



Politecnico di Bari

Repository Istituzionale dei Prodotti della Ricerca del Politecnico di Bari

Accurate blood pressure measurement from photoplethysmography signals using machine learning and deep learning techniques for innovative telemedicine

This is a PhD Thesis

Original Citation:

Accurate blood pressure measurement from photoplethysmography signals using machine learning and deep learning techniques for innovative telemedicine / De Palma, Luisa. - ELETTRONICO. - (2024). [10.60576/poliba/iris/de-palma-luisa_phd2024]

Availability:

This version is available at <http://hdl.handle.net/11589/280620> since: 2024-12-16

Published version

DOI:10.60576/poliba/iris/de-palma-luisa_phd2024

Publisher: Politecnico di Bari

Terms of use:

(Article begins on next page)

LIBERATORIA PER L'ARCHIVIAZIONE DELLA TESI DI DOTTORATO

Al Magnifico Rettore
del Politecnico di Bari

La sottoscritta Luisa De Palma nata a Corato il 26/05/1997

residente a Corato in via Nomentana 11/A e-mail luisa.depalma@poliba.it

iscritta al 3° anno di Corso di Dottorato di Ricerca in Ingegneria Elettrica e dell'Informazione ciclo XXXVII

ed essendo stata ammessa a sostenere l'esame finale con la prevista discussione della tesi dal titolo:

Accurate Blood Pressure Measurement from Photoplethysmography Signals Using Machine Learning and Deep Learning
Techniques for Innovative Telemedicine

DICHIARA

- 1) di essere consapevole che, ai sensi del D.P.R. n. 445 del 28.12.2000, le dichiarazioni mendaci, la falsità negli atti e l'uso di atti falsi sono puniti ai sensi del codice penale e delle Leggi speciali in materia, e che nel caso ricorressero dette ipotesi, decade fin dall'inizio e senza necessità di nessuna formalità dai benefici conseguenti al provvedimento emanato sulla base di tali dichiarazioni;
- 2) di essere iscritta al Corso di Dottorato di ricerca in Ingegneria Elettrica e dell'Informazione ciclo XXXVII, corso attivato ai sensi del "Regolamento dei Corsi di Dottorato di ricerca del Politecnico di Bari", emanato con D.R. n.286 del 01.07.2013;
- 3) di essere pienamente a conoscenza delle disposizioni contenute nel predetto Regolamento in merito alla procedura di deposito, pubblicazione e autoarchiviazione della tesi di dottorato nell'Archivio Istituzionale ad accesso aperto alla letteratura scientifica;
- 4) di essere consapevole che attraverso l'autoarchiviazione delle tesi nell'Archivio Istituzionale ad accesso aperto alla letteratura scientifica del Politecnico di Bari (IRIS-POLIBA), l'Ateneo archiverà e renderà consultabile in rete (nel rispetto della Policy di Ateneo di cui al D.R. 642 del 13.11.2015) il testo completo della tesi di dottorato, fatta salva la possibilità di sottoscrizione di apposite licenze per le relative condizioni di utilizzo (di cui al sito <http://www.creativecommons.it/Licenze>), e fatte salve, altresì, le eventuali esigenze di "embargo", legate a strette considerazioni sulla tutelabilità e sfruttamento industriale/commerciale dei contenuti della tesi, da rappresentarsi mediante compilazione e sottoscrizione del modulo in calce (Richiesta di embargo);
- 5) che la tesi da depositare in IRIS-POLIBA, in formato digitale (PDF/A) sarà del tutto identica a quelle **consegnate**/inviata/da inviarsi ai componenti della commissione per l'esame finale e a qualsiasi altra copia depositata presso gli Uffici del Politecnico di Bari in forma cartacea o digitale, ovvero a quella da discutere in sede di esame finale, a quella da depositare, a cura dell'Ateneo, presso le Biblioteche Nazionali Centrali di Roma e Firenze e presso tutti gli Uffici competenti per legge al momento del deposito stesso, e che di conseguenza va esclusa qualsiasi responsabilità del Politecnico di Bari per quanto riguarda eventuali errori, imprecisioni o omissioni nei contenuti della tesi;
- 6) che il contenuto e l'organizzazione della tesi è opera originale realizzata dalla sottoscritta e non compromette in alcun modo i diritti di terzi, ivi compresi quelli relativi alla sicurezza dei dati personali; che pertanto il Politecnico di Bari ed i suoi funzionari sono in ogni caso esenti da responsabilità di qualsivoglia natura: civile, amministrativa e penale e saranno dal sottoscritto tenuti indenni da qualsiasi richiesta o rivendicazione da parte di terzi;
- 7) che il contenuto della tesi non infrange in alcun modo il diritto d'Autore né gli obblighi connessi alla salvaguardia di diritti morali od economici di altri autori o di altri aventi diritto, sia per testi, immagini, foto, tabelle, o altre parti di cui la tesi è composta.

Bari 11/12/2024

Firma Luisa De Palma

La sottoscritta, con l'autoarchiviazione della propria tesi di dottorato nell'Archivio Istituzionale ad accesso aperto del Politecnico di Bari (POLIBA-IRIS), pur mantenendo su di essa tutti i diritti d'autore, morali ed economici, ai sensi della normativa vigente (Legge 633/1941 e ss.mm.ii.),

CONCEDE

- al Politecnico di Bari il permesso di trasferire l'opera su qualsiasi supporto e di convertirla in qualsiasi formato al fine di una corretta conservazione nel tempo. Il Politecnico di Bari garantisce che non verrà effettuata alcuna modifica al contenuto e alla struttura dell'opera.
- al Politecnico di Bari la possibilità di riprodurre l'opera in più di una copia per fini di sicurezza, back-up e conservazione.

Bari 11/12/2024

Firma Luisa De Palma



POLITECNICO DI BARI

DEPARTMENT OF ELECTRICAL AND INFORMATION ENGINEERING

ELECTRICAL AND INFORMATION PH.D. PROGRAM

SSD: ING-INF/07–ELECTRICAL AND ELECTRONIC MEASUREMENTS

FINAL DISSERTATION

Accurate Blood Pressure Measurement from
Photoplethysmography Signals Using Machine
Learning and Deep Learning Techniques for
Innovative Telemedicine

by

LUISA DE PALMA

Supervisors:

PROF. FILIPPO ATTIVISSIMO

PROF. ATTILIO DI NISIO

Coordinator of Ph.D. Program:

Prof. Mario Carpentieri

Course n°37, 01/11/2021-31/10/2024



POLITECNICO DI BARI

DEPARTMENT OF ELECTRICAL AND INFORMATION ENGINEERING

ELECTRICAL AND INFORMATION PH.D. PROGRAM

SSD: ING-INF/07–ELECTRICAL AND ELECTRONIC MEASUREMENTS

FINAL DISSERTATION

Accurate Blood Pressure Measurement from
Photoplethysmography Signals Using Machine
Learning and Deep Learning Techniques for
Innovative Telemedicine

by

LUISA DE PALMA

Referees:

PROF. EGIDIO DE BENEDETTO

PROF. ALBERTO VALLAN

Supervisors:

PROF. FILIPPO ATTIVISSIMO

PROF. ATTILIO DI NISIO

Coordinator of Ph.D. Program:

Prof. Mario Carpentieri

Course n°37, 01/11/2021-31/10/2024

CONTENTS

ABSTRACT	VII
LIST OF PUBLICATIONS	VIII
LIST OF FIGURES	XIV
LIST OF ABBREVIATIONS	XX
INTRODUCTION	24
<i>OVERVIEW AND THESIS OBJECTIVE</i>	24
<i>THESIS STRUCTURE</i>	27
CHAPTER 1	29
<i>PPG SIGNAL PROCESSING AND ENHANCEMENT</i>	29
<i>INTRODUCTION</i>	29
<i>OVERVIEW OF PPG SIGNAL</i>	31
1.1 DATASET PRE-PROCESSING AND LABELLING	33
1.1.1 DATASET	34
1.1.2 ALIGNMENT	35
1.1.3 CHUNKING	36
1.1.4 PRE-PROCESSING	36
1.1.5 PULSE SEGMENTATION AND LABELING	38
1.2 FEATURES EXTRACTION	39
1.3 ERROR ANALYSIS OF SP, DP AND DN CHARACTERISTIC POINTS ESTIMATION	46
1.4 FEATURES SELECTION	49
1.5 DISCUSSION	53
1.6 CONCLUSION	55
CHAPTER 2	57

CONTENTS

ML MODELS FOR SBP AND DBP ESTIMATION	57
<i>INTRODUCTION</i>	57
2.1 MACHINE LEARNING MODELS	59
2.1.1 XGBOOST MODELS	61
2.1.2 NN MODELS	63
2.2 RESULTS AND DISCUSSION	65
2.2.1 TRAINING AND TEST OF XGBOOST AND NN MODELS	65
2.2.2 COMPARISON WITH OTHER METHODS	69
2.2.3 COMPLIANCE TO STANDARDS AND CLASSIFICATION GUIDELINES	72
2.2.4 BLAND–ALTMAN ANALYSIS	76
2.3 CONCLUSION	78
CHAPTER 3	80
PERFORMANCE COMPARISON OF ML MODELS FOR SBP AND DBP ESTIMATION	80
<i>INTRODUCTION</i>	80
3.1 MACHINE LEARNING MODELS AND DATASET	82
3.2 COMPARISON OF RESULTS USING ML AND FEATURES SELECTED BY THREE SELECTION ALGORITHMS	84
3.3 EFFECTS OF ML ALGORITHMS AND DATASET SIZES ON RMSE AND TRAINING TIME	91
3.4 DISCUSSION	101
3.5 CONCLUSION	108
CHAPTER 4	110
ABP ESTIMATION THROUGH PPG SIGNAL ANALYSIS AND ADVANCED LOSS FUNCTION OPTIMIZATION	110
<i>INTRODUCTION</i>	110
4.1 DATASETS	113
4.1.1 MIMIC-III DATASET	114
4.1.2 MIMIC-II DATASET	115
4.2 METHODS AND MODELS	116
4.2.1 MODELS	117
4.2.2 EXPERIMENTAL CONFIGURATION	119
4.2.3 LOSS FUNCTION IMPLEMENTATION	119

CONTENTS

4.3	RESULTS	121
4.3.1	PPG AND ITS DERIVATIVES	122
4.3.2	PPG SIGNALS AS ONLY INPUT	125
4.3.3	SIGNALS FROM DATASET B	127
4.4	DISCUSSION	129
4.5	CONCLUSION	130
CHAPTER 5		132
HARDWARE IMPLEMENTATION FOR AN EMBEDDED SOLUTION		132
INTRODUCTION		132
5.1	HARDWARE DESIGN	134
5.1.1	DESIGN SPECIFICATIONS	136
5.1.2	MICROCONTROLLER	137
5.1.3	POWER MANAGEMENT	138
5.1.4	SAFETY	142
5.2	SENSORS	143
5.2.1	MAX30102	144
5.2.2	BMI270	145
5.2.3	QMC5883L	146
5.3	PCB DESIGN	146
5.4	SYSTEM FUNCTIONALITIES	148
CHAPTER 6		152
OTHER BIOMEDICAL APPLICATION FOR A TELEMEDICINE SOLUTION		152
INTRODUCTION		152
6.1	ARCHITECTURE OVERVIEW	154
6.2	SOLUTION'S IMPLEMENTATION	155
6.2.1	COMMUNICATION PROTOCOL OF THE CHECKME PRO	155
6.2.2	ANDROID APP	156
6.2.3	DATABASE STORAGE	159
6.2.4	WEB DASHBOARD	161
6.3	VALIDATION	163
6.4	CONCLUSION	166
CHAPTER 7		168

CONTENTS

<i>ECG WAVE SEGMENTATION FOR AN AUTOMATIC ANALYSIS</i>	168
<i>INTRODUCTION</i>	168
<i>7.1 ACQUISITION SYSTEM</i>	171
<i>7.2 ECG SEGMENTATION</i>	173
<i>7.2.1 RAW SIGNAL ACQUISITION</i>	174
<i>7.2.2 R-PEAK DETECTION</i>	175
<i>7.2.3 QRS ONSET AND OFFSET DETECTION</i>	177
<i>7.2.4 P WAVE SEGMENTATION</i>	179
<i>7.2.5 T WAVE SEGMENTATION</i>	180
<i>7.3 RESULTS</i>	181
<i>7.4 CONCLUSION</i>	183
CONCLUSION	184
APPENDIX A	186
REFERENCES	192

ABSTRACT

The aim of this thesis was to study, develop and validate systems for telemedicine applications to monitor vital parameters. The focus has been on photoplethysmography (PPG) devices to obtain non-invasive, cuff-less, wireless, and repeated measurements of blood pressure (BP), in addition to heart rate (HR), oxygen saturation of blood (SpO₂) and respiration rate (RR). It includes software design and implementation to estimate BP from the PPG signal, with the development of the processing algorithm, including filtering and noise elimination, and evaluating the critical issues on which it is necessary to intervene. The characteristic points of PPG signal have been identified and features have been extracted, including novel features extracted from the Maximal Overlap Discrete Wavelet Transform (MODWT) enhanced PPG signal. Then the most significant features have been identified by several selection algorithms. This has permitted to implement, train and compare the performance of several machine learning (ML) models with the aim of estimating systolic and diastolic BP using the processed PPG signal.

Afterwards, several deep learning (DL) algorithms have been implemented using the whole PPG signal instead of the features extracted from it, and the impact of the loss function, model's input and duration of the input has been investigated. Then a first prototype of a wearable embedded solution has been developed for a telemedicine application.

LIST OF PUBLICATIONS

A total of **four** papers have been published on international journals during the Ph.D. program and **one** has been accepted and is being published. Papers **[P6]** and **[P18]** have been authored before the beginning of the Ph.D. program. Paper **[P9]** has been awarded with the **IEEE MeMeA 2022 Student Travel Grant**; both papers **[P11]** and **[P12]** have received the **IEEE MeMeA 2023 Certificates of Appreciation**.

International Journal Papers Indexed by Scopus:

- [P1] F. Attivissimo, L. De Palma, A. Di Nisio, M. Scarpetta, A.M.L. Lanzolla, "Photoplethysmography Signal Wavelet Enhancement and Novel Features Selection for Non-Invasive Cuff-Less Blood Pressure Monitoring," *Sensors* 2023, 23, 2321, doi: **10.3390/s23042321**.
- [P2] F. Attivissimo, F. Adamo, L. De Palma, D. Lotano, A. Di Nisio, "First experimental tests on the prototype of a capacitive oil level sensor for aeronautical applications", *Acta IMEKO*, vol.12 (2023) no. 1, pp. 1-6, doi: **10.21014/actaimeko.v12i1.1474**.
- [P3] F. Attivissimo, V. I. D'Alessandro, L. De Palma, A. M. L. Lanzolla, and A. Di Nisio, "Non-Invasive Blood Pressure Sensing via Machine Learning," *Sensors*, vol. 23, no. 19, p. 8342, Oct. 2023, doi: **10.3390/s23198342**.

LIST OF PUBLICATIONS

- [P4] A. Di Nisio, **L. De Palma**, M. A. Ragolia, A. M. L. Lanzolla, F. Attivissimo, "Performance comparison of machine learning algorithms for the estimation of blood pressure using photoplethysmography", *Biomedical Signal Processing and Control*, Volume 99, 2024, 106838, ISSN 1746-8094, doi: [10.1016/j.bspc.2024.106838](https://doi.org/10.1016/j.bspc.2024.106838).
- [P5] F. Attivissimo, F. Adamo, **L. De Palma**, A. Di Nisio, M. A. Ragolia, A. M. L. Lanzolla, "Analysis of Model Parameters and Experimental Setup for Accurate Characterization of Ultrasound Phased Arrays Using a Low-Cost Sensor", in *IEEE Transactions on Instrumentation and Measurement*, (Accepted, To be published).

International Conference Proceedings Indexed by Scopus:

- [P6] **L. De Palma**, M. Scarpetta and M. Spadavecchia, "Characterization of Heart Rate Estimation Using Piezoelectric Plethysmography in Time- and Frequency-domain," 2020 IEEE International Symposium on Medical Measurements and Applications (MeMeA), Bari, Italy, 2020, pp. 1-6, doi: [10.1109/MeMeA49120.2020.9137226](https://doi.org/10.1109/MeMeA49120.2020.9137226).
- [P7] **L. De Palma**, F. Adamo, F. Attivissimo, S. De Gioia, A. Di Nisio, A.M.L. Lanzolla, M. Scarpetta, "Low-cost capacitive sensor for oil-level monitoring in aircraft," 2022 IEEE International Instrumentation and Measurement Technology Conference (I2MTC), 2022, pp. 1-4, doi: [10.1109/I2MTC48687.2022.9806667](https://doi.org/10.1109/I2MTC48687.2022.9806667).
- [P8] V. I. D'Alessandro, F. Paciolla, **L. De Palma**, F. Adamo, A. Di Nisio and N. Giaquinto, "Robotized sorter for blood classification using RFID tags," 2022 IEEE International Symposium on Medical Measurements and Applications (MeMeA), 2022, pp. 1-6, doi: [10.1109/MeMeA54994.2022.9856477](https://doi.org/10.1109/MeMeA54994.2022.9856477).

LIST OF PUBLICATIONS

- [P9] **L. De Palma**, F. Attivissimo, A. Di Nisio, A. M. L. Lanzolla, M. A. Ragolia and M. Spadavecchia, "Development of a web-based system for interfacing a portable Bluetooth vital sign monitor," 2022 IEEE International Symposium on Medical Measurements and Applications (MeMeA), 2022, pp. 1-6, doi: [10.1109/MeMeA54994.2022.9856526](https://doi.org/10.1109/MeMeA54994.2022.9856526).
- [P10] M. Scarpetta, M. Spadavecchia, V. I. D'Alessandro, **L. De Palma** and N. Giaquinto, "A new dataset of satellite images for deep learning-based coastline measurement," 2022 IEEE International Conference on Metrology for Extended Reality, Artificial Intelligence and Neural Engineering (MetroXRINE), 2022, pp. 635-640, doi: [10.1109/MetroXRINE54828.2022.9967574](https://doi.org/10.1109/MetroXRINE54828.2022.9967574).
- [P11] **L. De Palma**, V. I. D'Alessandro, F. Attivissimo, A. Di Nisio and A. M. L. Lanzolla, "ECG wave segmentation algorithm for complete P-QRS-T detection," 2023 IEEE International Symposium on Medical Measurements and Applications (MeMeA), Jeju, Republic of Korea, 2023, pp. 1-6, doi: [10.1109/MeMeA57477.2023.10171894](https://doi.org/10.1109/MeMeA57477.2023.10171894).
- [P12] V. I. D'Alessandro, **L. De Palma**, F. Attivissimo, A. Di Nisio and A. M. L. Lanzolla, "U-Net convolutional neural network for multisource heterogeneous iris segmentation," 2023 IEEE International Symposium on Medical Measurements and Applications (MeMeA), Jeju, Republic of Korea, 2023, pp. 1-5, doi: [10.1109/MeMeA57477.2023.10171896](https://doi.org/10.1109/MeMeA57477.2023.10171896).
- [P13] F. Adamo, G. Andria, F. Attivissimo, A. Di Nisio, **L. De Palma** and D. Lotano, "Characterization of Innovative Oil Level Sensors for Aerospace Applications," 2023 IEEE 10th International Workshop on Metrology for AeroSpace (MetroAeroSpace), Milan, Italy, 2023, pp. 374-379, doi: [10.1109/MetroAeroSpace57412.2023.10190007](https://doi.org/10.1109/MetroAeroSpace57412.2023.10190007).
- [P14] V. I. D'Alessandro, F. Adamo, **L. De Palma**, D. Lotano and M. Scarpetta, "U-Net Convolutional Neural Network for Optic Disc

LIST OF PUBLICATIONS

- Segmentation,” 2023 IEEE International Conference on Metrology for eXtended Reality, Artificial Intelligence and Neural Engineering (MetroXRINE), Milano, Italy, 2023, pp. 1087-1091, doi: [10.1109/MetroXRINE58569.2023.10405762](https://doi.org/10.1109/MetroXRINE58569.2023.10405762).
- [P15] **L. De Palma**, A. D. Nisio, A. Lanzolla, D. Lotano, A. Pignatelli and M. A. Ragolia, “Development of a System for Monitoring Driver Comfort via Smartphones,” 2024 IEEE International Symposium on Medical Measurements and Applications (MeMeA), Eindhoven, Netherlands, 2024, pp. 1-6, doi: [10.1109/MeMeA60663.2024.10596743](https://doi.org/10.1109/MeMeA60663.2024.10596743).
- [P16] R. Germinario, A. la Grasta, M. De Carlo, **L. De Palma**, F. Dell’Olio, V. M. N. Passaro, “Simulation and design of an ISFET-based biosensor for estimating Ca²⁺ concentration in sweat,” 2024 IEEE Sensors Applications Symposium (SAS), Naples, Italy, 2024, pp. 1-6, doi: [10.1109/SAS60918.2024.10636565](https://doi.org/10.1109/SAS60918.2024.10636565).
- [P17] M. A. Ragolia, **L. De Palma**, N. Giaquinto, A. Pignatelli, M. Scarpetta, “Ultrasound Haptics for XR and Rehabilitation: Influence of Arm and Hand Muscle Stiffness on User Perception,” 2024 IEEE International Conference on Metrology for eXtended Reality, Artificial Intelligence and Neural Engineering (MetroXRINE), St Albans-London, UK, 2024, (To be published).

National Conference Proceedings:

- [P18] A. Di Nisio, A.M.L. Lanzolla, M. Spadavecchia, E. Allegretti, **L. De Palma**, E. Sibilano, “Characterization and calibration of heart rate measuring devices and algorithms”, Atti del IV Forum Nazionale delle Misure, Messina, pp. 169-170, ISBN: 978-88-9456-130-2, 10-12 settembre 2020.

LIST OF PUBLICATIONS

- [P19] F. Attivissimo, **L. De Palma**, A. Di Nisio, A. M. L. Lanzolla, M. A. Ragolia, “Piattaforma virtuale per la verifica real-time di sistemi di localizzazione elettromagnetici per la navigazione chirurgica”, Atti del VI Forum Nazionale delle Misure, Brescia, pp. 35-42, ISBN: 9788894561357, 15-17 settembre 2022.
- [P20] F. Adamo, G. Andria, **L. De Palma**, N. Giaquinto, M. Scarpetta, “Didattica delle Misure: un software per la correzione automatica di domande a risposta aperta”, Atti del VI Forum Nazionale delle Misure, Brescia, pp. 165-166, ISBN: 9788894561357, 15-17 settembre 2022.
- [P21] F. Attivissimo, **L. De Palma**, A. Di Nisio, A. M. L. Lanzolla, M. A. Ragolia, M. Spadavecchia, “Implementazione di una soluzione di telemedicina per un monitor di parametri vitali indossabile”, Atti del VI Forum Nazionale delle Misure, Brescia, pp. 299-300, ISBN: 9788894561357, 15-17 settembre 2022.
- [P22] V. I. D’Alessandro, **L. De Palma**, A. Di Nisio, A.M.L. Lanzolla, M.A. Ragolia, M. Scarpetta, “Enfatizzazione del segnale fotopletismografico e selezione di nuove feature per il monitoraggio non invasivo della pressione sanguigna”, Atti del VII Forum Nazionale delle Misure, Bologna, pp. 197-198, ISBN: 978-88-942753-2-2, 13-15 settembre 2023.
- [P23] F. Adamo, F. Attivissimo, **L. De Palma**, A. Di Nisio, A.M.L. Lanzolla, M.A. Ragolia, “Caratterizzazione termica a lungo termine di sensori di livello capacitivi flessibili realizzati mediante stampa 3D”, Atti del VII Forum Nazionale delle Misure, Bologna, pp. 377-378, ISBN: 978-88-942753-2-2, 13-15 settembre 2023.
- [P24] **L. De Palma**, F. Attivissimo, A. Di Nisio, V.I. D’Alessandro, “Stima non invasiva della pressione sanguigna dal segnale fotopletismografico utilizzando modelli di machine learning”, Atti del VIII Forum Nazionale

LIST OF PUBLICATIONS

delle Misure, S. Vincenzo (LI), pp. 225-226, ISBN: 978-88-942753-3-9, 12-14
settembre 2024.

LIST OF FIGURES

Fig. 1. Types of PPG measurements.	32
Fig. 2. PPG signal and its pulsatile and steady parts.	32
Fig. 3. PPG signal and the two phases of the cardiac cycle.	33
Fig. 4. Workflow of data analysis.	33
Fig. 5. Raw PPG signal and ABP signal before alignment.	35
Fig. 6. Alignment of the normalized PPG and ABP signals.	36
Fig. 7. Example of segmentation of the raw PPG signal.	38
Fig. 8. Workflow of the processing steps.	39
Fig. 9. Different morphologies of PPG pulses of $xNORM$ with characteristic points for two different patients: (blue pulse) adult patient; (red pulse) neonate patient. Sampling frequency is 125 Hz.	41
Fig. 10. (a) Scaling function; (b) wavelet function.	43
Fig. 11. Pulse PPG before (blue) and after (red) the use of MODWT.	44
Fig. 12. ABP pulse corresponding to the PPG pulse with SBP and DBP values.	45
Fig. 13. (a) Histogram of errors for systolic locations; (b) boxplot of errors with mean, mean + standard deviation (STD) and mean-STD.	47
Fig. 14. (a) Histogram of errors for diastolic locations; (b) boxplot of errors with mean, mean + STD and mean-STD.	47
Fig. 15. (a) Histogram of errors for dicrotic notch locations; (b) boxplot of errors with mean, mean + STD and mean-STD.	48
Fig. 16. (a) Feature importance scores sorted using RRelief algorithm for SBP measurement; (b) feature importance scores sorted using CFS algorithm for SBP measurement; (c) feature importance scores sorted using MRMR algorithm for SBP measurement. Feature labels are noted as follows: (*) calculated on $xFILT$ (i.e. before MODWT enhancement), (°) calculated on $xMODWT$ (i.e. after MODWT enhancement), (-) calculated on the normalized signal $xNORM$, (+) new feature and (#) already known feature.	51
Fig. 17. (a) Feature importance scores sorted using RRelief algorithm for DBP	

LIST OF FIGURES

measurement; (b) feature importance scores sorted using CFS algorithm for DBP measurement; (c) feature importance scores sorted using MRMR algorithm for DBP measurement. Feature labels are noted similarly to the previous figure. _____	53
Fig. 18. (a) Systolic and (b) diastolic blood pressure occurrences in 2 mmHg bins. Only the observations with $80 \text{ mmHg} \leq \text{SBP} \leq 180 \text{ mmHg}$ and $60 \text{ mmHg} \leq \text{DBP} \leq 110 \text{ mmHg}$ were considered since outside these ranges there were few observations and, also, DBP less than 60 mmHg corresponds to severe hypertension condition. _____	59
Fig. 19. NN with nine hidden layers with 1024, 1024, 1024, 512, 512, 512, 128, 64, and 64 neurons. _____	64
Fig. 20. Error probability density of SBP, DBP, and MAP estimations. Errors were defined as the difference between the predicted pressures (using XGBoost model or NN model) and measured ones; then, their histograms were normalized to obtain the probability densities shown in the plot. _____	67
Fig. 21. (a, c, e) Regression of the predicted output and true response for SBP, DBP, and MAP estimations using the XGBoost model; (b, d, f) Regression of the predicted output and true response for SBP, DBP, and MAP estimations using the NN model. _____	69
Fig. 22. Confusion matrix for BP level classification according to ESH/ESC guidelines. _____	75
Fig. 23. Bland–Altman plots for (a) SBP, (b) DBP, and (c) MAP. _____	78
Fig. 24. Overview of data flow. _____	84
Fig. 25. Significant features for SBP using three selection algorithms: RReliefF (a), MRMR (b), CFS (c). _____	87
Fig. 26. Significant features for DBP using three selection algorithms: RReliefF (a), MRMR (b), CFS (c). _____	88
Fig. 27. RMSE results for systolic pressure (a) and for diastolic pressure (b) using the reduced dataset and two different selection methods namely MRMR and RReliefF. The training time is reported in the logarithmic scale. _____	97
Fig. 28. Training time and RMSE for SBP measurement, with indication of the Pareto front. _____	98
Fig. 29. RMSE of SBP measurement, varying the dimension of the training dataset. _____	99
Fig. 30. Fitting of RMSE for SBP measurement varying the number of observations using XGBoost models. _____	104
Fig. 31. Workflow of the processing for Dataset A. _____	115
Fig. 32. Loss weight compared with the ABP signal to weight the systolic and diastolic peaks. _____	120
Fig. 33. Developed system architecture. _____	134

LIST OF FIGURES

Fig. 34. Master BOARD. _____	135
Fig. 35. Slave BOARD. The PPG sensor, not shown here, is soldered into the opening on the right side of the board. _____	136
Fig. 36. The schematic of power management circuit based on MCP73832T. _____	139
Fig. 37. Schematic of DW01A and of FS8205. _____	140
Fig. 38. Schematic of TLV757P. _____	141
Fig. 39. Protection circuit. _____	142
Fig. 40. Functional diagram of the MAX30102 [137]. _____	144
Fig. 41. Components of the MAXREFDES117 [138]. _____	145
Fig. 42. Parameters for the acquisition. _____	149
Fig. 43. MATLAB interface for PPG signal acquisition and vital parameters. _____	150
Fig. 44. Block diagram of architecture developed. _____	155
Fig. 45. Daily check measurements, after calibration of BP by means of a sphygmomanometer. The second measurement (top) is repeated about 1 minute after the first one (bottom). _____	157
Fig. 46. Daily check measurements, before (bottom) and after (top) calibration of BP by means of a sphygmomanometer. _____	158
Fig. 47. Data sending screen. _____	159
Fig. 48. Sections of the web app menu. _____	162
Fig. 49. Personal data of user section. _____	162
Fig. 50. Plot of HR with timestamp of acquisitions. View of web app screen. _____	163
Fig. 51. Experimental setup used for validation with Fluke ProSim 8 (red box) and Checkme Pro medical device (blue box). _____	165
Fig. 52. ECG signal morphology of a cardiac cycle. _____	169
Fig. 53. AD8232 single lead heart rate monitor in a break-out board developed by Sparkfun. _____	172
Fig. 54. Positioning of electrodes based on Einthoven triangle (black pad corresponds to the right arm, blue pad corresponds to the left arm and the red one to the right leg). _____	172
Fig. 55. Experimental setup for ECG acquisition. _____	173
Fig. 56. Raw ECG signal. _____	174
Fig. 57. Filtered ECG signal. _____	175
Fig. 58. R-peak detection algorithm. _____	175
Fig. 59. ECG signal after WT. _____	176
Fig. 60. ECG signal after WT transform (blue) and square signal (red). _____	176
Fig. 61. R-peak detection on Raw ECG signal. _____	177
Fig. 62. Standard deviation of sliding window (blue) and zeros detected from zero-	

LIST OF FIGURES

<i>crossing algorithm.</i>	178
Fig. 63. <i>QRS complex segmentation.</i>	179
Fig. 64. <i>P wave and T wave detection algorithms.</i>	179
Fig. 65. <i>P wave segmentation.</i>	180
Fig. 66. <i>T wave segmentation.</i>	181
Fig. 67. <i>Percentage of detection.</i>	182
Fig. 68. <i>IOU for all the ECG waves.</i>	183

LIST OF TABLES

<i>Table 1. Mean and STD of errors for characteristic points.</i>	48
<i>Table 2. Search spaces and best values of hyper-parameters for SBP.</i>	62
<i>Table 3. Search spaces and the best values of hyper-parameters for DBP.</i>	62
<i>Table 4. Validation results for SBP and DBP estimations.</i>	66
<i>Table 5. Test results using XGBoost and NN models.</i>	66
<i>Table 6. Comparison with other works.</i>	70
<i>Table 7. Comparison of results for the validation set with AAMI standard.</i>	73
<i>Table 8. Comparison of results for the test set with AAMI standard.</i>	73
<i>Table 9. Comparison of results for the validation set with BHS standard.</i>	73
<i>Table 10. Comparison of results for the test set with BHS standard.</i>	73
<i>Table 11. Results of BP level classification according to ESH/ESC guidelines.</i>	76
<i>Table 12. Systolic pressure measurement performance using XGBoost model.</i>	90
<i>Table 13. Diastolic pressure measurement performance using XGBoost model.</i>	90
<i>Table 14. Systolic pressure measurement performance using NN model.</i>	91
<i>Table 15. Diastolic pressure measurement performance using NN model.</i>	91
<i>Table 16. Performance comparison of ML models and features sets for systolic (a) and diastolic (b) pressure measurement.</i>	92
<i>Table 17. Statistical analysis of the best models for systolic pressure (a) and for diastolic pressure (b).</i>	101
<i>Table 18. Comparison of several ML models and features selection methods.</i>	106
<i>Table 19. Comparison of the results with Costa et al for Dataset A4.</i>	122
<i>Table 20. Comparison of results varying the duration.</i>	123
<i>Table 21. Comparison of results between the use of MSE and the implemented loss functions using Residual U-Net and 30 s PPG and its derivatives (Dataset A3) and 8.192 s PPG and its derivatives (Dataset A4) on test set.</i>	124
<i>Table 22. Comparison of results between the use of MSE and the implemented loss functions using an 8.192 s PPG signal and Residual U-Net (Dataset A1) on test set.</i>	

LIST OF TABLES

.....	125
Table 23. Comparison of results by using the implemented loss function and MSE and two different lengths of the signal and Residual U-Net on the test set.	126
Table 24. Comparison of results by using the two different loss functions and different models on test set.	127
Table 25. Comparison of results by using Dataset B and the approximation-refinement models with different loss functions.	128
Table 26. Data used to validate the measurements acquired by the medical device. Reference values are provided by Fluke ProSim 8.	166
Table 27. Mean time error and standard deviation for each ECG wave, onsets, and offsets.	182
Table A1. Features.	186

LIST OF ABBREVIATIONS

1D	One-Dimensional
AAMI	Association for the Advancement of Medical Instrumentation
ABP	Arterial Blood Pressure
ADC	Analog to Digital Converter
AMR	Anisotropic Magnetoresistance
APIs	Application Programming Interfaces
ARMA	Autoregressive Moving Average
BHS	British Hypertension Society
BIAS	Mean of Differences
BLE	Bluetooth Low Energy
BMS	Battery Management System
BP	Blood Pressure
CFS	Correlation-based Feature Selection
CI	Confidence Interval
CNNs	Convolutional Neural Networks
CRC	Cyclic Redundancy Check
CVD	Cardiovascular Disease
DAQ	Data Acquisition
DBP	Diastolic Blood Pressure
DL	Deep Learning
DMS	Driver Monitoring System
DN	Dicrotic Notch
DP	Diastolic Peak
DRC	Design Rule Check
DWT	Discrete Wavelet Transform
ECG	Electrocardiogram
EEG	Electroencephalogram

LIST OF ABBREVIATIONS

EMD	Empirical Mode Decomposition
ESC	European Society of Cardiology
ESH	European Society of Hypertension
ET	Ensemble of Tree
FFT	Fast Fourier Transform
FPC	Flexible Printed Circuit
GBR	Gradient Boosting Regressor
GP	Gaussian Process
GPR	Gaussian process regression
HR	Heart Rate
HTML	Hypertext Markup Language
HTTP	Hypertext Transfer Protocol
I2C	Inter Integrated Circuit
ICU	Intensive Care Unit
IMODWT	Inverse Maximal Overlap Discrete Wavelet Transform
IMU	Inertial Measurement Unit
IOU	Intersection Over Union
IP	Inflection Point
ISM band	Industrial Scientific and Medical band
JSON	JavaScript Object Notation
KAR	Kernel Approximation Regression
LA	Left Arm
LDO	Low Dropout Regulator
LED	Light Emitting Diode
LOA	Limits Of Agreement
LR	Linear Regression
LSTM	Long Short-Term Memory
MAE	Mean Absolute Error
MAP	Mean Arterial BP
ME	Mean Error
MEG	Magnetoencephalography
MEMS	Micro Electro-Mechanical Systems
MIC	Maximum Information Coefficient
ML	Machine Learning
MODWT	Maximal Overlap Discrete Wavelet Transform
MRMR	Minimum Redundancy Maximum Relevance

LIST OF ABBREVIATIONS

MSE	Mean Squared Error
MSP	Max Slope Point
NADAM	Nesterov-accelerated Adaptive Moment Estimation
NN	Neural Network
NTP	Network Time Protocol
PCA	Principal Component Analysis
PCB	Printed Circuit Board
PCC	Pearson's correlation coefficients
PG	Plethysmography
PHP	Hypertext Preprocessor
PI	Pulse Index
PPG	Photoplethysmography
PTT	Pulse Transit Time
PWV	Pulse Wave Velocity
R	Correlation Coefficient
RA	Right Arm
ReLU	Rectified Linear Unit
REST	Representational State Transfer
RL	Right Leg
RMSE	Root Mean Squared Error
RNNs	Recurrent Neural Networks
RR	Respiration Rate
RT	Regression Tree
SBP	Systolic Blood Pressure
SDK	Software Development Kit
SI	Arterial Stiffness
SOA	Service Oriented Architecture
SP	Systolic Peak
SpO₂	Oxygen Saturation of Blood
STD	Standard Deviation
STFT	Short Time Fourier Transform
SVM	Support Vector Machine
TDP	Diastolic Peak Time
TL	Transfer Learning
TSP	Systolic Peak Time
UART	Universal Asynchronous Receiver-Transmitter

LIST OF ABBREVIATIONS

URLs Uniform Resource Locators

USB Universal Serial Bus

UUID Universally Unique Identifier

WT Wavelet Transform

XGBoost eXtreme Gradient Boost

INTRODUCTION¹

OVERVIEW AND THESIS OBJECTIVE

Photoplethysmography (PPG) is an optical measurement technique that can be exploited to measure the oxygen saturation of blood (SpO_2), to estimate heart rate (HR), respiration rate (RR), and to evaluate atherosclerosis and arterial stiffness. Recently, the use of PPG to also estimate Blood Pressure (BP) values with appropriate calibration has become an active area of research. Indeed, the ability to use, for these purposes, a signal acquired at a single site by a wearable, non-invasive, wireless, miniaturized, inexpensive, and easy-to-use sensor certainly has great potential to control the health of an individual and detect states of hypertension; in fact, nowadays, the interest in the use of the PPG signal is becoming more and more important for the estimation of BP.

Among vital signs, the monitoring of BP is a very important aspect in the treatment of many clinical conditions; it is relevant for the assessment of the state of hypertension, which is associated with chronic diseases and an increase in mortality and morbidity. Currently, measurements are made using cuff-based devices that are complicated, not always accurate, and are prone to errors if the cuff is not of the correct size or if the appropriate calibrations are not made; hence, a fundamental prerequisite is that both the caregiver and the patient need to be trained in their use. Moreover, the gold standard is the invasive BP monitoring

¹ This Introduction is based on the papers [1], [2].

INTRODUCTION

of arterial blood pressure (ABP), which is carried out through the cannulation of a peripheral artery and is utilized in the management of critically ill and perioperative patients. For this reason, there is the spread of the development of practical and reliable telemedicine solutions [3],[4],[5],[6] to guarantee monitoring at home and at hospitals with the aim of ensuring early identification and prevention of cardiovascular diseases (CVDs), hypertension, and other related diseases by using non-invasive, low-cost, and portable solutions.

In this thesis, new features relevant to BP estimation using PPG are presented. A total of 195 features, including the proposed ones and those already known in the literature, have been calculated on a set composed of 50,000 pulses from 1,080 different patients. Three feature selection methods, namely Correlation-based Feature Selection (CFS), RReliefF, and Minimum Redundancy Maximum Relevance (MRMR), have then been applied to identify the most significant features for BP estimation. Some of these features have been extracted through a novel PPG signal enhancement method based on the use of the Maximal Overlap Discrete Wavelet Transform (MODWT). As a matter of fact, the enhanced signal leads to a reliable identification of the characteristic points of the PPG signal (e.g., systolic, diastolic, and dicrotic notch points) by simple means, obtaining results comparable with those from purposefully defined algorithms. Hence, this study leads to the selection of several new features from the MODWT enhanced signal on every single pulse extracted from PPG signals, in addition to features already known in the literature. These features can be employed to train machine learning (ML) models useful for estimating systolic blood pressure (*SBP*) and diastolic blood pressure (*DBP*) in a non-invasive way, which is suitable for telemedicine healthcare monitoring. In fact, a ML approach to estimating BP using PPG is then presented. The final aim of this work was to develop ML methods for estimating BP in a non-invasive way that is suitable in a telemedicine healthcare monitoring context. The training of regression models useful for

INTRODUCTION

estimating *SBP* and *DBP* was conducted using new extracted features from PPG signals processed using MODWT. Subsequently, an in-depth performance analysis has been done on the estimation of *SBP* and *DBP* by using features from the PPG signal enhanced using the MODWT to train many ML regression models, including eXtreme Gradient Boost (XGBoost). The impact on accuracy of different features selection methods, ML methods, training set sizes, and the use of signal enhancement have been analyzed. One result is the achievable improvements using, for ML, features extracted from MODWT enhanced PPG signals. Then, a comparison of the results obtained using different sets of the most significant features is reported. One set of features also includes the new ones extracted from the MODWT enhanced signal, and the other set includes only the features already known in the literature. Moreover, several ML algorithms have been trained to provide a comparison of their accuracy and training time, showing the Pareto front. RReliefF and MRMR selection algorithms, and several ML algorithms such as XGBoost, Gaussian process regression (GPR) models, and Ensemble models stood out for their performance, with a different compromise between prediction error and training time. In addition, a further result has been obtained by varying the dimension of the dataset to understand the impact on root mean squared error (RMSE) for models that have shown better performance, giving an empirical relationship on achievable RMSE as a function of training set size. From that relationship, an upper boundary of the set size has been extrapolated, over which no further RMSE improvements are expected.

After this analysis, the focus was on applying the trained models to a different dataset than the one used, obtained using a different PPG sensor. This aspect is aligned with the final objective of this thesis. However, it was immediately evident that there was a problem, already known from the literature, that occurs when the dataset or sensor changes. With this aim, ML models were re-analyzed

INTRODUCTION

in a transfer learning (TL) context, and calibration attempts on the PPG signal were attempted. Analyses were also carried out on the features extracted from the different datasets to understand their ranges. At the end of this study, deep learning (DL) approaches were experimented since DL models are more prone to exploit the potential of TF. The first analysis involved a comparison of different DL models and the study of the TL to solve the problem defined previously, using the PPG signal to obtain the estimated pressure values *SBP* and *DBP*; subsequently, further analysis involved the use of the PPG signal to obtain the *ABP* signal, and another aspect of inter-subjectivity and intra-subjectivity was addressed. Taking into account the works in the literature, it was decided to study the impact that the loss function has in the training phase as the models and the dataset vary. Finally, an embedded solution was implemented to create a telemedicine system that can also estimate BP from the PPG signal in addition to HR, SpO₂, and RR.

THESIS STRUCTURE

The thesis is structured as follows: in **Chapter 1** the MODWT enhancement of PPG signal and the novel features selection for non-invasive cuff-less BP monitoring are dealt with, in particular the source database and the signal pre-processing are described; then features extraction and selection is presented, including new proposed features obtained by using MODWT. In **Chapter 2** the ML approach for XGBoost models is presented and a comparison of the obtained results with the literature has been done, focusing on standard medical protocols for performance assessment. In **Chapter 3** a more detailed focus on several ML algorithms and a study on different feature sets obtained using three different selection algorithms is presented.

In **Chapter 4** DL models have been developed to obtain the *ABP* signal from the

INTRODUCTION

PPG signal without relying on purposely extracted signal features. Finally, a more in-depth analysis was carried out considering the impact of the loss function on training. In **Chapter 5** the hardware implementation of a portable solution for the acquisition of PPG signal, accelerometer, gyroscope and magnetometer data using an ESP32 and a web server is illustrated with the ultimate goal of implementing a complete telemedicine solution that includes, among others parameters, BP estimation. It was essential to develop a prototype to acquire the PPG signal and fully leverage the implementation discussed in the previous chapters. Furthermore, by using TL, it will be possible to apply the implemented models to signals obtained from different sensors such as the sensor under consideration which operates in reflective mode and differs from the PPG sensor utilized in the public dataset, which employs a sensor in transmissive mode. Additionally, this approach will enable the creation of a dataset, which will be crucial for validating the processing implementation. In **Chapter 6** and **Chapter 7** other telemedicine solutions for biomedical applications are presented, focusing on several vital signs. The final two chapters emphasize the importance of monitoring vital signs by expanding the focus beyond the PPG signal. The goal is to incorporate additional types of physiological signals and different hardware, for example a multi-parametric device and a single lead heart rate monitor, aiming to offer a comprehensive overview of potential telemedicine applications that could be integrated. This approach will aim to provide a thorough assessment of a patient's overall health status.

PPG SIGNAL PROCESSING AND ENHANCEMENT²

INTRODUCTION

In recent years, telemedicine has become increasingly prevalent, due to the utilization of innovative wearable sensors, miniaturized devices and even smartphones that permit the monitoring of vital signs. These devices are characterized by their simplicity of use, non-invasiveness and wireless connectivity [6], [7], [8], [9], [10], [11]. Among the vital signs BP requires adequate monitoring. Consequently, researchers are exploring methods for performing cuff-less and non-invasive BP measurements. A significant number of studies are currently focused on the use of PPG for BP estimation.

Several studies have been conducted over the years and continue to be conducted today on the use of electrocardiogram (ECG) and PPG signals acquired simultaneously for the estimation of BP [12], additionally, studies have been conducted on the use of only the PPG signal. There is a relationship between the PPG signal and BP that is related to a measure of the speed of the blood flow, known as pulse wave velocity (PWV) [13], this allows for the measurement of the time for a blood pulse to reach a peripheral point from the heart, which is known as the pulse transit time (PTT) [14]. A shorter PTT is associated with a higher BP,

² This Chapter is based on [1].

CHAPTER 1

while a longer PTT is associated with a lower BP. However, this approach necessitates the acquisition of data from multiple sites and the synchronization of the two signals. Consequently, the use of the PPG signal alone represents a promising path for further investigation and improvement. Indeed, it has the potential to make the acquisition process more efficient although it necessitates more complex processing to derive BP estimates from the PPG signal. Moreover, the use of PPG for the estimation of BP is not without its own set of criticalities and limitations. These include the need to eliminate noise, develop multi-photodetectors, identify events, carry out individual calibration based on skin color and clinical factors, and address calibration drift over short time intervals [15].

Consequently, there is a necessity to enhance BP measurement through PPG, for this reason the focus of the research is on the investigation of PPG signal characteristics that are correlated with BP and can be exploited for ML [16], [17], [18], [19], [20], [21], [22], [23]. Features can be employed for the non-invasive measurement of both *SBP* and *DBP*. They can be defined in time domain (including the calculation of derivatives), frequency domain, or statistically. Moreover, various ML methodologies have been explored by researchers, including support vector machines (SVM), regression trees (RT), neural networks (NN), linear regression (LR), and others. This Chapter presents a study and research focused on the extraction of new and more significant features from PPG signals with the potential to improve BP estimation. In particular, it has been demonstrated that the use of the MODWT enables the enhancement of the PPG signal and the extraction of features that are crucial for this objective. As a matter of fact, it has been demonstrated that MODWT enhances the identification of characteristic points in the PPG signal, thereby rendering it more similar to the ABP signal. Consequently, this study introduces several novel features that are useful for BP estimation, which can be extracted from both the enhanced and the

CHAPTER 1

base PPG signal. These features have not been previously utilized in literature. Another significant contribution of this study is the meticulous examination of both novel and known features with the objective of identifying those most pertinent to BP estimation. To this end, three distinct feature selection algorithms have been employed to analyze features extracted from a substantial number of PPG signals contained in the MIMIC-III Waveform Database. The analysis has led to the identification of the most informative features for BP estimation. This is a fundamental and general result that can be applied to any other work involving the use of ML techniques for BP measurement from PPG signals.

OVERVIEW OF PPG SIGNAL

PPG is spreading for real-time monitoring of vital signs because it is a simple, low-cost, and non-invasive optical measurement method that can provide important health information. It is a type of plethysmography (PG) that exploits optical properties unlike other types of PG, such as those based on capacitive, inductive, and piezoelectric properties [24], [25]. PPG measures light transmitted or reflected between a source (LED) and a photodetector placed on the surface of the skin, which is affected by volumetric changes in blood circulation [26]. In transmission measurements, it is possible to use red light (680 nm) or near infrared light (810 nm), as they allow deeper penetration. In reflection measurements, the photodetector reveals backscattered or reflected light from tissues, bones, and blood vessels [27] as shown in **Fig. 1**.

CHAPTER 1

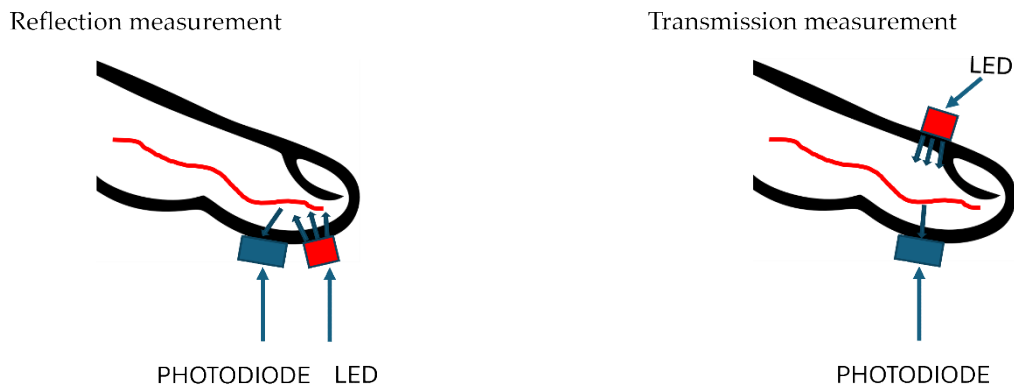


Fig. 1. Types of PPG measurements.

Since the maximum pulsatile component of reflected light occurs in the wavelength range between 510 nm and 590 nm, green light (565 nm) and yellow light (590 nm) can be used [15], [28]. The PPG signal is characterized by a pulsatile part and a steady part, as shown in **Fig. 2**; the pulsatile one is associated with the variation of BP with blood volume changes and is synchronous to the pulse, while the steady one is associated with some aspects such as respiration and the sympathetic nervous system.

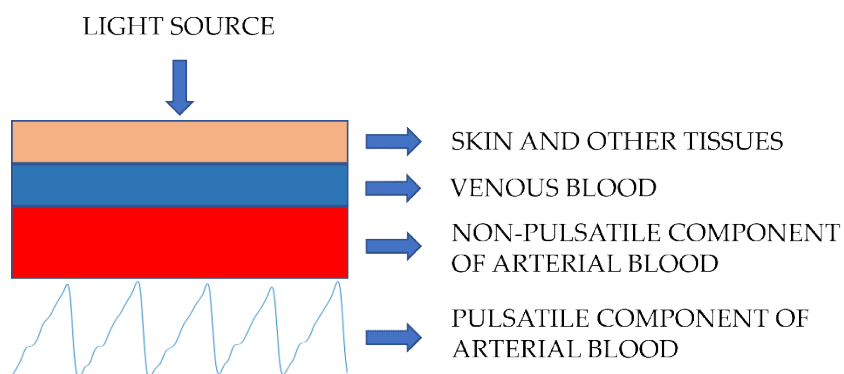


Fig. 2. PPG signal and its pulsatile and steady parts.

The two phases of the cardiac cycle characterized by systole and diastole can be identified in the PPG signal. The systole phase is characterized by an increase in blood perfusion, resulting in an increase in volume. The increase in arterial volume results in greater absorption of emitted light, and therefore the reflected

CHAPTER 1

or transmitted light that reaches the photodiode is less. The opposite situation occurs during diastole, as shown in **Fig. 3**.

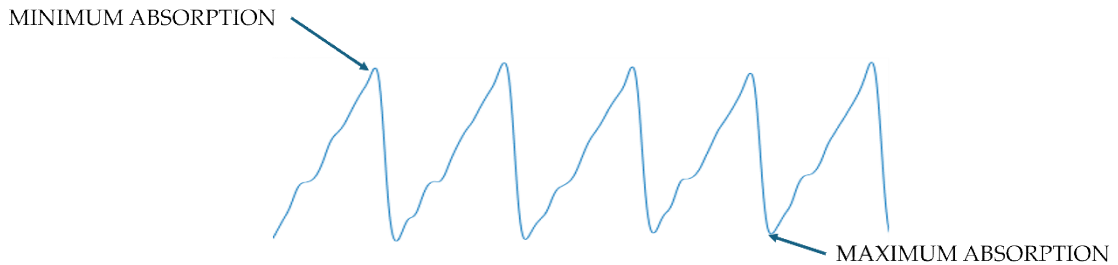


Fig. 3. PPG signal and the two phases of the cardiac cycle.

1.1 DATASET PRE-PROCESSING AND LABELLING

In this study, a clinical dataset of physiological signals acquired by the monitors of patients in an intensive care unit (ICU) is utilized. However, due to the frequent interruption or alteration of acquisitions (resulting from factors such as monitoring device failure, misconfiguration, or shifts in patient condition), these datasets often contain records of varying lengths, with missing or anomalous signals. Consequently, a multitude of automated checks have been employed to eliminate unreliable data in a systematic manner as the analysis progresses. The data processing has been conducted using MATLAB R2022a.

The workflow of the data analysis is illustrated in **Fig. 4** and described in detail in this and subsequent sections.

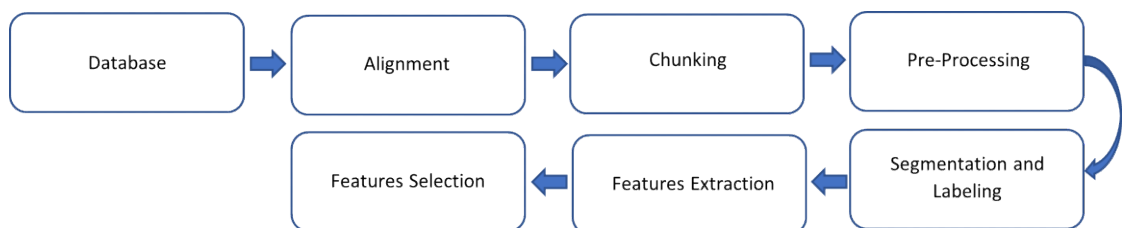


Fig. 4. Workflow of data analysis.

CHAPTER 1

1.1.1 DATASET

This study was conducted using PPG and ABP signals available in the open access MIMIC-III Waveform Database [29], [30], [31], which was selected for its size and accessibility. It is an extension of the MIMIC II Waveform Database, which has been utilized in numerous other works pertaining to the analysis of biomedical signals. The MIMIC-III Waveform Database contains physiologic signals acquired from bedside monitors in adults aged 16 years or above (representing 87% of admissions, with 56% of these individuals being male adults) and neonatal (13% of admissions) ICUs. These signals are almost always accompanied by one or more ECG signals as well as ABP, PPG, and respiration signals. The age quartiles for adults are as follows $Q_1 = 52.8$ years, $Q_2 = 65.8$ years and $Q_3 = 77.8$ years. The most prevalent patient conditions are coronary atherosclerosis of the native coronary artery (7.1%), unspecified septicemia (4.2%), and subendocardial infarction (initial episode of care) (3.6%). The data was collected using two critical care information systems, each comprising a different set of medical devices. The Philips CareVue Clinical Information System (with Intellivue MP-70 monitor) and the iMDsoft MetaVision ICU were utilized. All protected health information in the database is deidentified and no demographic information is provided. Furthermore, the PPG signals available in this database have been collected using a fingertip device (Multi-Measurement Module), and all signals have been acquired at a sampling rate of 125 Hz. Given the extensive size of the database, only a portion of folder #30 and the entirety folder #32 were initially downloaded from the database, corresponding to 6,740 patients. However, for the study presented in this Chapter, only patients where both PPG and ABP signals were available, corresponding to 1,080 patients, have been considered. The WFDB MATLAB Toolbox [31], [32] and purposely created functions have been utilized for data handling.

1.1.2 ALIGNMENT

When ABP and PPG are acquired by different devices, they are provided without time alignment as shown in **Fig. 5**.

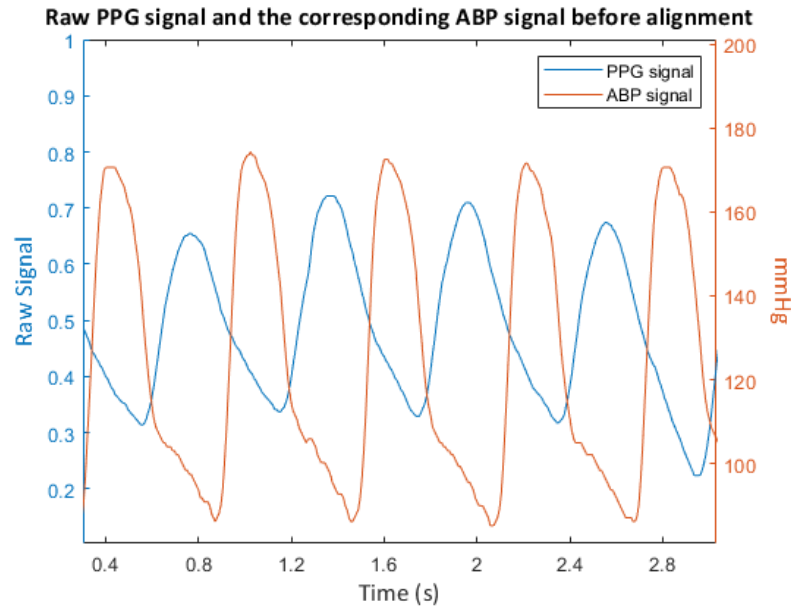


Fig. 5. Raw PPG signal and ABP signal before alignment.

It is essential to verify in advance that the signals are properly aligned; if any misalignment is detected, the alignment should be implemented.

Consequently, such alignment has been carried out for all records using cross-correlation as reported in [17], [33], [34]. The cross-correlation function

$$g(\Delta t) = \sum ABP(t) \times PPG(t + \Delta t) \quad (1)$$

was calculated between the two signals, and the location of the maximum value was identified as time lead or lag, different between pairs of signals. An example of the alignment is shown in **Fig. 6**.

CHAPTER 1

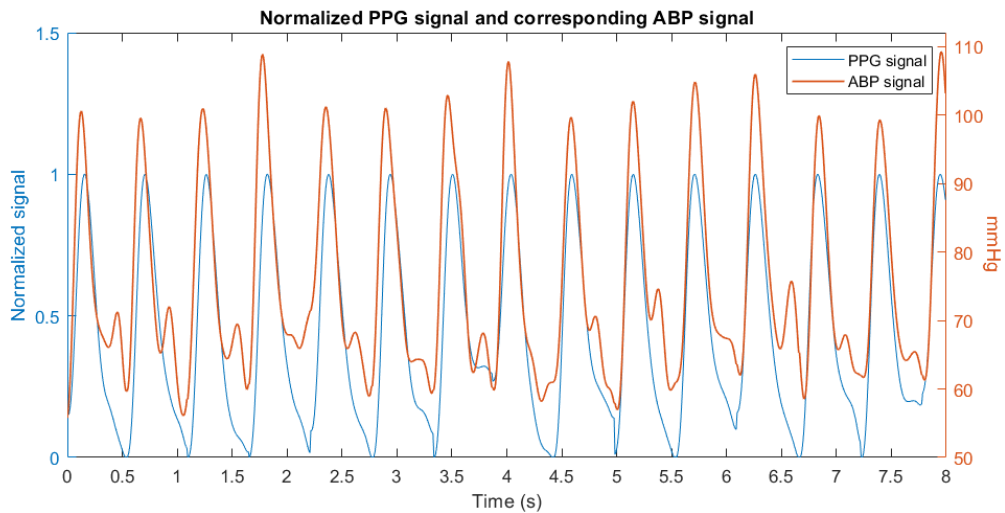


Fig. 6. Alignment of the normalized PPG and ABP signals.

1.1.3 CHUNKING

For each record, consecutive blocks of 30 s have been obtained by signal chunking. The duration of the signal chunks is arbitrary, but is considered adequate for the purpose of obtaining physiological information such as HR.

1.1.4 PRE-PROCESSING

Subsequently, the PPG signals were subjected to the following processing: (1) denoising, by following the technique reported in [34], [35], [36] and used in [17], which involved the application of a second-order Butterworth filter with pass-band 0.5 Hz to 8 Hz; (2) Z-score standardization was carried out in accordance with the methodology described in [17]; and (3) baseline correction was performed using the technique reported in [37], [38], [39] and used in [19], which consists of the removal of a fourth-order fitted polynomial. The resulting signal will subsequently be referenced later as x_{FILT} .

The ABP signal has also been processed to partition each chunk into pressure pulses, which will be used to measure *SBP* and *DBP* later. For that partitioning, a tenth-order lowpass Yule-Walker recursive filtering with an 8 Hz cut-off

CHAPTER 1

frequency has been applied to the ABP signal and the *slope sum function* has been calculated as reported in [40] to identify ABP pulses. The duration of the analyzing window length for the slope sum calculation is selected to be equal to the typical duration of the upslope of the pulse, and in this study it has been set to 0.128 s (similarly to [40]). This corresponds to 16 samples acquired at $f_s = 125$ Hz.

Afterwards, the ABP pulses were evaluated in accordance with the *complementary signal abnormality index* [40], [41] and, if they exceeded a threshold of 0.4, the entire ABP chunk and the corresponding PPG chunk were discarded from subsequent processing, as demonstrated in [33].

Additionally, PPG chunks were also discarded if they failed a similarity test. In the literature, several similarity tests have been proposed, including those presented in [17], [18]. In this Chapter, however, a different test based on the coefficient of determination of several linear regressions has been used. For the purpose of this study, PPG pulses were identified by using the corresponding bounds of ABP pulses, and then the following regressions have been calculated: of the PPG pulse on the corresponding ABP pulse; of a PPG pulse on the previous one; and of an ABP pulse on the previous one. In each one of the three cases, separately, the average of the coefficient of determination among the pulses within the chunk was calculated. Chunks were discarded if the average of the coefficient of determination was less than 0.8, as demonstrated in [33].

The coefficient of determination rsq has been computed as follows:

$$\begin{aligned} y_{resid} &= x - y_{fit} \\ SS_{resid} &= \sum_{i=1}^N y_{resid}^2 \\ SS_{total} &= (N - 1) var(x) \end{aligned} \quad (2)$$

CHAPTER 1

$$rsq = 1 - \frac{SS_{resid}}{SS_{total}}$$

where $\mathbf{x} = [x_1, \dots, x_i, \dots, x_N]$ is the sampled PPG pulse signal of length N , with $i = 1, \dots, N$, and $y_{fit} = [y_1, \dots, y_i, \dots, y_N]$ is the associated fitting.

1.1.5 PULSE SEGMENTATION AND LABELING

In order to facilitate the extraction of features, it is essential to segment PPG pulses independently of the ABP pulses that were previously identified. To this end, this study extends the *slope sum function* calculation to PPG in analogy to ABP, thereby obtaining a partitioning of the chunk. The accurate identification of the onset points of PPG pulses is of great significance for the subsequent extraction of time-related features. The results of the application of the *slope sum function* to identify the onsets of the pulses are presented in **Fig. 7** on the raw PPG signal.

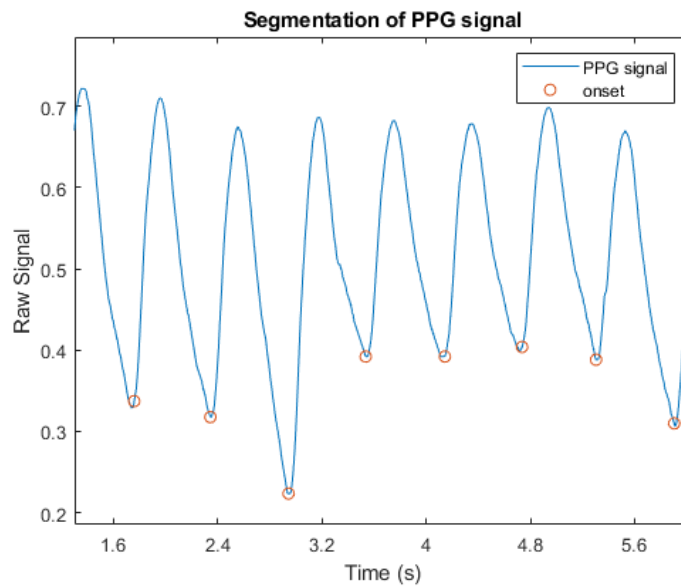


Fig. 7. Example of segmentation of the raw PPG signal.

The initial segment obtained was excluded from further analysis, as it may have contained a partial pulse. For each PPG pulse, an additional signal quality index

CHAPTER 1

based on skewness has been calculated as described in [20]. In this Chapter PPG pulse has been discarded when skewness value was less than zero. Subsequently, the PPG pulses were labelled with the corresponding *SBP* and *DBP* values, which were necessary for the phase of features selection. In order to achieve this, the ABP pulses were re-segmented in accordance with the boundaries of the PPG pulses. Then, for each processed ABP pulse, the *SBP* was calculated as the peak value and the *DBP* as the next minimum value. Finally, ABP pulses and the corresponding PPG pulses were discarded if they had non-physiological values, specifically when $SBP > 300$ mmHg or $DBP < 20$ mmHg or $HR < 20$ bpm or $HR > 200$ bpm.

All the processing steps are shown in **Fig. 8**.

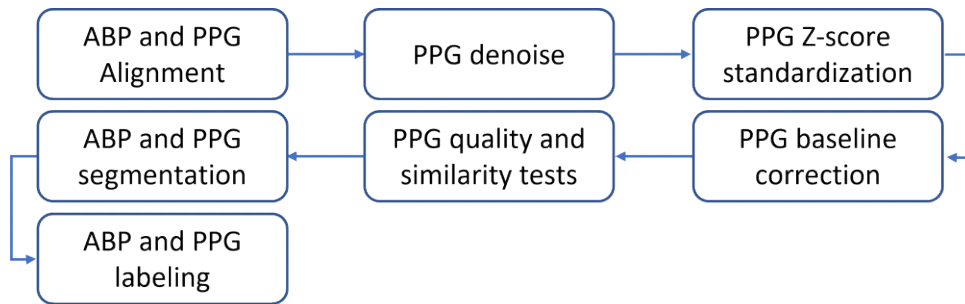


Fig. 8. Workflow of the processing steps.

1.2 FEATURES EXTRACTION

The extraction of the features was conducted on PPG pulses or PPG chunks, processing the following signals:

4. x_{FILT} , obtained after the baseline correction;
5. x_{NORM} , obtained after normalization of x_{FILT} in the range $[0, 1]$ for each pulse separately;
6. x_{MODWT} , obtained from x_{FILT} after the MODWT enhancement that will be discussed later in this section.

CHAPTER 1

A total of 195 extracted features were identified. The most relevant ones are listed and defined in **Appendix A**, wherein features already known in the literature [19], [21], [23] are distinguished from those proposed in this study for BP measurement on PPG signals.

Several proposed features have been extracted from individual pulses using the MATLAB built-in function *extract*, which gives features in the time domain and frequency domain on each pulse of x_{FILT} and x_{MODWT} and, in a few cases, also of x_{NORM} . Clearly, the definition of these features is well established; however, their application to x_{MODWT} PPG signals to evaluate their significance for BP is novel. Many features have been extracted from the PPG pulses on x_{FILT} following [19], [21], [22], [23], and are related to the amplitude of characteristic points, area, width, time, first and second derivatives, nonlinear functions of features, and statistics.

Moreover, the characteristic points have been identified on each PPG pulse of x_{FILT} , shown in **Fig. 9**, and they are *max slope point* (MSP), *systolic peak* (SP), *dicrotic notch* (DN), *inflection point* (IP), and *diastolic peak* (DP).

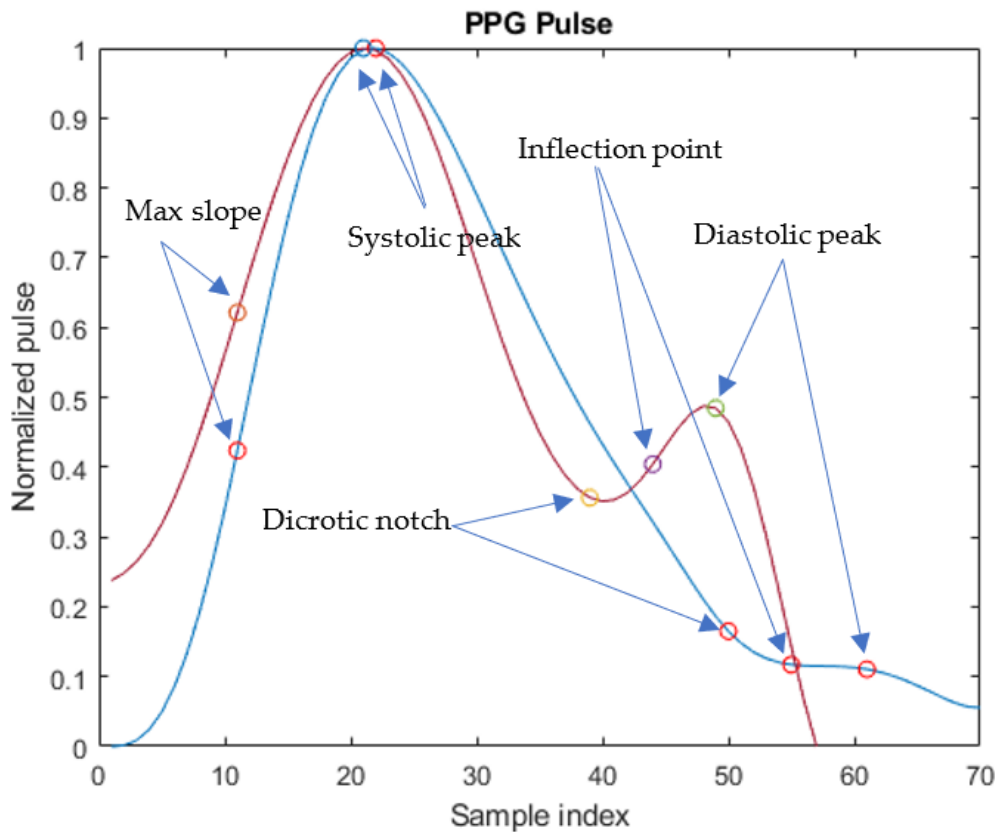


Fig. 9. Different morphologies of PPG pulses of x_{NORM} with characteristic points for two different patients: (blue pulse) adult patient; (red pulse) neonate patient. Sampling frequency is 125 Hz.

The identification of those characteristic points cannot be obtained reliably based only on PPG amplitude, as the signal morphology varies considerably between patients. This is particularly evident in relation to age and condition, as shown in **Fig. 9**. Indeed, the DP may not be evident in the signal. Hence, the detection of points has been conducted in accordance with the algorithms presented in [22], which also encompass the first and second derivatives of PPG pulses.

This Chapter proposes an alternative approach to determining characteristic points, alternative to [22], which is based on the application of proper wavelet filtering to obtain an enhanced PPG signal that better resembles the ABP signal. In order to achieve this, the MODWT has been applied to each pulse, with the

CHAPTER 1

computation being carried out down to level $\lfloor \log_2 N \rfloor$, where N is the number of samples of the pulse.

Wavelets have found application for the enhancement and denoising of medical images and bio signals as evidenced by [42], [43], [44]. In particular, MODWT has been used successfully for other physiological signals, including ECG, electroencephalogram (EEG), and magnetoencephalography (MEG) [45], [46], and has also proven suitable for the PPG signal in this study. This wavelet is an undecimated wavelet transform analogous to the discrete wavelet transform (DWT). Unlike the DWT, however, no down sampling of coefficients is conducted during its computation, resulting in a high degree of redundancy. Furthermore, MODWT is a linear filtering operation that can be utilized to assess the behaviors of a signal dependent on its scale. It is a time-shift-invariant method that facilitates the alignment of decomposed wavelet and scaling coefficients at each level with the initial signal. Additionally, it enables the examination of localized signal variations. Consequently, a linear combination of the scaling function and wavelet function is employed, taking into account the number of decomposition levels. The implementation of the MODWT, used in this study, performs the circular convolution in the Fourier domain.

The reconstruction of the pulse has been achieved through the application of the Inverse Maximal Overlap Discrete Wavelet Transform (IMODWT). Among the numerous variants of the MODWT, the sym4 synthesis wavelet was selected as it yielded superior outcomes in the highlighting of the characteristic points. This wavelet belongs to a family of wavelets that are near symmetric, orthogonal, and biorthogonal. The scaling function and the wavelet function are shown in **Fig. 10**.

CHAPTER 1

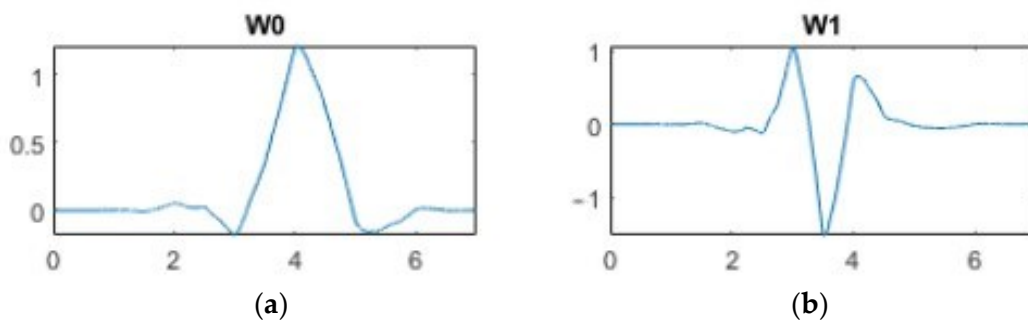


Fig. 10. (a) Scaling function; (b) wavelet function.

For the signal synthesis with IMODWT, only the fourth and fifth levels coefficients have been utilized. As reported in [47], these selected coefficients were found to maximize the energy of the QRS complex in ECG signals. In this study, the same approach has allowed the obtention of a frequency-localized version of the PPG pulse, which covers the bandwidth that maximizes its energy. In fact, the use of MODWT on the PPG pulse represents a key point in this study. This approach has allowed the emphasis of two of the most relevant points of a PPG pulse, namely the DP and the DN, as illustrated in Fig. 9. In the algorithm implemented in this research, SP is identified as the first peak of the enhanced PPG pulse, followed by a local minimum corresponding to DN, and then by a local maximum that is identified as DP.

As is evident in Fig. 11, the DP and the DN are more pronounced in the enhanced signal and there is a greater similarity with the morphology of the ABP pulse shown in Fig. 12. In contrast in the PPG pulse before the application of MODWT, these points are less pronounced and cannot be reliably identified unless information from the first and second derivatives is also utilized.

CHAPTER 1

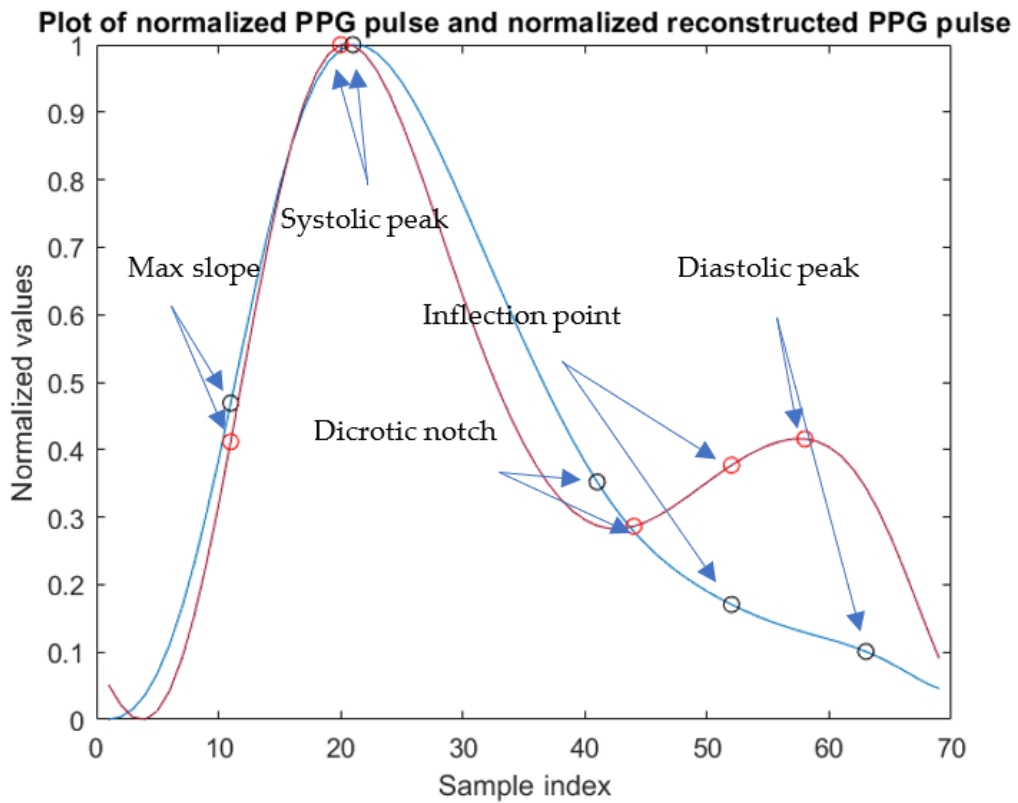


Fig. 11. Pulse PPG before (blue) and after (red) the use of MODWT.

From these new pulses, which exhibit an improved similarity with the ABP pulse, additional features have then been extracted. These include the characteristic points of the PPG pulse, time-related features, area-related features, energy-related features, amplitude-related features, and other features in the time and frequency domains. This has been achieved through the utilization of the built-in MATLAB function, *extract*. The **Appendix A** presents a list of features extracted from the enhanced pulses.

CHAPTER 1

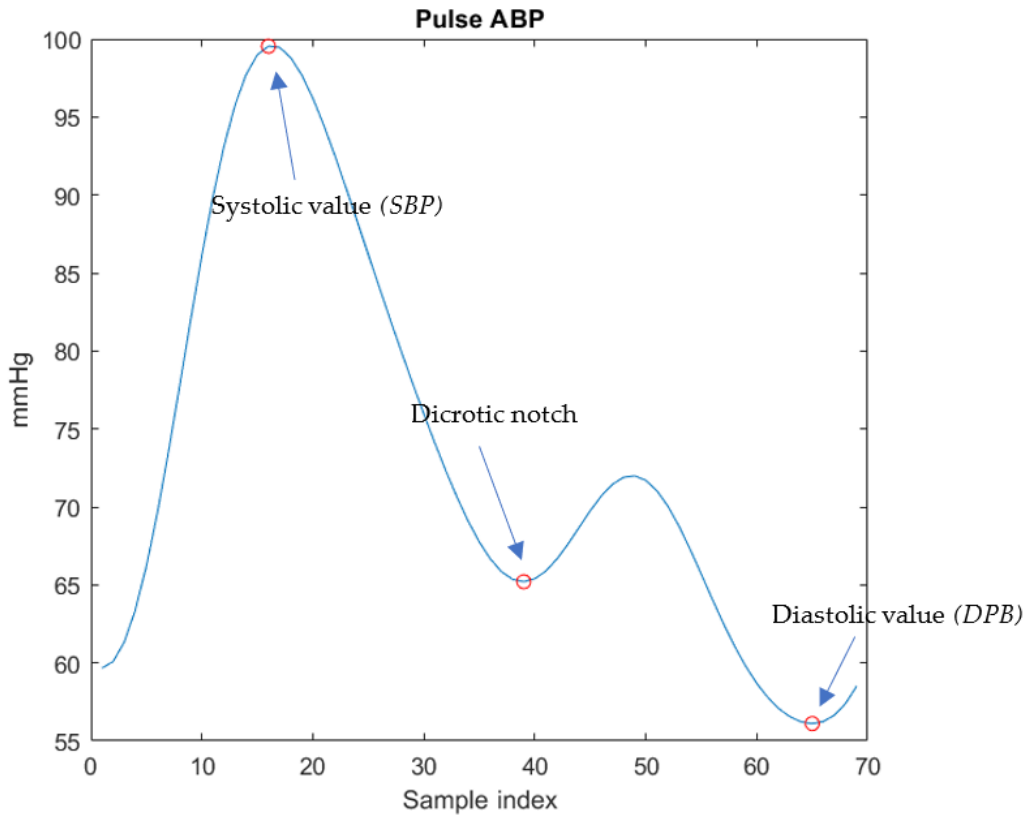


Fig. 12. ABP pulse corresponding to the PPG pulse with SBP and DBP values.

In addition, other features have been computed by considering the signal in time intervals that include couples constituted by a pulse and the next one, rather than a single pulse. In such case, the calculated value for each couple is averaged among all the couples within a given chunk. This resulting feature value is then assigned to each pulse within the chunk (e.g., Mean of $tb1$, Mean of $tb2$, Mean of $TP/p2\pi$, Mean of $TDN/p2\pi$, etc.).

Finally, there are features that have been calculated on the PPG chunk as a whole, rather than smaller intervals or single pulses. Once more, the value is assigned, again, to each pulse of the chunk (e.g., Area from 2 to 5, Peak1, Freq1, Freq2, etc.). Several frequency-related features have been obtained by means of the Fast Fourier Transform (FFT) applied to each PPG chunk of x_{FILT} in order to extract the sixteen FFT features described in [19]. Other statistics-related features, such

CHAPTER 1

as the mean and standard deviation, have been calculated on PPG chunks following denoising and prior to Z-scores standardization.

From the obtained set of 20×10^6 pulses, each one described by its features, random samples have been extracted for the analysis performed in the next sections.

1.3 ERROR ANALYSIS OF SP, DP AND DN CHARACTERISTIC POINTS ESTIMATION

The timing of the characteristic points of PPG pulses is of particular relevance, and features based on them are correlated with PTT, stiffness of the large arteries, BP, and age [48].

In fact, the SP time (TSP) is due to the arrival of a pressure wave from the left ventricle, while the DP time (TDP) is due to a pressure wave that reaches the lower limbs and is reflected back towards the fingers, hence the time interval between them is related to transit times and also to arterial stiffness SI

$$SI = \frac{h}{(TDP - TSP)} \quad (3)$$

where h is the patient's height.

It has therefore been deemed necessary to study the differences between the instants of SP (and also DP and DN) obtained by applying the algorithms in [22], based on derivatives, minus the ones obtained with the algorithm reported in this thesis that exploits the MODWT. For this purpose, timings have been calculated, in both cases, with resolution 8 ms, which is equal to the sampling step (given the 125 Hz sampling frequency of signals in the dataset).

CHAPTER 1

Therefore, a statistical analysis has been carried out on the aforementioned errors by randomly sampling 2×10^6 pulses.

The initial observation is that the DP is visible in less than 1% of x_{FILT} pulses, but in 95% of x_{MODWT} pulses. Hence, in the vast majority of x_{MODWT} pulses, the DP can be identified directly by searching for the second local peak (after the SP). Conversely, in the corresponding x_{FILT} , when the DP is not visible as a peak, the DP location commonly assumed in the literature is the one where the second derivative is zero, as also followed in this study.

The location differences for x_{FILT} minus x_{MODWT} are shown in **Fig. 13 - Fig. 15**.

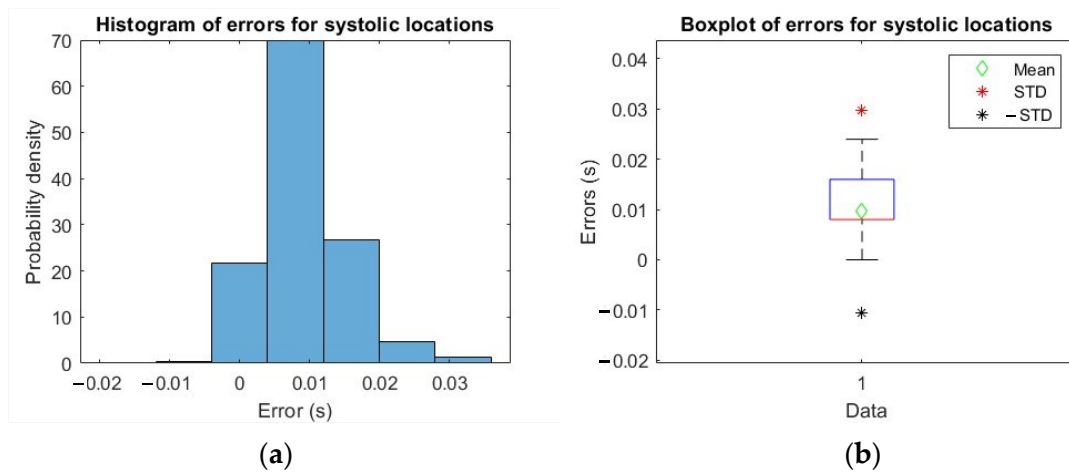


Fig. 13. (a) Histogram of errors for systolic locations; (b) boxplot of errors with mean, mean + standard deviation (STD) and mean-STD.

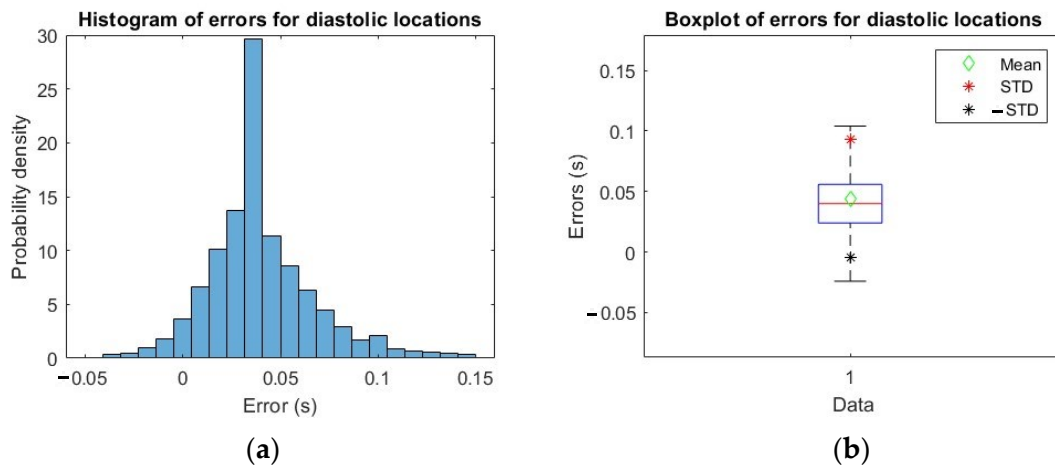


Fig. 14. (a) Histogram of errors for diastolic locations; (b) boxplot of errors with mean, mean + standard deviation (STD) and mean-STD.

CHAPTER 1

mean + STD and mean-STD.

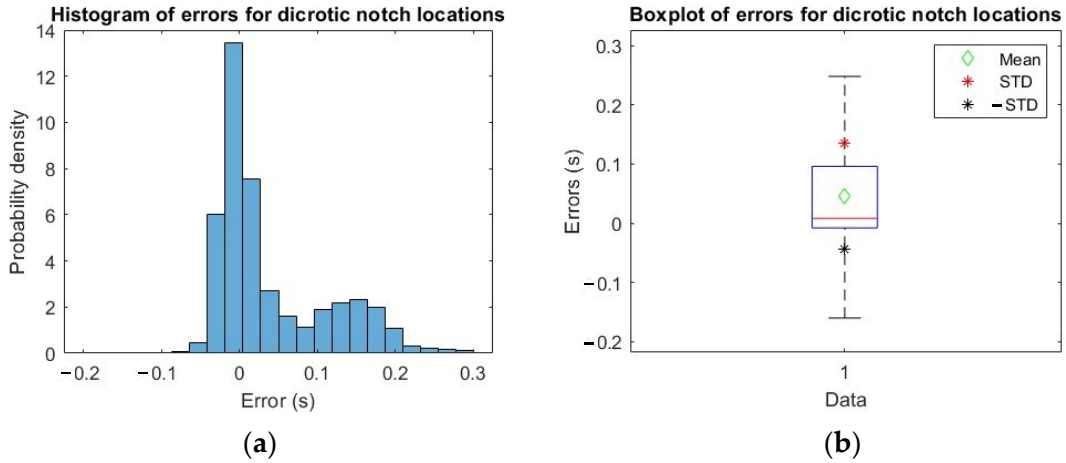


Fig. 15. (a) Histogram of errors for dicrotic notch locations; (b) boxplot of errors with mean, mean + STD and mean-STD.

In **Table 1**, the mean and STD of errors computed as described above are reported for the three characteristic points.

Table 1. Mean and STD of errors for characteristic points.

	Mean (s)	STD (s)
Systolic Points (SP)	0.0097	0.0202
Diastolic Points (DP)	0.0441	0.0486
Dicrotic Notch Points (DN)	0.0458	0.0896

It can be observed from the plots in **Fig. 13 - Fig. 15**, and the values in **Table 1** that the time error calculated in all three cases is very small. It is crucial that the error associated with identifying characteristic points is minimized to ensure the compatibility of the two point-identification methods. Therefore, it can be concluded that the implemented algorithm based on MODWT is a valid alternative that is compatible with the one in the literature for identifying the three characteristic SP, DP and DN points of the PPG pulse.

CHAPTER 1

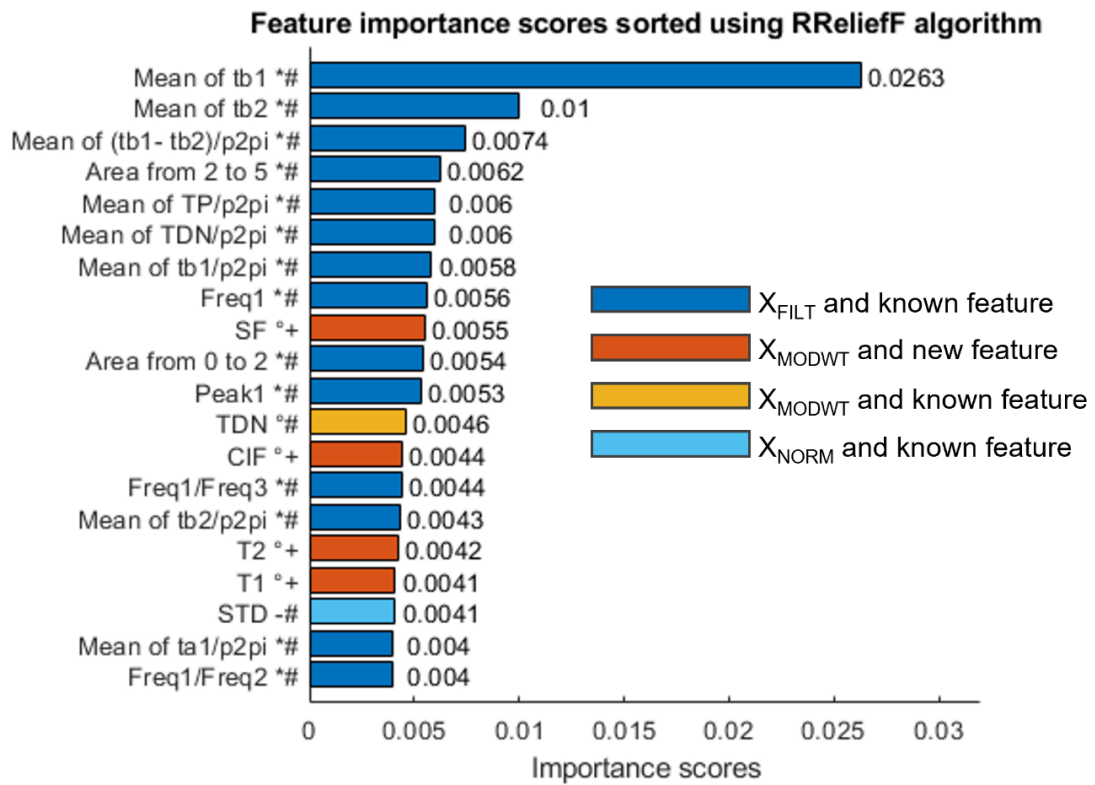
In the following section, the objective is to ascertain whether the features extracted using the three characteristic points obtained after MODWT improvement, in addition to the remaining newly obtained features, are significant for BP measurement.

1.4 FEATURES SELECTION

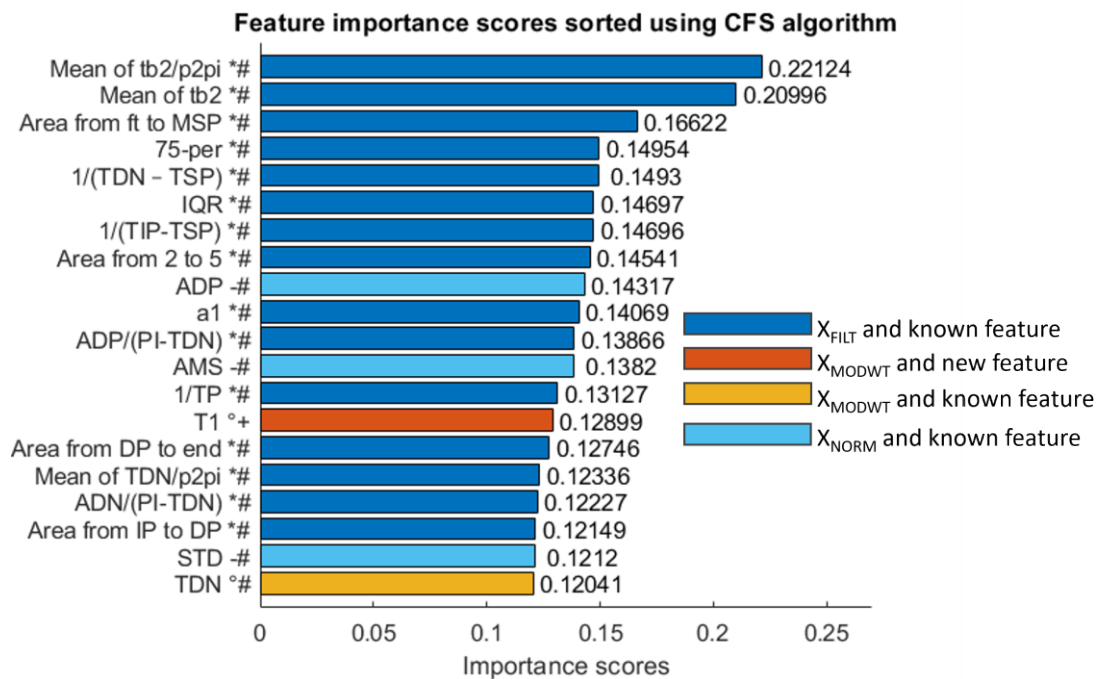
Subsequently, a selection of the most significant features related to *DBP* and *SBP* labels was made following the process of features extraction. A random subset of 50,000 pulses was selected for the subsequent analysis.

For these purposes, three different methods have been used following [19]. The algorithms used are: the CFS [49], which calculates the correlation and selects features that are at the same time highly correlated with the label and negligibly correlated with each of the other features; the RReliefF [50], [51], which penalizes the predictors that assign different values to neighbors with the same label and rewards predictors that assign different values to neighbors with different labels; and the MRMR [52], [53], which identifies an optimal set of features that are mutually as dissimilar as possible and can effectively represent the label. The last algorithm minimizes redundancy among a feature set while maximizing the relevance of a feature set to the label. The three methods were employed to identify the best feature sets for *SBP* measurement. The first 20 features (out of 195) are shown in **Fig. 16** and listed in **Table A1** of the **Appendix A**.

CHAPTER 1

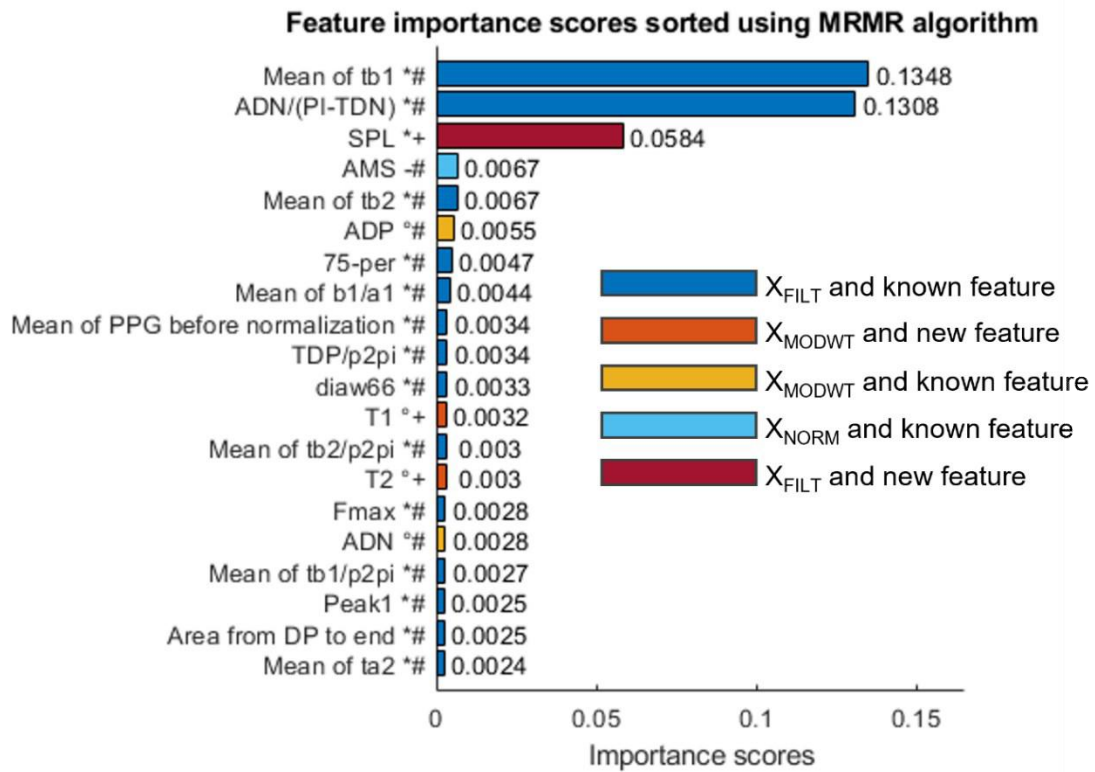


(a)



(b)

CHAPTER 1



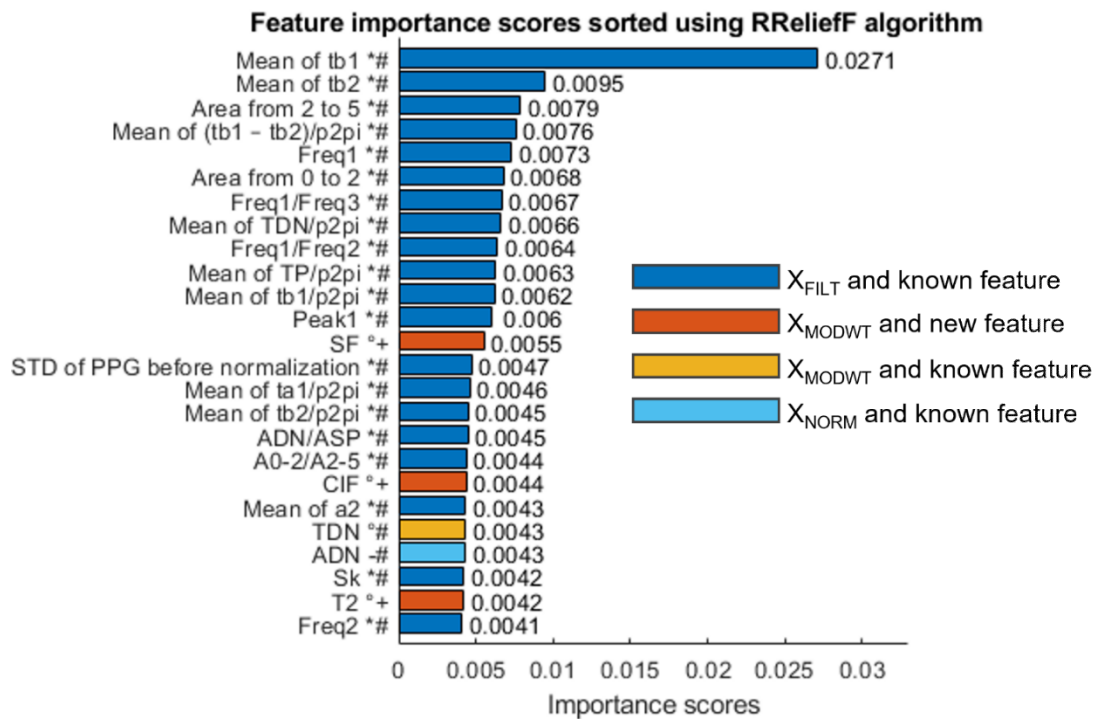
(c)

Fig. 16. (a) Feature importance scores sorted using RReliefF algorithm for *SBP* measurement; (b) feature importance scores sorted using CFS algorithm for *SBP* measurement; (c) feature importance scores sorted using MRMR algorithm for *SBP* measurement. Feature labels are noted as follows: (*) calculated on x_{FILT} (i.e. before MODWT enhancement), (°) calculated on x_{MODWT} (i.e. after MODWT enhancement), (-) calculated on the normalized signal x_{NORM} , (+) new feature and (#) already known feature.

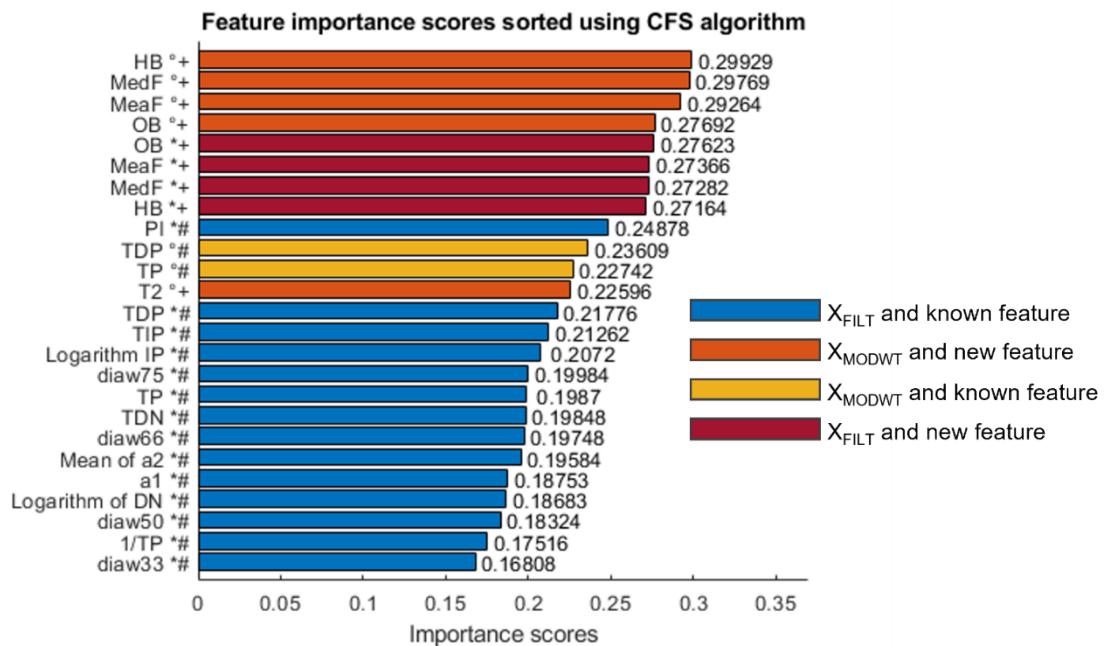
The results demonstrate that the three methods select, among the best features, some of the new features extracted from the MODWT enhanced signal, which confirms their significance, as will be discussed in the next section.

The same procedure has also been followed to identify the most significant features associated with *DBP* measurement, as shown in **Fig. 17**.

CHAPTER 1

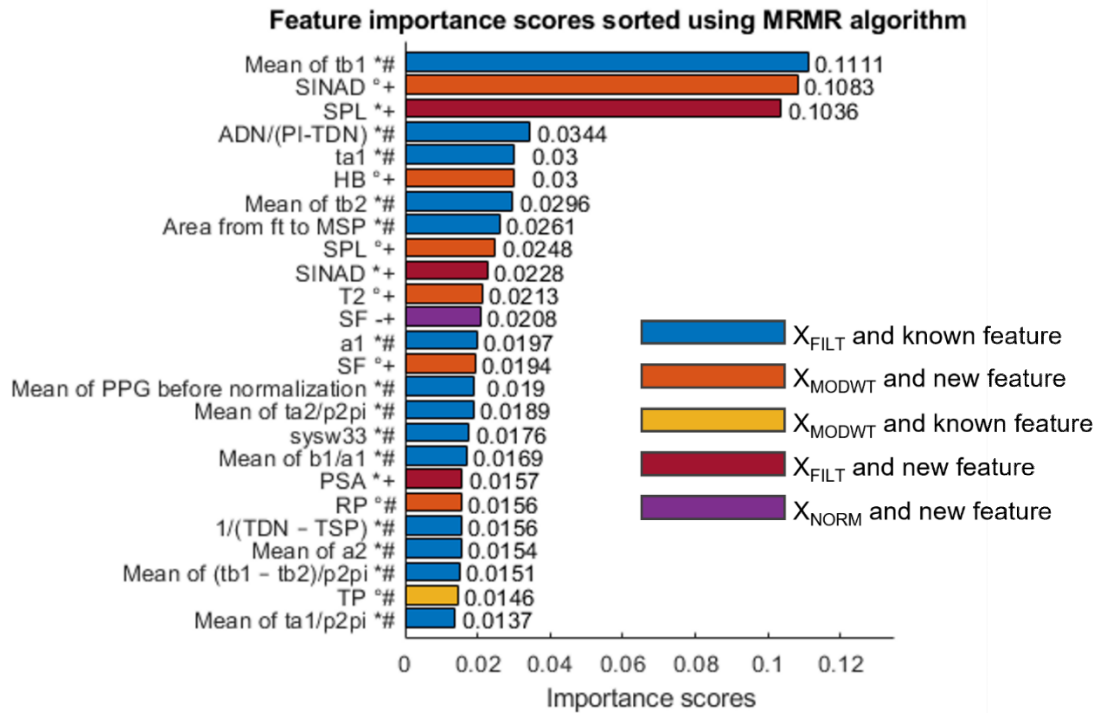


(a)



(b)

CHAPTER 1



(c)

Fig. 17. (a) Feature importance scores sorted using RReliefF algorithm for *DBP* measurement; (b) feature importance scores sorted using CFS algorithm for *DBP* measurement; (c) feature importance scores sorted using MRMR algorithm for *DBP* measurement. Feature labels are noted similarly to the previous figure.

Therefore, as well, for the case in which the diastolic values are taken, the three methods select several newly defined features for both the MODWT enhanced PPG signal and the filtered signal (x_{FILT}).

1.5 DISCUSSION

This section presents a summary of the results obtained during the features selection phase. It is observed that the features selected using the three methods, in both systolic and diastolic cases, include known features calculated after

CHAPTER 1

MODWT enhancement and new ones. Therefore, the following observations can be made.

Indeed, a number of features have been extracted from the PPG signal and subjected to investigation using three distinct selection methods. In particular, a number of already-known features have been calculated both before and after MODWT enhancement, demonstrating that the use of MODWT alone leads to improvements. This occurs with respect to the following features: TDN, which is selected by CFS for *SBP* and by RReliefF for both *SBP* (0.0046 score) and *DBP* (0.0043 score); ADP and ADN selected by MRMR for *SBP*; TDP selected by CFS for *DBP*; and TP selected by both CFS and MRMR for *DBP*.

On the other hand, several new features have been selected even if they are not extracted from MODWT enhanced signals: SPL is selected by MRMR for *SBP*; OB, MeaF, MedF and HB are selected by CFS for *DBP*; and SPL, SINAD, SF and PSA are selected by MRMR for *DBP*.

Moreover, the selection criteria indicate that several proposed new features are more useful than already known features in exploiting MODWT enhancement. For instance, SF is better than TDN according to RReliefF for *SBP*; T1 (score 0.12899 in **Fig. 16b**) is better than TDN (score 0.12041) according to CFS for *SBP*; T1 (score 0.032 in **Fig. 16c**) and T2 (score 0.0030) are better than ADN (score 0.028) according to MRMR for *SBP*; SF and CIF are better than TDN according to RReliefF for *DBP*; and many other features are better than TP and TDP according to CFS and MRMR for *DBP*.

Furthermore, features that are calculated simultaneously after MODWT enhancement and are novel have frequently been selected. For example, SF and CIF are among the best features according to RReliefF for both *SBP* (**Fig. 16a**) and *DBP* (**Fig. 17a**). SF has also been selected by MRMR for *DBP*. Other features that have been selected by more than one method are T1 and T2.

CHAPTER 1

In addition, it is important to note that many proposed features outperform already known features when their score is evaluated by CFS and MRMR for *DBP*, as shown in **Fig. 17b, c**.

Considering the previously discussed findings, the initial number of features, which was equal to 195, can be reduced by selecting the best significant features, shown in **Table A1** in the **Appendix A**. Several proposed features appear at least twice according to different selection methods, such as SF, CIF, T1, T2, SPL, TDN, TP, Area from DP to end, and so on. It should be noted that the shape factor SF, which has been proposed as a feature for PPG signals and is defined as the ratio between the RMS of the pulse and its mean absolute value, has been selected three times when applied to the enhanced signal x_{MODWT} . Moreover, the SF on the x_{MODWT} is greater than the SF on the x_{FILT} , since the DP is more pronounced in the x_{MODWT} . This feature is related to the shape of the pulse, which is known to depend strongly on vascular aging. Hence it may also be relevant for the evaluation of arterial stiffness, which is generally known to increase with age. These considerations demonstrate that the MODWT enhancement of the PPG signal, as well as the individuated new features, enables the extraction of significant information for BP that has the potential to improve its estimation through ML techniques.

1.6 CONCLUSION

This Chapter presents a discussion of the features of the PPG signal that are significant for BP measurements as well as the use of the MODWT to enhance the PPG signal.

Although the ABP signal allows for a more direct and accurate measurement of BP, it is obtained in an invasive manner, in contrast to the non-invasive acquisition of PPG signals, which can be easily and comfortably carried out, even

CHAPTER 1

at home. Hence, the utilization of PPG pulse enhancement through MODWT has been proposed, motivated by the fact that it exhibits greater similarity with the ABP pulse.

The first result of this study indicate that the enhanced signal facilitates more reliable extraction of characteristic points of the PPG pulse, such as the DP and the DN. Indeed, identifying the DP or the DN on PPG pulses can be challenging, as these points may be less pronounced or absent according to patient's age and condition. However, the proposed MODWT enhancement allows for the direct acquisition of characteristic points by considering signal valleys and peaks, resulting in a performance comparable to that of the purposely defined algorithm presented in [22], as demonstrated by an error analysis. For example, the DP was clearly marked in 95% of pulses (in contrast to only 1% for the untreated pulses), and that characteristic point exhibited a mean error of 0.04 s with respect to [22]. For systolic points, the mean and STD of the errors were found to be 0.0097 s and 0.0202 s, respectively, when the locations were obtained using a purposely defined already known algorithm and those obtained using the MODWT enhancement. For diastolic points, the mean and STD of the errors were found to be 0.0441 s and 0.0486 s, respectively. Finally, for dicrotic notch points, the mean and STD of the errors were found to be 0.0458 s and 0.0896 s, respectively. Indeed, as the second significant outcome following the extraction and selection of features, several new proposed features (as well as old features) obtained from x_{MODWT} have been found to be significant according to the scores provided by three feature evaluation methods, namely CFS, RReliefF and MRMR. It should be noted that these methods permit the selection of optimal features that are both relevant and non-redundant for the estimation of the variables of interest, which in this case are the systolic and diastolic BP values. Therefore, the findings presented in this Chapter provide a base for the development of BP estimation methods based on PPG signal analysis.

ML MODELS FOR SBP AND DBP ESTIMATION³

INTRODUCTION

In light of the spread of PPG for BP measurement, this Chapter aims to contribute to the ongoing research on ML models for estimating *SBP* and *DBP*. In **Chapter 1**, PPG signals were analyzed to identify the most significant features for BP estimation. This was achieved by employing several selection algorithms, including RReliefF, CFS, and MRMR. This methodology has led to the justification of the application of MODWT to enhance the single-site PPG signal and to the selection of new proposed features. Following this line of research, this Chapter focuses on the development of ML techniques to find the optimal algorithm for BP measurement. It demonstrates the value of the already analyzed features, with a particular emphasis on those selected through the MRMR method, including those obtained after the MODWT enhancement. The novelty of this research lies in the use of novel extracted features from PPG signals, which were evaluated for their significance using several criteria, and in the use of ML algorithms.

For this purpose, XGBoost models with Bayesian optimization and NN models were trained for regression using significant features selected with the MRMR

³ This Chapter is based on [2].

CHAPTER 2

algorithm. A comparison of results between XGBoost and NN models was presented and the improvements with respect to the literature, by using XGBoost models and the proposed features, are shown.

After the processing described in **Chapter 1** and the extraction of the features from the PPG signal, a dataset comprising 195 features for each PPG pulse and the target values of *SBP* and *DBP* measured on the ABP signal were obtained. Then, the dataset was reduced to *SBP* in the range of 80 mmHg to 180 mmHg and *DBP* in the range of 60 mmHg to 110 mmHg, in order to facilitate comparisons with the literature, given that similar distributions are used in other works [16], [17], [18], [21], [22], [54], [55], [56]. It is evident that *SBP* below 80 mmHg and *DBP* below 60 mmHg correspond to a severe hypotension condition while *SBP* above 180 mmHg and *DBP* above 110 mmHg correspond to a severe hypertension condition. However, in these cases, there were few observations in the initial dataset.

At the end of the processing, performed in MATLAB R2022a, the dataset contained 9.1×10^6 observations of PPG pulses from 1,080 patients. **Fig. 18** illustrates the distribution of systolic and diastolic BP values for the dataset processed in this study. The aforementioned dataset was used for the training and validation of ML models developed in the Python programming language, as will be discussed in the following sections. The dataset utilized for training and validation of ML models included 9×10^6 observations, with the 90% constituting the training set and the 10% constituting the validation set. Instead, the test set included 100,000 observations.

CHAPTER 2

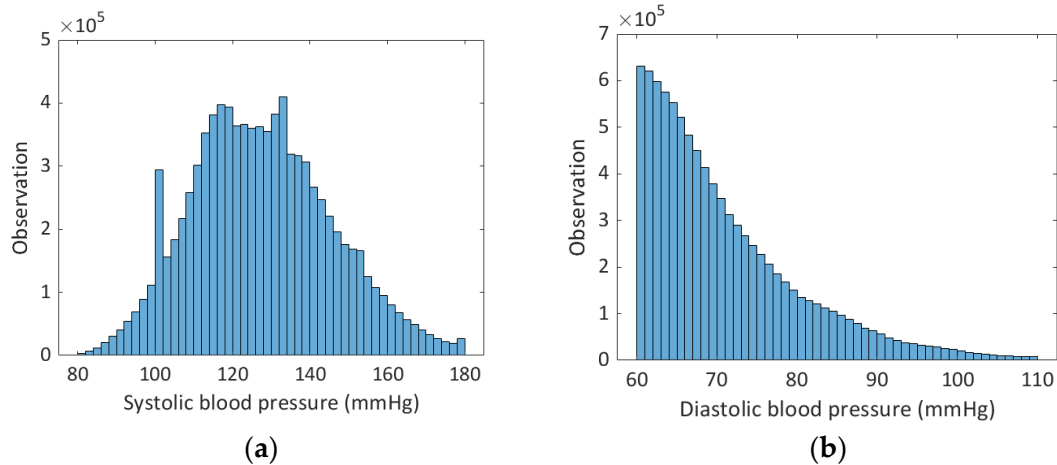


Fig. 18. (a) Systolic and (b) diastolic blood pressure occurrences in 2 mmHg bins. Only the observations with $80 \text{ mmHg} \leq SBP \leq 180 \text{ mmHg}$ and $60 \text{ mmHg} \leq DBP \leq 110 \text{ mmHg}$ were considered since outside these ranges there were few observations and, also, *DBP* less than 60 mmHg corresponds to severe hypertension condition.

2.1 MACHINE LEARNING MODELS

ML offers a suite of powerful techniques for the identification and evaluation of cardiovascular risk and health conditions. In this Chapter, the technique has been exploited to train supervised regression models capable of measuring BP based on features extracted from the PPG signal. For the purposes of training, each observation in the dataset is provided with systolic and diastolic labels derived from the corresponding ABP signal, which serves as the ground truth.

In this Chapter, an XGBoost model was trained due to its advantages, including execution speed and model performance, which proved to be suitable for the stated goal. In contrast, an NN model was trained to facilitate a comparison of the results. This approach was selected due to its prevalence among researches, as evidenced in [18], [22], [23], [57] and its characteristic of higher training speed. Moreover, XGBoost models have been utilized in the literature for a multitude of purposes, including wearable running monitoring [58], but have recently been employed for PPG signal processing to estimate blood glucose levels [59], blood

CHAPTER 2

pressure (utilizing multisite PPG acquisition and PTT features) [60], and vascular aging [61].

XGBoost is an efficient open-source implementation of the gradient boosting algorithm, and it is also available in Python using the Scikit-learn library, which is utilized in this study. Gradient boosting is a class of ensemble ML algorithms that can be used for both classification and regression. Ensemble models are based on decision tree models. In fact, trees are incorporated into the ensemble to rectify prediction errors that have been previously made. These models are fitted using a differentiable loss function and a gradient descent optimization algorithm in order to minimize the loss gradient. Furthermore, this algorithm provides hyperparameters that can be tuned, such as the number of trees or estimators, the learning rate, the row and column sampling rate, the maximum tree depth, the minimum tree weight, and the regularization terms alpha and lambda. Indeed, XGBoost adds a regularization term into the objective function, thereby reducing the model's susceptibility to overfitting.

Moreover, in this study, Bayesian hyper-parameter optimization [62] was used to adjust the hyper-parameters of the XGBoost model within the specified search space. Bayesian optimization permits the optimization of a proxy function rather than the true objective function. The search process balances exploration and exploitation, with the initial exploration phase aimed at building the surrogate function with the objective of minimizing the cost function at a global level. In this study, the Bayesian Optimization implementation provided by the Python library Scikit-optimize was used. The RMSE evaluation metric was defined using a Scikit-learn function in order to facilitate the conversion of the optimization problem into a minimization problem as required by Scikit-optimize.

The Bayesian optimization process was set providing the basic regressor, the search space, the evaluation metric, the cross-validation strategy (selected as a 7-fold approach), the maximum number of trials, and the optimizer parameters,

CHAPTER 2

which included the use of Gaussian Process (GP) for hyper-parameter optimization. Then, the optimal hyper-parameters were identified and utilized to instantiate the XGBoost model, which was subsequently trained using a 10-fold cross-validation strategy.

The next paragraphs will be concentrated on the XGBoost and NN models that were trained.

2.1.1 XGBOOST MODELS

The entire dataset was utilized for both *SBP* and *DBP*. The training and cross-validation were conducted using 9×10^6 observations (out of 9.1×10^6 observations). A total of 20 features for *SBP* and 25 features for *DBP* were selected, in order of highest MRMR score among the 195 features listed in **Chapter 1**, which include those derived from the MODWT enhanced PPG signal. The number of features used to train the models was selected using the RReliefF algorithm for both systolic and diastolic cases. Indeed, the RReliefF algorithm indicates that the 20 features for *SBP* and the 25 features for *DBP* have an importance score greater than 0.001. In consideration of the lower scores, it was determined that they were not significant, as they were related to uncorrelated features with respect to the output. The reduction in the number of features was implemented to decrease the complexity of the models and training. In fact, the removal of noisy features helps to reduce the memory and computational cost, while also helping to avoid overfitting. Moreover, the columns were normalized to the range $[0, 1]$ before the training.

Then, the first step consisted of finding the optimal hyper-parameters within a specified search space for the Bayesian optimization approach, utilizing the selected features for both *SBP* and *DBP* measurements.

CHAPTER 2

The search spaces and the best hyper-parameter values for *SBP* and *DBP* measurements are, respectively, shown in **Table 2** and **Table 3**.

Table 2. Search spaces and best values of hyper-parameters for *SBP*.

Hyper-Parameter	Range	Best
Learning rate	[0.01, 1.0]	0.226
Maximum tree depth	[2, 15]	15
Subsample	[0.1, 1.0]	0.894
Subsample ratio of columns by tree	[0.1, 1.0]	1.0
Lambda	[1×10^{-10} , 200]	120.0
Alpha	[1×10^{-10} , 200]	1×10^{-10}
Estimators	[50, 5100]	5000

Table 3. Search spaces and the best values of hyper-parameters for *DBP*.

Hyper-Parameter	Range	Best
Learning rate	[0.01, 1.0]	0.136
Maximum tree depth	[2, 20]	15
Subsample	[0.1, 1.0]	0.894
Subsample ratio of columns by tree	[0.1, 1.0]	1.0
Lambda	[1×10^{-9} , 200]	120.0
Alpha	[1×10^{-10} , 200]	1×10^{-10}
Estimators	[50, 6000]	5200

The following section provides an explanation of the hyper-parameters utilized in XGBoost. The learning rate is the step size shrinkage used for the update to enhance the model's robustness and prevent overfitting by reducing the feature weights. It is selected within the range [0, 1] with typical values in [0.01, 0.2]. The maximum depth of a tree is employed to regulate the phenomenon of overfitting. As the depth of the tree increases, the model becomes more intricate and more susceptible to overfitting. The value 0 is only accepted in a loss-guided growing policy, while large values result in a more aggressive consumption of memory. Any positive value is acceptable, with typical values in the range [3, 10]. In this study, trial and error was employed to modify the upper bound of the range in

CHAPTER 2

order to achieve more optimal results. The subsample represents the fraction of observations to be randomly sampled for each tree. Its purpose is to prevent overfitting. In fact, lower values make the algorithm more conservative, while too small values might lead to under-fitting. For this reason, the range is $[0, 1]$ and typical values are in $[0.5, 1]$. The subsample ratio of columns by tree represents the subsample ratio of columns when constructing each tree. This parameter has a range of $[0, 1]$ and the default value is 1. Lambda is the L2 regularization term on weights, and an increase in this value makes the model more conservative. Alpha is the L1 regularization term on weights and it is used in cases of very high dimensionality so that the algorithm runs faster when implemented. Finally, estimators are the number of trees in an XGBoost model. For the three last hyper-parameters, a trial-and-error method was used to define the range.

2.1.2 NN MODELS

In Python, TensorFlow 2.9.1 was used to define a sequential model with an input layer of size n , nine hidden layers, and an output layer. The activation function selected for each layer was the Rectified Linear Unit (ReLU). The number of hidden layers and neurons was determined through a series of trials. The NN model is shown in **Fig. 19**. For *SBP* estimation, $n = 20$ while for *DBP* estimation, $n = 25$.

CHAPTER 2

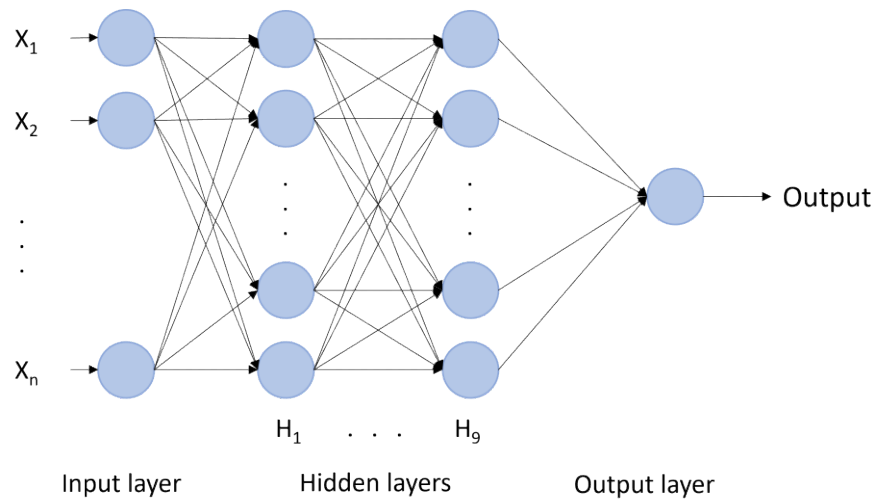


Fig. 19. NN with nine hidden layers with 1024, 1024, 1024, 512, 512, 512, 128, 64, and 64 neurons.

Moreover, several optimizers were tested including Adadelta, Adagrad, Adam, Adamax, Nadam, RMSprop, and SGD. However, the Nesterov-accelerated Adaptive Moment Estimation (Nadam) algorithm yielded the most optimal results for both *SBP* and *DBP* estimations.

The fit was made using a batch size of 4,096, 150 epochs, and a validation split of 0.2.

The optimal NN architecture was determined through a process of trial and error, with the addition of hidden layers being identified as the most promising approach. The ReLU activation function was selected due to its suitability for normalized inputs, which has resulted in enhanced outcomes. The batch size must be selected to align with the memory requirements of the GPU and the CPU architecture. Values below the minimum required for optimal performance were not considered, as they would exceed the memory constraints of the system. Conversely, values above the maximum were not permitted, as they would exceed the memory limitations of the CPU. Therefore, the maximum feasible batch size was established. The number of epochs was selected in the range [50, 200] but no improvements were observed beyond the 150th epoch.

2.2 RESULTS AND DISCUSSION

This section will demonstrate the efficacy of ML algorithms. The two models, XGBoost and NN, were trained using the features selected by the MRMR algorithm, which included the new features obtained on MODWT-enhanced PPG pulses. As previously demonstrated, the application of MODWT to the PPG signal results in enhanced signal quality, facilitating the identification of characteristic points and rendering the signal more similar to the ABP signal.

The criteria used to evaluate the performance of ML models for estimating BP are the RMSE, Mean Absolute Error (MAE), correlation coefficient (R), and Mean Error (ME).

The results were then compared with other methods reported in the literature in addition to the standards for BP measurement, which are focused on the classification of hypertension states. The predicted BP values from the regression model and the true values were employed to validate the correct classification into the seven classes delineated by the guideline, taking into account the range of values for *SBP* and *DBP*. The classification results were evaluated using a confusion matrix.

2.2.1 TRAINING AND TEST OF XGBOOST AND NN MODELS

This paragraph presents the results obtained following training and validation. **Table 4** presents the results of XGBoost and NN models, evaluated in terms of RMSE and MAE.

CHAPTER 2

Table 4. Validation results for *SBP* and *DBP* estimations.

Model		RMSE (mmHg)	MAE (mmHg)
XGBoost	SBP	5.60	3.11
	DBP	3.92	2.09
NN	SBP	7.80	5.00
	DBP	5.56	3.53

After validation, a test was conducted on both models using a set of 100,000 new observations out of the entire dataset of 9.1×10^6 observations (not included in the training set). The results were presented in **Table 5**, which reports the performance parameters for *SBP*, *DBP*, and Mean Arterial BP (MAP).

In addition to *SBP* and *DBP*, MAP was considered because it is linked to the total peripheral resistance and to cardiac output and is associated with HR [63], [64]. MAP is a frequently utilized BP parameter. It is defined as the average pressure of the artery of a subject during one cardiac cycle (4). It is considered to be a superior indicator of organ perfusion in comparison to *SBP* [65].

$$MAP = \frac{SBP + 2 \cdot DBP}{3}, \quad (4)$$

Table 5. Test results using XGBoost and NN models.

Model		RMSE (mmHg)	MAE (mmHg)	R	ME (mmHg)
XGBoost	SBP	5.67	3.12	0.95	0.020
	DBP	3.95	2.11	0.91	-0.001
	MAP	3.24	2.01	0.93	0.006
NN	SBP	7.81	5.00	0.90	-0.420
	DBP	5.60	3.55	0.81	-0.250
	MAP	4.56	3.12	0.85	-0.310

CHAPTER 2

The results reported in **Table 4** and **Table 5** demonstrate that the utilization of XGBoost models rather than NN yields superior outcomes for the measurements of both systolic and diastolic pressure.

Moreover, the results for XGBoost models obtained in the final test phase, as shown in **Table 5**, are similar and confirm the ones obtained during the training and cross-validation phase, as shown in **Table 4**.

Fig. 20 depicts the error probability densities of *SBP*, *DBP* and *MAP*. It is evident that the errors obtained using the XGBoost model exhibit a narrower and more concentrated distribution around zero than those obtained using the NN model. As illustrated in **Fig. 21**, the XGBoost models yield the most accurate predictions, with R values consistently higher than those obtained using the NN models.

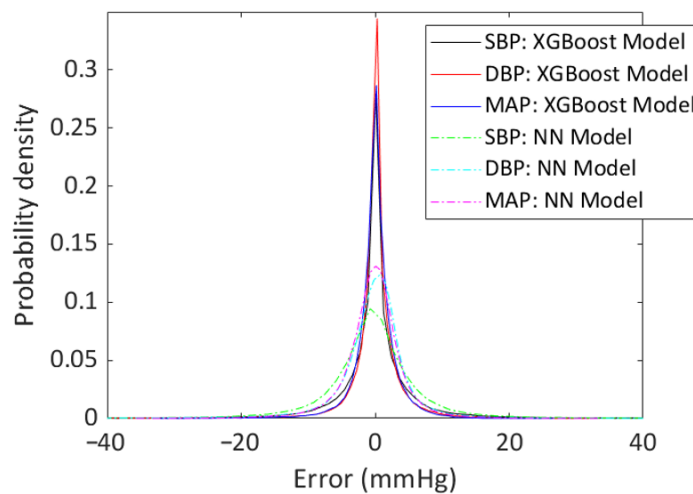
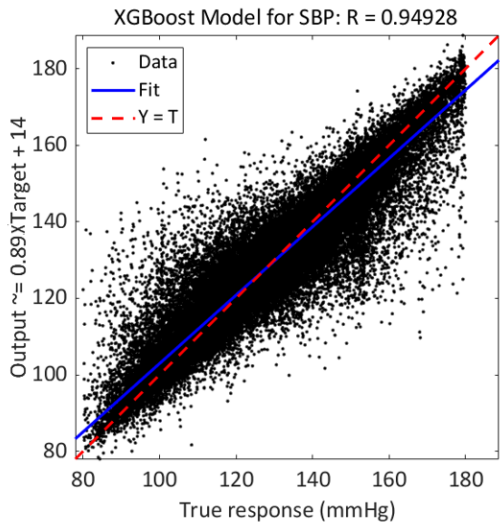
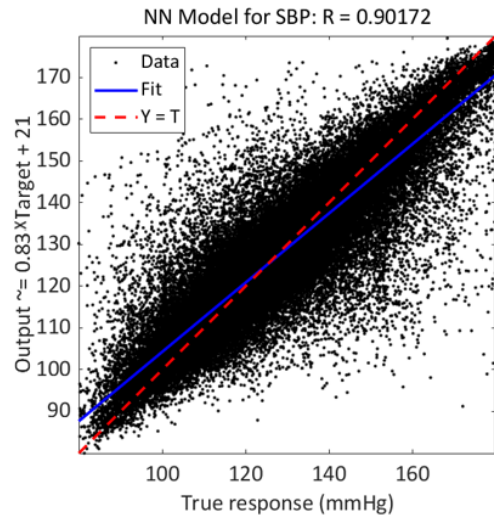


Fig. 20. Error probability density of *SBP*, *DBP*, and *MAP* estimations. Errors were defined as the difference between the predicted pressures (using XGBoost model or NN model) and measured ones; then, their histograms were normalized to obtain the probability densities shown in the plot.

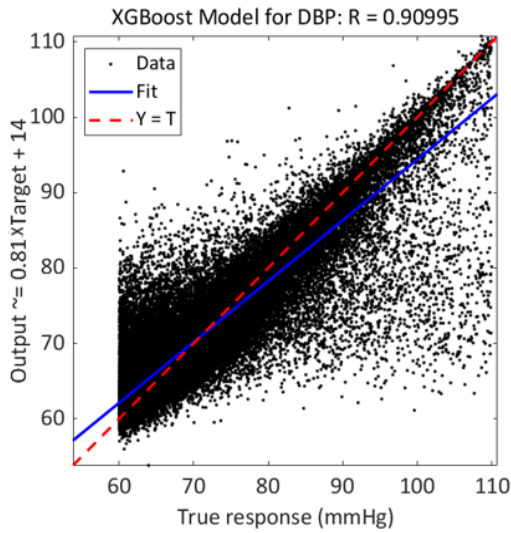
CHAPTER 2



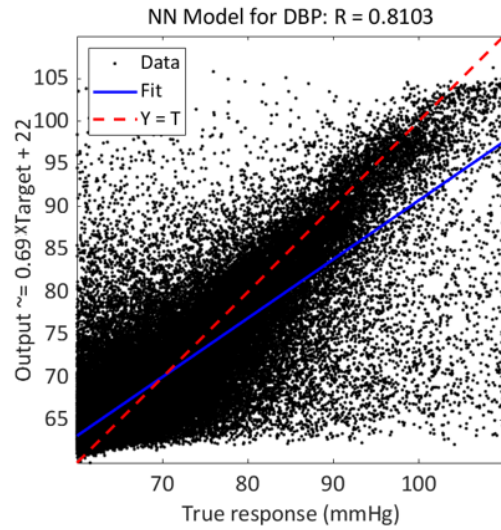
(a)



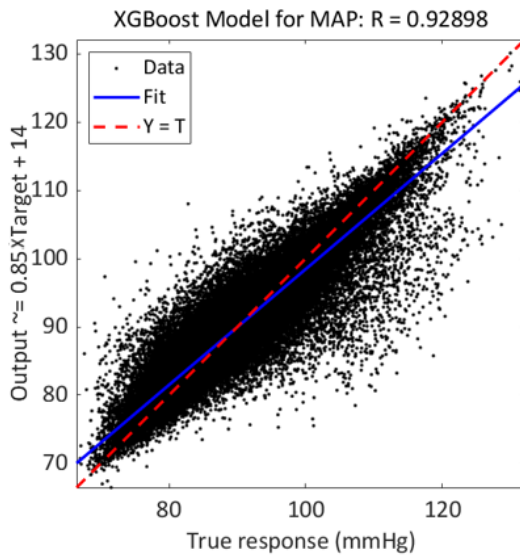
(b)



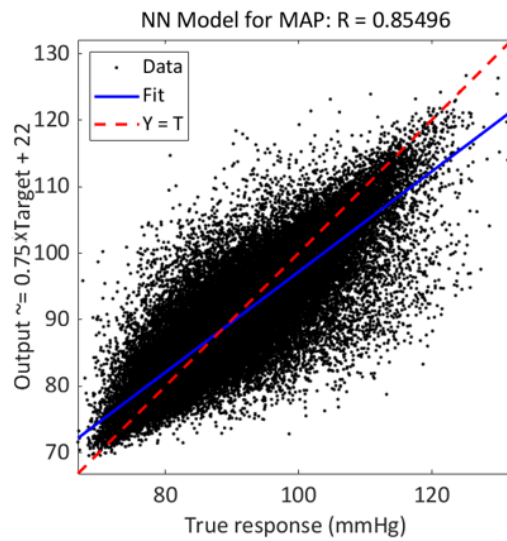
(c)



(d)



(e)



(f)

CHAPTER 2

Fig. 21. (a, c, e) Regression of the predicted output and true response for *SBP*, *DBP*, and *MAP* estimations using the XGBoost model; (b, d, f) Regression of the predicted output and true response for *SBP*, *DBP*, and *MAP* estimations using the NN model.

During the training phase, it was observed that the training time for NN was significantly shorter than that for the XGBoost models. The inference time was found to be significantly reduced for XGBoost models, which suggests that the trained model could be used for real-time predictions, thus facilitating continuous monitoring. Given the computational complexity of current implementations for feature extraction and ML models, it is not feasible to perform onboard processing on a wearable device. Consequently, a cloud-based solution is required. The objective is to streamline feature extraction by including only those selected in the present study and to simplify models to permit onboard processing, thereby reducing the computational complexity and assessing the minimal hardware requirements.

2.2.2 COMPARISON WITH OTHER METHODS

Comparing results with literature is challenging due to the disparate evaluation criteria and distinct datasets. In this Chapter, the type of algorithms and the use of features have been employed as criteria for selecting and identifying other works in the literature for comparison. In this context, the criterion is the training of ML algorithms with features extracted from the PPG signal, namely, the methodology employed in the research.

In **Table 6**, the performance of other methods is shown.

CHAPTER 2

Table 6. Comparison with other works.

Work	Method	Data Size	Performance Evaluation	SBP	DBP
Kachuee et al. [18]	SVM	MIMIC II (1,000 subjects)	RMSE	/	/
			MAE	12.38	6.34
			R	/	/
			ME	/	/
Kim et al. [66]	ANN	180 recordings, 45 subjects	RMSE	/	/
			MAE	4.53	/
			R	/	/
			ME	/	/
Cattivelli et al. [67]	Proprietary algorithm	MIMIC database (34 recordings, 25 subjects)	RMSE	8.37	5.92
			MAE	/	/
			R	/	/
			ME	/	/
Zhang et al. [68]	SVM	7,000 samples from 32 patients	RMSE	/	/
			MAE	11.64	7.62
			R	/	/
			ME	/	/
Zadi et al. [69]	Autoregressive moving average (ARMA) models	15 subjects	RMSE	6.49	4.33
			MAE	/	/
			R	/	/
			ME	/	/
Chowdhury et al. [19]	GPR	222 recordings, 126 subjects	RMSE	6.74	3.59
			MAE	3.02	1.74
			R	0.95	0.96
			ME	/	/
Hasanzadeh et al. [21]	AdaBoost	MIMIC II 942 subjects	RMSE	/	/
			MAE	8.22	4.17
			R	0.78	0.72
			ME	0.09	0.23
Kachuee et al. [54]	AdaBoost	1,000 subjects	RMSE	/	/
			MAE	8.21	4.31
			R	/	/
			ME	/	/
Wang et al. [70]	ANN	58,795 PPG samples	RMSE	/	/
			MAE	4.02	2.27
			R	/	/
			ME	/	/
Kurylyak et al. [23]	ANN	15,000 PPG heartbeats	RMSE	/	/
			MAE	3.80	2.21
			R	/	/
			ME	/	/

CHAPTER 2

Fleischhauer et al. [71]	XGBoost	MIMIC, Queensland, PPG BP (273 subjects and 259,986 single beats)	RMSE	/	/
			MAE	6.366	/
			R	0.874	/
			ME	/	/
Liu et al. [72]	SVR	MIMIC II 910 good PPG pulses cycles	RMSE	/	/
			MAE	8.54	4.34
			R	/	/
			ME	/	/
Zhang et al. [73]	Gradient Boosting Regressor (GBR)	MIMIC II 2,842 samples from 12,000 data points	RMSE	/	/
			MAE	4.33	2.54
			R	/	/
			ME	/	/
Proposed method	XGBoost	MIMIC III 9.1×10^6 PPG pulses from 1080 subjects	RMSE	5.67	3.95
			MAE	3.12	2.11
			R	0.95	0.91
			ME	0.01	0.02

A comparison with other works has demonstrated that the trained models, which employ XGBoost, the MRMR selection algorithm, and features derived from MODWT, have the capacity to enhance PPG pulses, with the concomitant reduction of estimation errors for both systolic and diastolic BP measurements. It is noteworthy that XGBoost is derivative-free, which may confer an advantage when the fitting problem exhibits a considerable degree of freedom. Furthermore, the utilization of MODWT enhancement has permitted the accentuation of distinctive characteristics within PPG pulses, such as the diastolic point. This has the potential to be a critical factor in achieving such results. It is evident that the proposed method has yielded a more accurate *SBP* measurement than the other methods presented in **Table 6**. As previously stated, a direct comparison of results is challenging due to the use of disparate datasets and ML algorithms, as detailed in **Table 6**. For example, it should be noted that Chowdhury et al. [19] obtained a smaller RMSE for *DBP*, which may be attributed to the distinct dataset utilized and the incorporation of demographic features that serve as a robust predictor of BP values. These features include

CHAPTER 2

gender, age, and height, which are known to influence the shape of the PPG pulse and arterial stiffness. Considering Zhang et al. [73], they employ a GBR algorithm, resulting in slightly inferior outcomes when compared to those reported in this Chapter, as well as the results reported by Fleischhauer et al. [71] using XGBoost are inferior to those of this Chapter. In fact, the optimal results are achieved through the implementation of Bayesian optimization for the XGBoost models and a distinct selection of features, which were also obtained following MODWT enhancement. This approach appears to offer a more effective solution than other ML algorithms, as evidenced by the results presented in **Table 6**.

2.2.3 COMPLIANCE TO STANDARDS AND CLASSIFICATION GUIDELINES

The accurate estimation of BP is of paramount importance for the detection of hypertension and the assessment of overall health status. Consequently, the accuracy requirements for BP measurement devices and methods have been standardized.

In this Chapter, the protocols proposed by the Association for the Advancement of Medical Instrumentation (AAMI) [74], [75] and by the British Hypertension Society (BHS) [76] were considered in order to make a comparison with the results reported in this study as also made in [17], [19], [20], [21], [77], [78], [79].

As the most favorable outcomes were achieved with the XGBoost models, rather than the NN models, the subsequent comparisons will focus exclusively on the XGBoost models. As shown in **Table 7 - Table 10**, the proposed method is in compliance with the AAMI and BHS grade A standards. The dataset included 1,080 patients and a total of 9.1×10^6 observations of PPG pulses.

CHAPTER 2

Table 7. Comparison of results for the validation set with AAMI standard.

		ME (mmHg)	STD (mmHg)
Results	SBP	0.009	5.60
	DBP	0.019	3.92
	MAP	0.0157	3.21
AAMI	SBP	≤5	≤8
	DBP		

Table 8. Comparison of results for the test set with AAMI standard.

		ME (mmHg)	STD (mmHg)
Results	SBP	0.020	5.67
	DBP	-0.001	3.95
	MAP	0.006	3.24
AAMI	SBP	≤5	≤8
	DBP		

Table 9. Comparison of results for the validation set with BHS standard.

		Cumulative Error Percentage		
		≤5 mmHg	≤10 mmHg	≤15 mmHg
Results	SBP	80.85%	93.00%	96.84%
	DBP	89.56%	96.86%	98.74%
	MAP	90.89%	98.18%	99.49%
BHS	Grade A	60%	85%	95%
	Grade B	50%	75%	90%
	Grade C	40%	65%	85%

Table 10. Comparison of results for the test set with BHS standard.

		Cumulative Error Percentage		
		≤5 mmHg	≤10 mmHg	≤15 mmHg
Results	SBP	80.96%	92.91%	96.73%
	DBP	89.48%	96.87%	98.68%
	MAP	90.84%	98.07%	99.44%
BHS	Grade A	60%	85%	95%
	Grade B	50%	75%	90%
	Grade C	40%	65%	85%

CHAPTER 2

As can be observed in **Table 7** and **Table 8**, the results align with the AAMI standard requirements. According to this protocol, the mean and the STD of the errors for both *SBP* and *DBP* estimations should not exceed 5 mmHg and 8 mmHg, respectively. Furthermore, the BHS standard is met, as the absolute error of over 60% of the data is less than 5 mmHg. Consequently, the method is classified as Grade A.

Moreover, as established in [21], another guideline was used to evaluate the regression models. For this purpose, the guideline [80] provided by the European Society of Hypertension (ESH) and the European Society of Cardiology (ESC) was considered. This guideline focuses on the state of hypertension and, in fact, categorizes it into seven classes:

- Optimal: if $SBP < 120$ mmHg and $DBP < 80$ mmHg;
- Normal: if 120 mmHg $\leq SBP \leq 129$ mmHg and/or 80 mmHg $\leq DBP \leq 84$ mmHg;
- High Normal: if 130 mmHg $\leq SBP \leq 139$ mmHg and/or 85 mmHg $\leq DBP \leq 89$ mmHg;
- Grade 1 Hypertension: if 140 mmHg $< SBP \leq 159$ mmHg and/or 90 mmHg $\leq DBP \leq 99$ mmHg;
- Grade 2 Hypertension: if 160 mmHg $\leq SBP \leq 179$ mmHg and/or 100 mmHg $\leq DBP \leq 109$ mmHg;
- Grade 3 Hypertension: if $SBP \geq 180$ mmHg and/or $DBP \geq 110$ mmHg;
- Isolated Systolic Hypertension: if $SBP \geq 140$ mmHg and $DBP < 90$ mmHg.

Since hypertension represents a state of health that is of interest for identification purposes, ESH/ESC guidelines have been used to evaluate the regression models, with the predicted values being classified into seven classes. The BP ground truth and the BP predicted by the XGBoost model were classified according to the previously described scheme to evaluate the consistency between the classified predicted values and the classified true values in the different states of

CHAPTER 2

hypertension. The results are shown in **Fig. 22** and in **Table 11**. The table presents the accuracy, sensitivity, specificity, and F1-score values. Two classes exhibited low sensitivity: “Grade 3 Hypertension” and “Isolated Systolic Hypertension”. The low sensitivity can be attributed to the limited number of training cases in the dataset. It is evident that “Grade 3 Hypertension” represents a critical condition, while “Isolated Systolic Hypertension” is observed with low frequency in young and middle-aged subjects.

Output Class	Grade 1 Hypertension	14,325 14.3%	1163 1.2%	8 0.0%	1246 1.2%	417 0.4%	613 0.6%	108 0.1%	80.1% 19.9%
	Grade 2 Hypertension	454 0.5%	3214 3.2%	58 0.1%	44 0.0%	1 0.0%	85 0.1%	1 0.0%	83.3% 16.7%
	Grade 3 Hypertension	0 0.0%	61 0.1%	30 0.0%	1 0.0%	0 0.0%	1 0.0%	0 0.0%	32.3% 67.7%
	High Normal	2491 2.5%	154 0.2%	3 0.0%	15,629 15.6%	528 0.5%	3036 3.0%	539 0.5%	69.8% 30.2%
	Isolated Systolic Hypertension	502 0.5%	11 0.0%	1 0.0%	453 0.5%	420 0.4%	69 0.1%	16 0.0%	28.5% 71.5%
	Normal	919 0.9%	171 0.2%	5 0.0%	3520 3.5%	59 0.1%	16,392 16.4%	3197 3.2%	67.6% 32.4%
	Optimal	205 0.2%	99 0.1%	12 0.0%	420 0.4%	8 0.0%	2330 2.3%	26,981 27.0%	89.8% 10.2%
		75.8% 24.2%	66.0% 34.0%	25.6% 74.4%	73.3% 26.7%	29.3% 70.7%	72.8% 27.2%	87.5% 12.5%	77.0% 23.0%
	Grade 1 Hypertension	Grade 2 Hypertension	Grade 3 Hypertension	High Normal	Isolated Systolic Hypertension	Normal	Optimal		
	Target Class								

Fig. 22. Confusion matrix for BP level classification according to ESH/ESC guidelines.

CHAPTER 2

Table 11. Results of BP level classification according to ESH/ESC guidelines.

Class	Accuracy	Sensitivity	Specificity	F1-Score	Actual Class Members
Grade 1 Hypertension	91.9%	75.8%	95.6%	77.9%	18.9%
Grade 2 Hypertension	97.7%	66.0%	99.3%	73.6%	4.9%
Grade 3 Hypertension	99.8%	25.6%	99.9%	28.6%	0.1%
High Normal	87.5%	73.3%	91.4%	71.4%	21.3%
Isolated Systolic Hypertension	97.9%	29.3%	98.9%	28.9%	1.4%
Normal	86.0%	72.8%	89.8%	70.1%	22.5%
Optimal	93.1%	87.5%	95.6%	88.6%	30.8%
Average	90.3%	76.9%	93.5%	77.0%	

As is possible to see in **Table 11**, the average of accuracy, sensitivity, specificity, and F1-score are, respectively, 90.3%, 76.9%, 93.5%, and 77.0%.

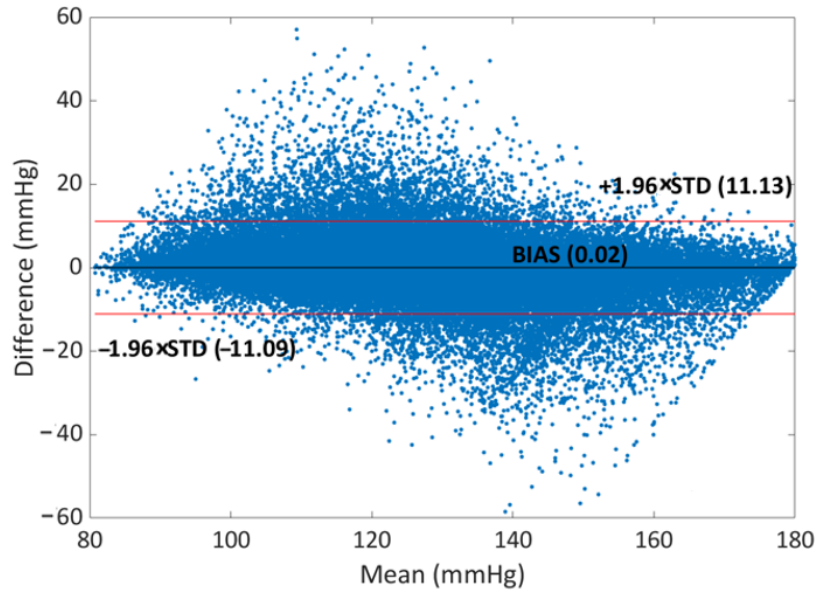
2.2.4 BLAND–ALTMAN ANALYSIS

Finally, to test the validity of the prediction of the XGBoost models for *SBP*, *DBP*, and *MAP*, a Bland–Altman analysis was performed. This analysis was used to determine the limits of agreement (LOA) between two different measurements in clinical practice, as described in [81], [82]. The mean and STD of the differences between the two measurements are used to determine the statistical limits. The mean bias (mean of the differences) and its LOA are provided by the Bland–Altman plot, which is shown in **Fig. 23**.

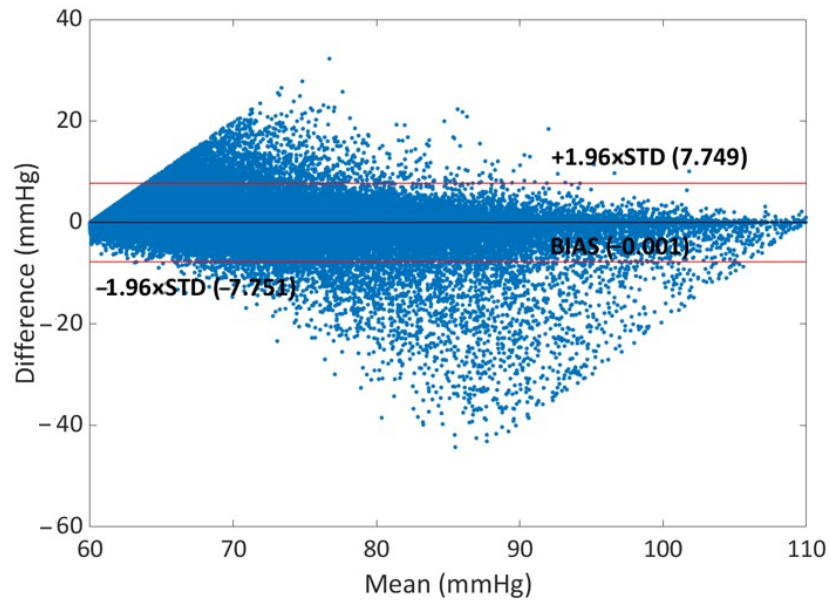
The black line represents the mean of the differences (BIAS), while the red lines represent the upper and lower limits ($\text{BIAS} \pm 1.96 \times \text{STD}$) of the LOA [83]. The LOA for errors of *SBP* is $[-11.09, 11.13]$ mmHg and the percentage of points outside the LOA is 5.91%; the LOA for errors of *DBP* is $[-7.75, 7.75]$ mmHg with a percentage of 5.08% points outside while for *MAP* the LOA for errors is $[6.35,$

CHAPTER 2

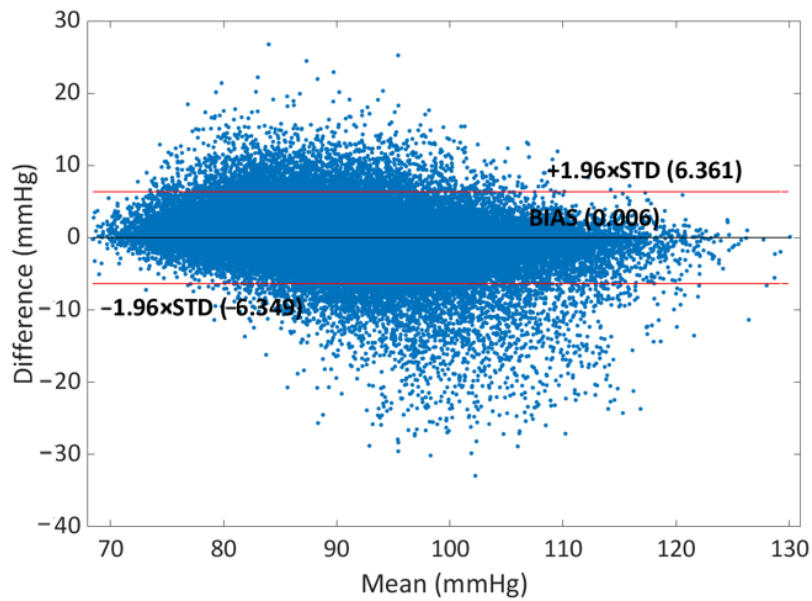
6.36] mmHg with a percentage of 5.73% points outside. In light of these findings, it can be reasonably concluded that the proposed model exhibits a high degree of accuracy.



(a)



(b)



(c)

Fig. 23. Bland–Altman plots for (a) *SBP*, (b) *DBP*, and (c) *MAP*.

2.3 CONCLUSION

The possibility of measuring BP by using PPG signals is advantageous for the monitoring of this vital sign since it avoids the use of cumbersome cuff-based devices, and it allows continuous monitoring. Nevertheless, the estimation of BP using PPG is subject to several criticalities and limitations, including the need to eliminate noise, perform individual calibration, and address calibration drift.

In **Chapter 1**, the focus was on the extraction of new features from PPG signals, including those obtained after the enhancement with MODWT. The significance of these features was evaluated by using several criteria, such as MRMR. In this Chapter, the features selected by the MRMR algorithm were used to train ML models to estimate BP, giving improved results.

Among the ML models, the XGBoost model with Bayesian optimization was found to be most suitable for estimating purposes, yielding superior results to an NN model trained on the same data. In fact, the XGBoost model, when combined with the use of novel features, demonstrated an improvement in systolic BP

CHAPTER 2

measurement compared to literature.

In addition, the *SBP* and *DBP* estimators were found to meet the requirements of the AAMI and BHS grade A standards, and also yielded satisfactory classification results in accordance with the ESH/ESC guideline.

PERFORMANCE COMPARISON OF ML MODELS FOR SBP AND DBP ESTIMATION⁴

INTRODUCTION

The need to develop non-invasive or minimally invasive treatments for patients, particularly in the context of vital sign acquisition and surgical procedures is spreading. This is because infections and pain can significantly worsen postoperative recovery and increase the risk of complications, particularly in the context of invasive BP measurement and surgery [20], [73], [85], [86].

This need for non-invasive, cuff-less, and continuous monitoring of BP has led to the use of PPG.

However, estimating BP using PPG is not straightforward due to the presence of noise, such as motion artifacts. Motion artifacts are caused by the subject's involuntary or voluntary movements, as well as respiration. These artifacts compromise the accuracy and reliability of the PPG signal, so it is critical to identify and implement algorithms that eliminate them [87], [88], [89]. In such instances, however, these artifacts can and should be employed to monitor additional parameters, such as eye blink [90], [91]. The present study did not address the implementation of motion artifact elimination algorithms, as its

⁴ This Chapter is based on [84].

CHAPTER 3

objective has been the analysis of the performance of several ML models.

It is evident that there is a significant interest in enhancing BP estimation through PPG and ML algorithms. In **Chapter 2**, XGBoost models and NN models, have been trained for regression using a set of significant features.

Nevertheless, further investigation is required to determine the optimal choice of features among the three-selection algorithm and to assess the accuracy of different ML models. This is why, in this Chapter, RMSE, MAE, and the training times obtained by the ML models using different selections of features, including new ones extracted on the MODWT enhanced PPG signal and features already known in literature, are compared. Two sets of features were obtained for each feature selection algorithm to analyze the impact of introducing new, significant features extracted from the MODWT enhanced signal. Additionally, the results obtained by using three different feature selection algorithms to identify the optimal results regardless of the ML model used were compared. Moreover, multiple ML algorithms have been trained using the most significant features selected by the RReliefF and MRMR algorithms, allowing for a comparison to be made. The ML algorithms were selected based on their demonstrated efficacy and serve as the fundamental components of numerous additional techniques. The objective of this overview is to provide a comprehensive and valuable insight into this field. Furthermore, one of the largest available datasets was selected for analysis. By selecting increasing portions of it, it was possible to understand the relationship between accuracy and training set size. This will provide useful guidance for designing the experiments. It is crucial to expand the dataset to assess its accuracy and the time required for training. This allowed to definitively state the optimal size, given the considerable burden of data collection, which necessitates the recruitment of numerous subjects. As a matter of fact, a smaller size will reduce training time and computational cost. This aspect was rigorously examined across multiple ML models and a range of training set sizes, including

CHAPTER 3

a comprehensive investigation of the XGBoost model.

3.1 MACHINE LEARNING MODELS AND DATASET

This section serves to introduce the ML models that will be discussed. ML is an invaluable tool in a multitude of research areas, particularly for classification and prediction purposes. The efficacy of several ML models was assessed in order to identify the most effective approach for estimating BP from PPG signals. Many of these models have been previously utilized in the existing literature, as referenced in [18], [19], [21], [23], [54], [66], [68], [69], [70], [92], [93], [94], [95]. The following ML models were investigated: XGBoost models [96], NNs [97], LR models [98], RTs [99], SVMs [100], GPR models [101], Kernel Approximation Regression (KAR) models [102], Ensemble of trees (ETs) [103]. XGBoost models represent the optimal ML algorithms based on a set of decision trees, utilizing a gradient boosting framework to minimize errors through gradient descent algorithms. It employs the most effective hardware and software optimization techniques to achieve superior results with minimal computing resources. NNs represent a subset of ML. The structure of NNs is based on the architecture of the human brain. They are designed to analyze and process tasks in a manner analogous to the manner in which the brain processes information. NNs are structured in a layered configuration, comprising an input layer, one or more hidden layers, and an output layer. Each layer is composed of neurons that are linked to other neurons through weighted connections and are activated above a specified threshold. LR models are designed to model the relationship between two variables by fitting a linear equation to observed data. In a given statistical model, one variable is designated as the explanatory variable, while the other is designated as the dependent variable. LR is a statistical method employed in the

CHAPTER 3

fields of data science and ML for the purpose of predictive analysis. RTs are a fundamental non-linear model that can effectively capture intricate relationships between features and targets. A data splitting approach is employed, guided by specific criteria, with the objective of identifying homogeneous groups based on their predefined hyperparameters. SVMs are a class of linear models that are particularly suited to the classification and regression problems that arise in many fields of scientific and engineering research. SVMs are capable of solving both linear and non-linear problems. The algorithm generates a line or hyperplane that separates the data into distinct classes. GPR models provide a nonparametric, Bayesian methodology for regression analysis that has become standard in ML applications due to their representation flexibility. In the context of nonlinear regression with a considerable number of observations, the KAR model represents the optimal statistical choice. This study employs a Gaussian kernel for the nonlinear regression of data sets comprising a considerable number of observations. The kernel function maps the predictor variables into a high-dimensional space, after which a linear SVM or an ordinary least squares linear regression model is fitted to the transformed predictor variables. The efficacy of ETs is enhanced when compared to that of single decision trees, due to the fact that they combine multiple decision trees in order to achieve superior predictive performance. This study employs two techniques: bagging (Bootstrap Aggregation), which serves to reduce the variance of a decision tree, and gradient boosting, which represents an extension of the boosting method that employs the gradient descent algorithm for the purpose of optimizing any differentiable loss function. The implementation of gradient boosting is observed to be slower than that of extreme gradient boosting, as represented by the XGBoost model. This study has examined all of the aforementioned models using the MIMIC III Waveform Database. The data has been pre-processed as presented in **Chapter**

CHAPTER 3

1. The final dataset contains 195 features for each PPG pulse and the target values of *SBP* and *DBP* from the *ABP* signal. **Fig. 24** shows an overview of the data flow.

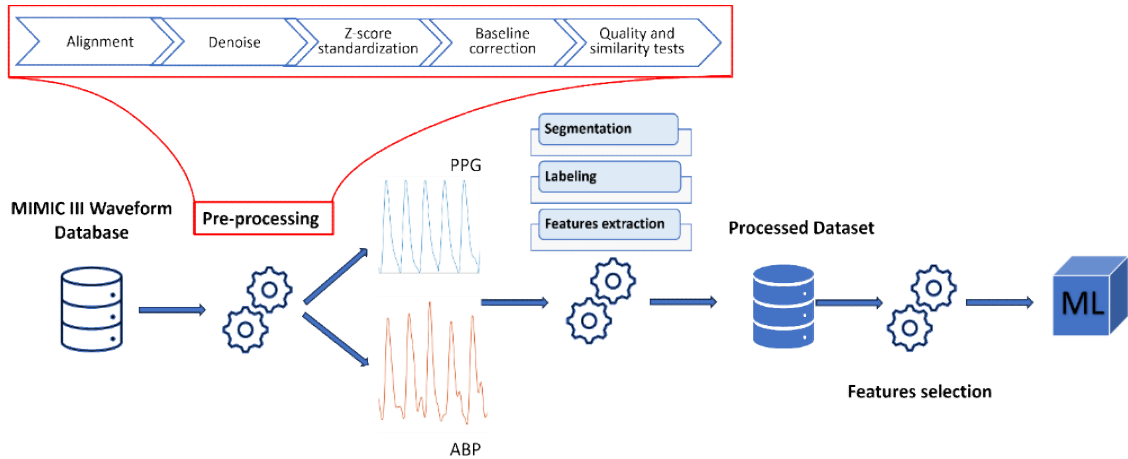


Fig. 24. Overview of data flow.

3.2 COMPARISON OF RESULTS USING ML AND FEATURES SELECTED BY THREE SELECTION ALGORITHMS

This section evaluates the performance obtained by considering different sets of features. Three feature selection methods were used to choose the best features from two large sets for both *SBP* and *DBP* measurements, resulting in 12 smaller sets overall.

The first large set, that will be called *full standard set* \mathfrak{F}_S , contains 142 features already found in the literature; the second large set of 195 features, is expanded with features obtained after the enhancement of the PPG signal using the MODWT, and will be called *full expanded set* \mathfrak{F}_E .

To make ML training more accessible, the large set of features \mathfrak{F}_S and \mathfrak{F}_E have to be reduced in a logical manner. To achieve this, three selection methods were

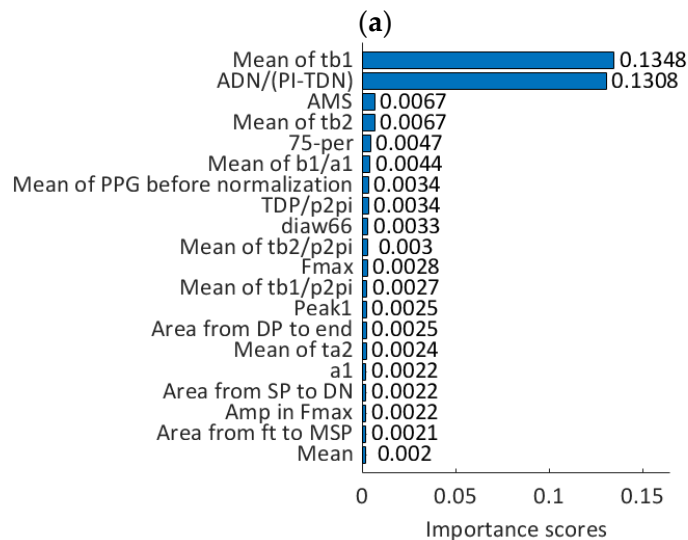
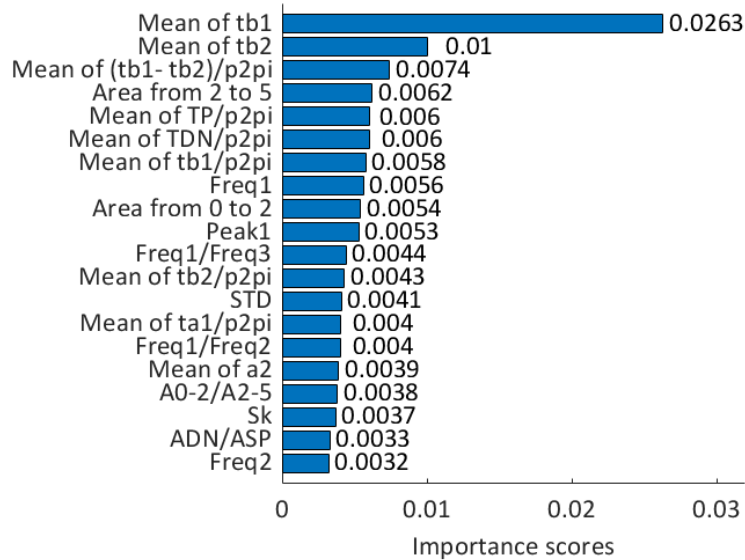
CHAPTER 3

used: RReliefF, MRMR, and CFS. These methods assign an importance score to each feature, allowing the selection of the most significant features. By applying these methods to \mathfrak{F}_S and \mathfrak{F}_E , for both *SBP* and *DBP*, 12 reduced sets are obtained: $\mathcal{R}_{i,j,k}$, where: $i = SBP, DBP$ for systolic and diastolic pressure, respectively; $j = S, E$ for the full standard or full expanded set of features, respectively; and $k = RReliefF, MRMR, CFS$. The number of features to consider in each set is somewhat arbitrary, but to ensure a fair comparison, it must remain consistent when the set is used to estimate the same type of pressure, whether *SBP* or *DBP*. Hence set cardinalities are $M_{SBP} = |\mathcal{R}_{SBP,j,k}|$ and $M_{DBP} = |\mathcal{R}_{DBP,j,k}|$, for all j and k . $M_{SBP} = 20$ and $M_{DBP} = 25$ have been chosen by considering, as a reference, the score assigned by the RReliefF algorithm. The threshold for significance has been set at 0.001, below which features are discarded. This is because they are deemed not significant and uncorrelated to the output. Two ML models were trained and evaluated on each reduced set of features, $\mathcal{R}_{i,j,k}$, to appreciate the effects of signal enhancement and of features selection methods. The two ML models used here are XGBoost and NN.

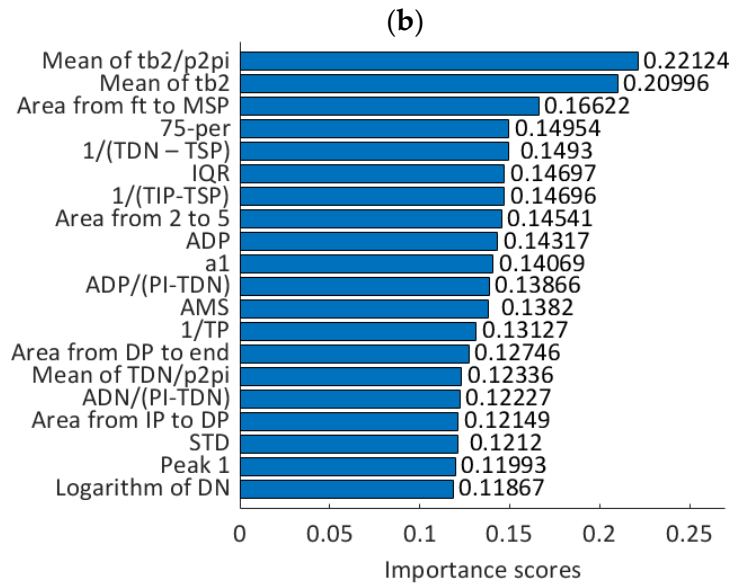
In order to gain a deeper insight into the rationale behind this particular section, it is essential to recall the features that have been taken into consideration in this Chapter, that compose \mathfrak{F}_S and \mathfrak{F}_E , that have already been described in the **Table A1** of the **Appendix A**. Moreover, in **Chapter 1** the importance scores of the best features of the expanded set, $\mathcal{R}_{i,E,k}$, are calculated and reported. These findings indicate that a considerable number of the newly introduced features of \mathfrak{F}_E exhibit higher scores than those belonging to \mathfrak{F}_S alone, suggesting the potential for training more accurate ML models. However, due to computational constraints, the actual performance of XGBoost and NN models has been evaluated exclusively within the specified case $\mathcal{R}_{i,E,MRMR}$ and reported in **Chapter 2**. It remains uncertain whether an alternative selection method, aside from the MRMR approach, could potentially yield enhanced ML outcomes. Furthermore,

CHAPTER 3

the potential influence of MODWT enhancement on ML performance remains unclear. Hence, in addition to feature sets $\mathcal{R}_{i,E,k}$ already enumerated in **Chapter 1**, in the present Chapter it necessary to consider also the sets $\mathcal{R}_{i,S,k}$, which are enumerated in **Fig. 25** and in **Fig. 26**.

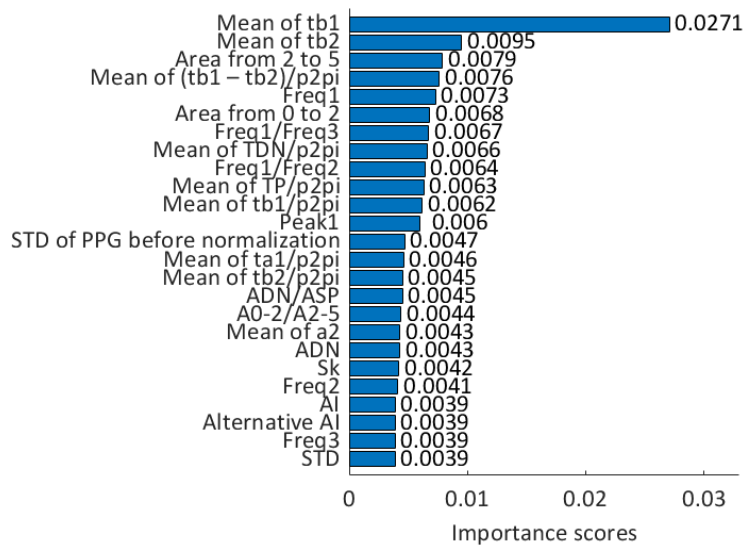


CHAPTER 3



(c)

Fig. 25. Significant features for *SBP* using three selection algorithms: RReliefF (a), MRMR (b), CFS (c).



CHAPTER 3

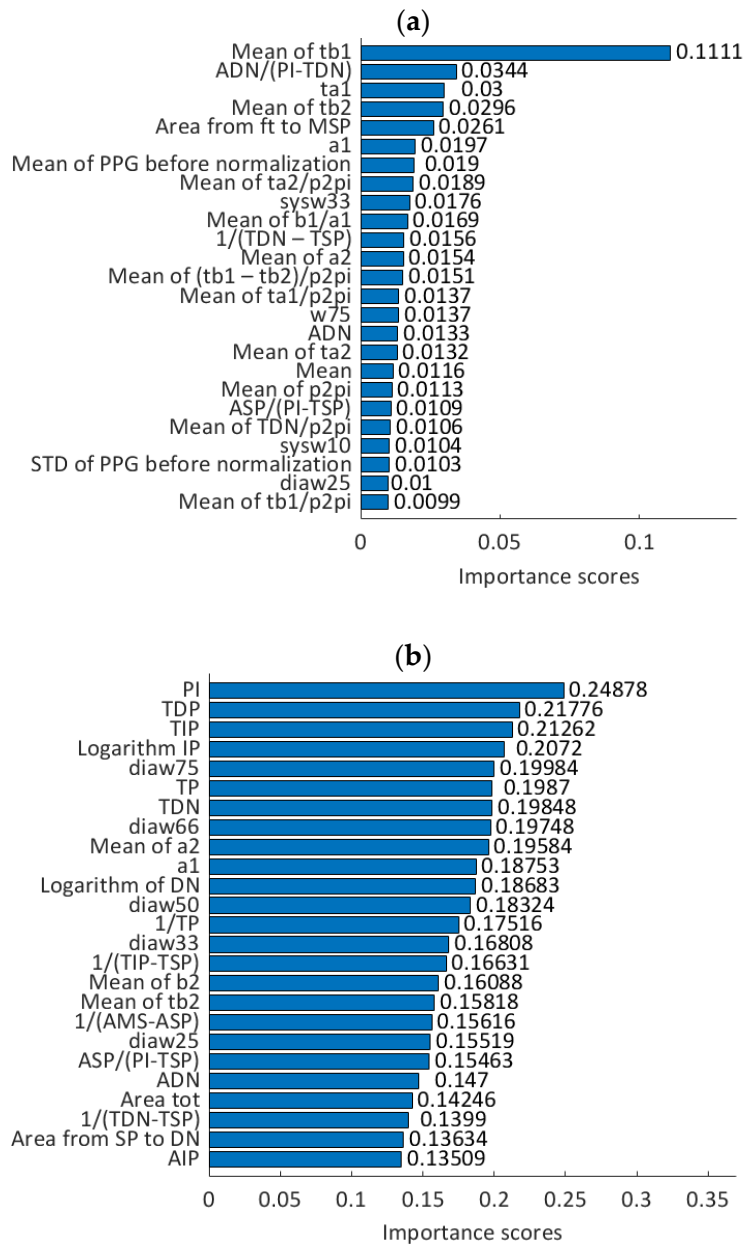


Fig. 26. Significant features for *DBP* using three selection algorithms: RReliefF (a), MRMR (b), CFS (c).

In order to ensure consistency with the methodology outlined in **Chapter 2**, the training of both XGBoost and NN models has been conducted using Python 3.9.9. For purposes of completeness, the hyperparameters of the XGBoost models are presented again here. For *SBP*, the hyper-parameters are as follows: the learning rate was set to 0.226, the maximum tree depth to 15, the subsample to 0.894, the

CHAPTER 3

subsample ratio of columns by tree to 1.0, lambda to 120.0, alpha to 1×10^{-10} , and the estimators to 5000. The hyper-parameters for *DBP* are as follows: the learning rate was set to 0.136, the maximum tree depth to 15, the subsample to 0.894, the subsample ratio of columns by tree to 1.0, the lambda to 120.0, the alpha to 1×10^{-10} , and the estimators to 5200. In contrast, NN models are sequential models comprising an input layer of size 20 for *SBP* and 25 for *DBP*, nine hidden layers, and an output layer. All neurons employ the ReLU activation function. The computations were performed on a NVIDIA GeForce RTX 3060 12 GB GPU. In **Table 12 - Table 15** the results obtained by ML models are reported. The criteria used to evaluate the performance of the ML models for estimating BP are RMSE

$$RMSE = \sqrt{\frac{1}{K} \sum_{n=1}^K (\widehat{BP}_n - BP_n)^2}, \quad (5)$$

and MAE

$$MAE = \frac{1}{K} \sum_{n=1}^K |\widehat{BP}_n - BP_n|, \quad (6)$$

where \widehat{BP}_n and BP_n are the n -th predicted and true BP (systolic or diastolic), respectively, and K in the number of observations used in the validation dataset. The results for XGBoost are presented in **Table 12** and **Table 13**, with the RMSE and MAE values obtained after 10-fold cross-validation. The training and cross-validation were conducted using 9×10^6 observations, with the 90% comprising the training set and the remaining 10% constituting the validation set. The results for the NN are presented in **Table 14** and **Table 15**, with the RMSE and MAE values for the validation set at the conclusion of the training period.

In light of these findings, it is evident that XGBoost models exhibit superior RMSE and MAE compared to NN models. This finding aligns with the conclusions of **Chapter 2**, which focused exclusively on $\mathcal{R}_{i,E,MRMR}$, but it builds

CHAPTER 3

upon that study by examining all three selection algorithms for both systolic and diastolic pressures, with and without MODWT enhancement. The combination of the XGBoost model, MODWT enhancement of the PPG signal, and a selection performed by RReliefF or MRMR yielded the most optimal results. The RMSE was better for MRMR, while the MAE was better with RReliefF. It is also noteworthy that the enhanced results are obtained using RReliefF and MRMR, which include MODWT enhancement. Conversely, CFS, which is the least effective method in this experimental setup, produces the poorest outcomes.

Table 12. Systolic pressure measurement performance using XGBoost model.

Systolic case	RMSE (mmHg)	MAE (mmHg)
RReliefF features reported in Chapter 1	5.77	2.77
RReliefF features in literature	6.93	3.32
MRMR features reported in Chapter 1	5.60	3.11
MRMR features in literature	5.89	3.25
CFS features reported in Chapter 1	6.77	3.59
CFS features in literature	6.60	3.49

Table 13. Diastolic pressure measurement performance using XGBoost model.

Diastolic case	RMSE (mmHg)	MAE (mmHg)
RReliefF features reported in Chapter 1	4.04	2.08
RReliefF features in literature	4.34	2.29
MRMR features reported in Chapter 1	3.92	2.09
MRMR features in literature	4.01	2.15
CFS features reported in Chapter 1	5.51	3.39
CFS features in literature	4.58	2.58

CHAPTER 3

Table 14. Systolic pressure measurement performance using NN model.

Systolic case	RMSE (mmHg)	MAE (mmHg)
RReliefF features reported in Chapter 1	7.05	4.47
RReliefF features in literature	7.31	4.43
MRMR features reported in Chapter 1	7.80	5.00
MRMR features in literature	7.81	5.02
CFS features reported in Chapter 1	8.96	5.69
CFS features in literature	8.90	5.62

Table 15. Diastolic pressure measurement performance using NN model.

Diastolic case	RMSE (mmHg)	MAE (mmHg)
RReliefF features reported in Chapter 1	4.98	2.93
RReliefF features in literature	5.13	3.10
MRMR features reported in Chapter 1	5.53	3.51
MRMR features in literature	5.57	3.52
CFS features reported in Chapter 1	7.26	5.01
CFS features in literature	6.80	4.53

3.3 EFFECTS OF ML ALGORITHMS AND DATASET SIZES ON RMSE AND TRAINING TIME

In this section, the Regression Learner App of MATLAB R2022a was employed to train seven additional families of algorithms, encompassing numerous potential variations, for a total of 34 models overall. The 10-fold cross-validation method was utilized for this purpose. However, it was necessary to reduce the

CHAPTER 3

size of the dataset due to the considerable amount of computing time required for training. Accordingly, a reduced dataset created by random extraction, comprising 10,000 observations has been employed for all algorithms, thereby facilitating a comparative analysis of the resulting outcomes. The actual training durations of each model are presented in **Table 16**, along with the RMSE performance metrics. The feature set utilized for training is $\mathcal{R}_{i,E,RReliefF}$ and $\mathcal{R}_{i,E,MRMR}$, which are derived from the MRMR and RReliefF algorithms and include the novel features extracted from the MODWT enhanced PPG signal. As evidenced in the preceding section, these feature sets yielded the most optimal outcomes.

Table 16 presents the RMSE of *SBP* and *DBP* and the training times of all ML algorithms for the two feature selection methods. The XGBoost and NN models have been included once more, but they have been trained using the reduced dataset. XGBoost and NN were trained in Python, while the remaining algorithms were trained in MATLAB using the Regression Learner App, as previously stated.

Table 16. Performance comparison of ML models and features sets for systolic (a) and diastolic (b) pressure measurement.

(a)			
Model	SBP		
	RMSE RReliefF (mmHg)	RMSE MRMR (mmHg)	Time (s)
Optimizable GPR	12.23	12.37	1.9561×10^5
XGBoost	13.21	13.51	991.00
Optimizable Ensemble (Bayesian optimization)	13.25	13.74	241.86

CHAPTER 3

Rational Quadratic GPR	13.28	14.43	275.57
Exponential GPR	13.29	14.42	194.37
Matern 5/2 GPR	13.39	14.50	150.75
Bagged Ensemble	13.57	13.96	6.60
Squared Exponential GPR	13.59	14.49	132.34
Fine Gaussian SVM	13.94	15.55	20.83
Optimizable SVM (Bayesian optimization)	13.95	16.44	1787.00
Optimizable NN (Bayesian optimization)	14.65	15.74	3224.8
Medium gaussian SVM	14.98	15.54	14.98
Least Squares Regression Kernel	15.25	15.52	21.46
Medium NN	15.26	15.83	51.06
Trilayered NN	15.38	15.73	34.29
Bilayered NN	15.39	15.63	26.67
NN	15.47	15.45	67.20
Optimizable Tree (Bayesian optimization)	15.51	15.92	23.83
Coarse Tree	15.52	16.02	1.30
SVM Kernel	15.65	16.11	51.36
Narrow NN	15.66	15.98	19.34
Boosted Ensemble	15.82	15.98	4.59
Wide NN	15.92	17.32	156.53
Medium Tree	16.17	16.62	1.31
Stepwise Linear	16.54	16.86	4112.7
Quadratic SVM	16.56	16.97	30.98
Interactions Linear	16.72	17.00	3.82
Coarse gaussian SVM	16.75	16.87	14.69
Robust Pure Quadratic Linear	16.84	17.04	4.74
Linear	17.00	17.03	1.14

CHAPTER 3

Robust Linear	17.01	17.03	1.73
Linear SVM	17.04	17.09	14.63
Robust Interactions Linear	17.36	18.24	51.47
Robust Quadratic Linear	17.38	17.71	62.63
Fine Tree	17.43	18.00	2.36
Cubic SVM	19.63	20.32	165.32

(b)

Model	DBP		
	RMSE RReliefF (mmHg)	RMSE MRMR (mmHg)	Time (s)
Optimizable GPR	7.47	7.52	1.4333x10 ⁵
Optimizable Ensemble (Bayesian optimization)	7.85	8.18	688.12
XGBoost	7.89	7.95	1339.00
Matern 5/2 GPR	7.90	8.37	154.03
Exponential GPR	7.90	8.28	157.59
Rational Quadratic GPR	7.91	8.33	268.85
Squared Exponential GPR	7.94	8.43	147.43
Bagged Ensemble	8.03	8.21	7.70
Fine Gaussian SVM	8.13	8.65	19.38
Optimizable NN (Bayesian optimization)	8.49	8.83	5038.00
Medium gaussian SVM	8.64	8.97	14.70
Boosted Ensemble	8.69	8.82	5.77
Bilayered NN	8.71	8.97	29.70
Least Squares Regression Kernel	8.72	8.91	18.96
Medium NN	8.74	9.13	52.24
Narrow NN	8.79	9.00	22.52

CHAPTER 3

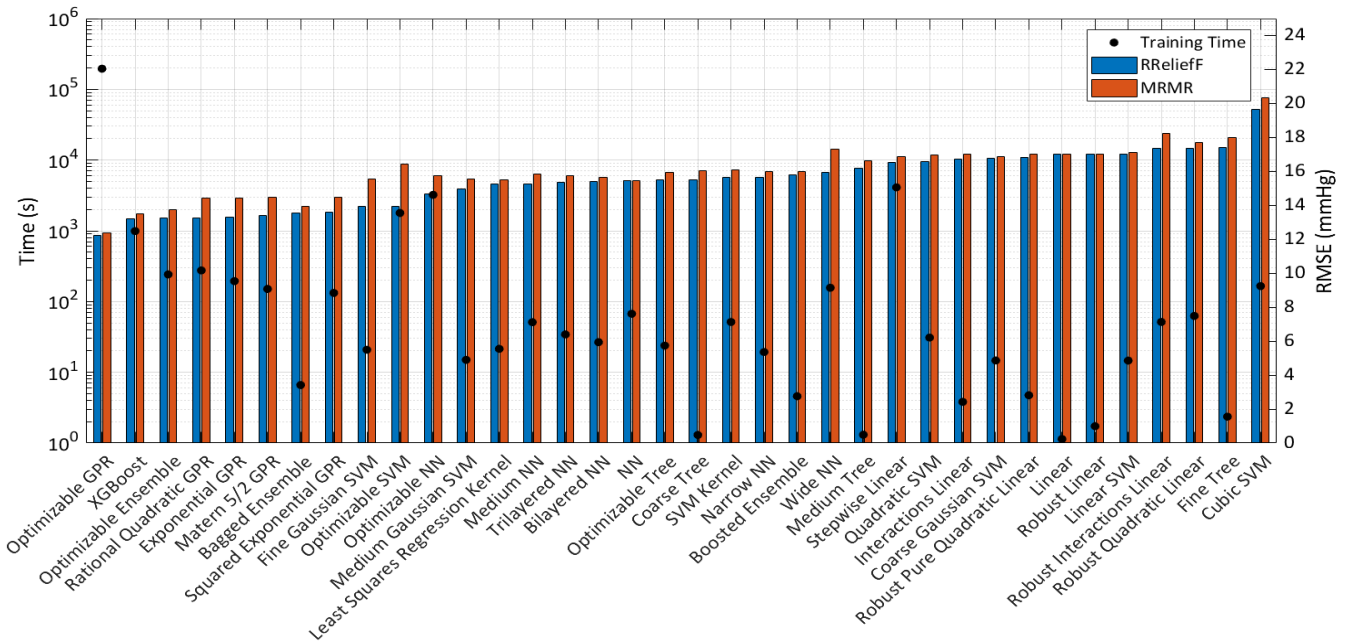
Coarse Tree	8.84	9.24	1.37
Optimizable Tree (Bayesian optimization)	8.85	9.09	26.13
NN	8.87	8.74	72.00
Trilayered NN	8.87	9.15	35.66
SVM Kernel	9.01	9.34	50.79
Medium Tree	9.29	9.61	1.35
Linear	9.30	9.36	1.32
Stepwise linear	9.36	9.49	15059
Robust Linear	9.42	9.48	2.90
Coarse Gaussian SVM	9.52	9.59	13.76
Wide NN	9.56	10.62	159.69
Robust Quadratic Linear	9.58	10.82	162.58
Optimizable SVM (Bayesian optimization)	9.59	9.59	3327.1
Linear SVM	9.62	9.71	14.24
Robust Pure Quadratic Linear	9.63	9.47	4.38
Interactions Linear	9.98	10.31	7.41
Quadratic SVM	10.01	10.29	27.43
Robust Interactions Linear	10.12	10.92	141.25
Fine Tree	10.16	10.55	4.10
Cubic SVM	28.22	26.70	129.68

Furthermore, **Fig. 27** depicts the identical results, arranged in accordance with the RMSE obtained through the RReliefF selection. It is evident that the training times exhibit a considerable degree of variation; thus, a logarithmic scale has been employed for illustrative purposes. It is important to note that the lower RMSE models have higher training times, yet there is no straightforward correlation between RMSE and training time. As can be observed in **Table 16**, the

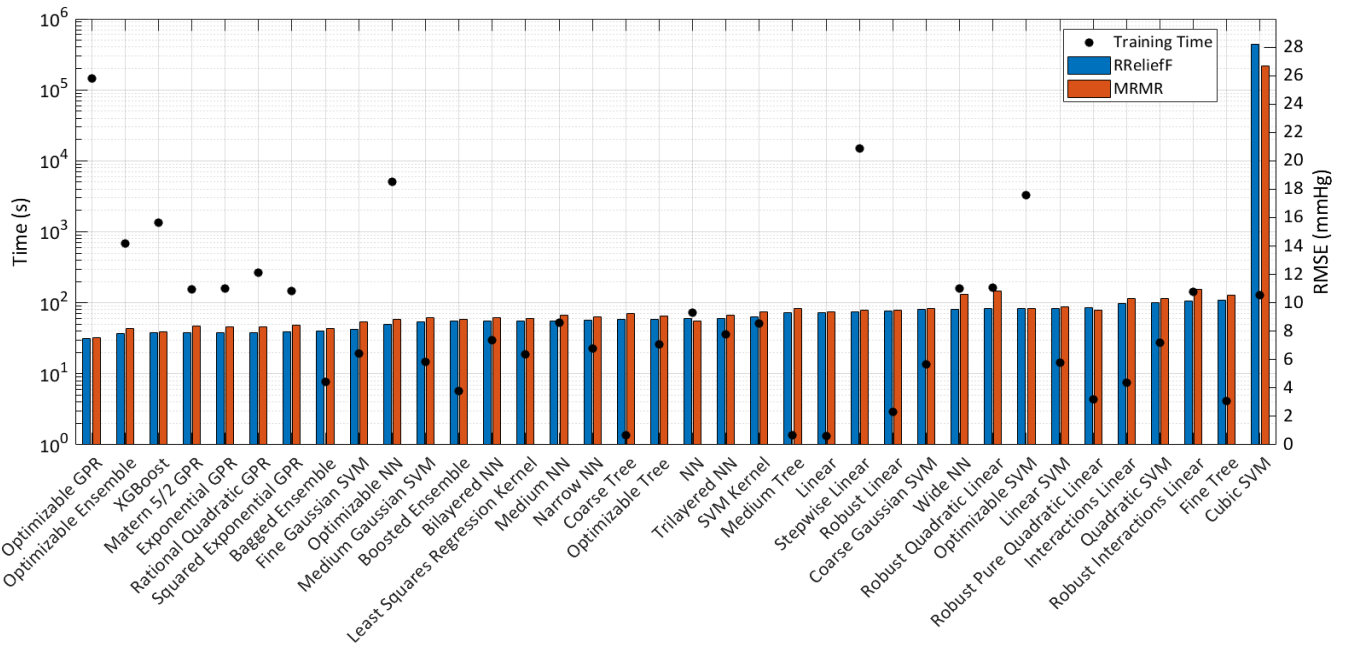
CHAPTER 3

RMSE values obtained with RReliefF are, in general, superior to those obtained with MRMR, with the exception of the NN model for both *SBP* (a) and *DBP* (b). This finding corroborates the results previously reported in **Table 14** and **Table 15**. In contrast, for two additional high RMSE models, namely Robust Pure Quadratic Linear and Cubic SVM, MRMR is observed to outperform RReliefF for *DBP*. In general, the use of Optimizable GPR, XGBoost, and Optimizable Ensemble resulted in superior RMSE outcomes. Among the models, XGBoost and the Optimizable Ensemble appear to offer the optimal balance, reducing training time significantly while maintaining low RMSE.

CHAPTER 3



(a)



(b)

Fig. 27. RMSE results for systolic pressure (a) and for diastolic pressure (b) using the reduced dataset and two different selection methods namely MRMR and RReliefF. The training time is reported in the logarithmic scale.

CHAPTER 3

The results are further illustrated in **Fig. 28**, where the models on the Pareto front are explicitly labeled. It is noteworthy that the Ensemble and GPR models appear on the Pareto front on two occasions (and frequently among the best RMSE scores). This is observed both as specific models (i.e., Bagged Ensemble and Exponential GPR) and as optimizable models with reduced RMSE but increased training times due to method/kernel and hyperparameters optimization.

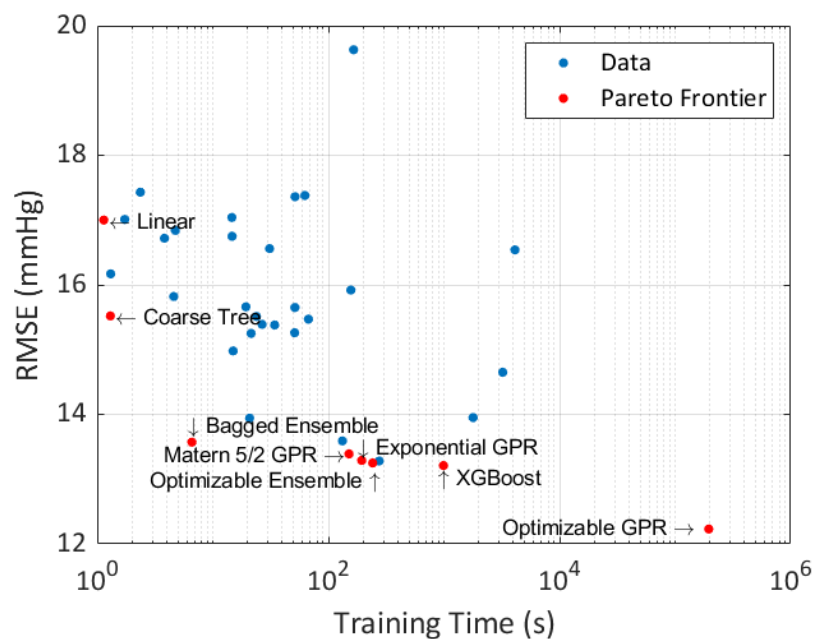


Fig. 28. Training time and RMSE for *SBP* measurement, with indication of the Pareto front.

Following the training phase, the Optimizable Ensemble has selected the Bag method, whereas the Optimizable GPR has chosen the Nonisotropic Rational Quadratic kernel.

A comparison of **Table 12** through **Table 15** reveals that the reduction in the dataset has resulted in an increase in the RMSE for both the XGBoost and the NN models. In some cases, the RMSE has doubled, indicating a dependence of performance on the dataset size. To further investigate this phenomenon, a study was conducted in which the dimension of the dataset varied for four models that

CHAPTER 3

demonstrated high performance. The dataset ranged from 1,000 observations to 100,000 observations, and the results are presented in **Fig. 29**. The four selected models are XGBoost, Optimizable Ensemble, and Exponential GPR, which demonstrate a lower *SBP* RMSE on the Pareto front, and Optimizable Tree, which exhibits a median RMSE. Among the optimal models, the Optimizable GPR was not considered due to the extensive training time required. However, it can be reasonably assumed that its behavior is similar to that of other models. This study was conducted exclusively for *SBP* measurement, utilizing the $\mathcal{R}_{SBP,E,MRMR}$ set, as superior RMSE outcomes were previously attained (for 9×10^6 observations) when MODWT enhancement and MRMR were employed. **Fig. 29** illustrates that an increase in the size of the dataset is associated with an improvement in performance. However, the rate of improvement is sublinear, as evidenced by the logarithmic scale used for the x-axis. These considerations are also supported by the literature [104]. As a matter of fact, the performance of the four models is more similar when the dataset is reduced in size, while the difference between them increases when the dataset is larger.

Furthermore, a more comprehensive statistical analysis has been conducted for the previously selected optimal models, Bagged Ensemble and Optimizable Tree

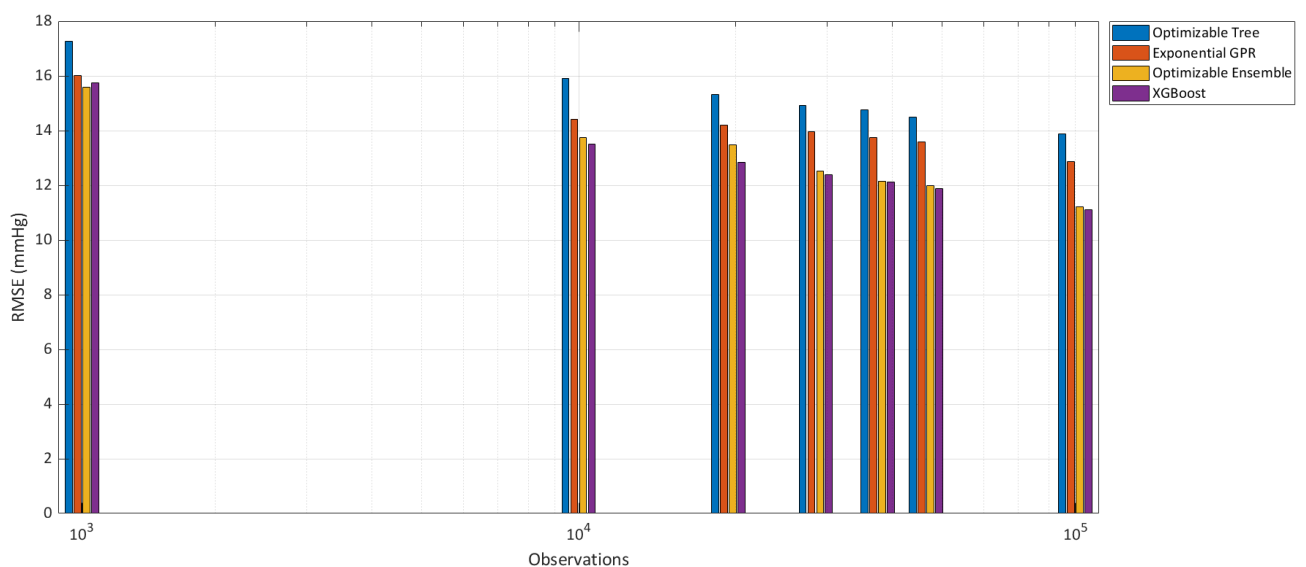


Fig. 29. RMSE of *SBP* measurement, varying the dimension of the training dataset.

CHAPTER 3

(which has a median *SBP* RMSE), in order to more accurately assess the significance of the obtained results, as illustrated in **Table 17**. The Bagged Ensemble was included in this further analysis because it is the method selected at the conclusion of the Optimizable Ensemble training. Consequently, by directly considering this model, it is possible to significantly reduce the training time while achieving optimal results. The table presents the mean RMSE obtained from the 10-fold cross-validation, the STD of the mean RMSE, and the 95% confidence interval (CI) of the mean RMSE. With regard to *SBP* estimation, it can be observed that XGBoost and Bagged Ensemble, which exhibit a smaller STD of RMSE, yield more consistent results across the repetitions of the 10-fold cross-validation. Referring to the measurement of *DBP*, the STD of the mean RMSE for the various methods is comparable, with the exception of XGBoost applied to RReliefF selected features, which exhibits a lower value. The results of the ANOVA indicate that there is a statistically significant difference between the methods under consideration (p-values 0.0006 for *SBP* RReliefF, 2×10^{-5} for *SBP* MRMR, 0.04 for *DBP* RReliefF, 0.007 for *DBP* MRMR). In particular, pairwise comparisons were performed using Tukey's HSD tests, which revealed significant differences between Optimizable Tree and the other methods. In the comparisons regarding Optimizable Tree, higher p-values were observed, specifically 0.01 for *SBP* RReliefF, 0.01 for *SBP* MRMR, 0.18 for *DBP* RReliefF, and 0.08 for *DBP* MRMR. Therefore, the discrepancies with regard to the Optimizable Tree are more pronounced in the estimation of *SBP*, while they are less pronounced in the estimation of *DBP* and in the selection of RReliefF features. As the RMSE of XGBoost, Optimizable Ensemble, Exponential GPR, and Bagged Ensemble are comparable, the selection between them can be based on the training time, which is shorter for Bagged Ensemble.

CHAPTER 3

Table 17. Statistical analysis of the best models for systolic pressure (a) and for diastolic pressure (b).

(a)

Model	SYS					
	RReliefF			MRMR		
	Mean RMSE (mmHg)	STD RMSE (mmHg)	CI 95%	Mean RMSE (mmHg)	STD RMSE (mmHg)	CI 95%
XGBoost	13.21	0.29	12.64-13.78	13.51	0.18	13.16-13.86
Optimizable Ensemble	13.25	0.40	12.47-14.03	13.74	0.45	12.86-14.62
Exponential GPR	13.29	0.54	12.23-14.35	14.42	0.39	13.66-15.18
Bagged Ensemble	13.57	0.28	13.29-14.12	13.96	0.23	13.51-14.41
Optimizable Tree	15.51	0.44	14.65-16.37	15.92	0.26	15.41-16.43

(b)

Model	DIA					
	RReliefF			MRMR		
	Mean RMSE (mmHg)	STD RMSE (mmHg)	CI 95%	Mean RMSE (mmHg)	STD RMSE (mmHg)	CI 95%
XGBoost	7.89	0.065	7.76-8.02	7.95	0.13	7.70-8.20
Optimizable Ensemble	7.85	0.30	7.26-8.44	8.18	0.15	7.89-8.47
Exponential GPR	7.90	0.26	7.39-8.41	8.28	0.34	7.61-8.95
Bagged Ensemble	8.03	0.31	7.42-8.64	8.21	0.22	7.78-8.64
Optimizable Tree	8.85	0.27	8.32-9.38	9.09	0.17	8.76-9.42

3.4 DISCUSSION

This section provides a concise overview of the findings presented in the

CHAPTER 3

preceding sections. In light of the aforementioned findings, the following observations can be made.

The larger dataset of 9×10^6 observations, considered with both XGBoost and NN models (see **Table 12** - **Table 15**), yielded the best results for both systolic and diastolic pressures when the features were selected using MRMR and RReliefF, in comparison with CFS.

Furthermore, the most significant finding is that the outcomes achieved through the utilization of RReliefF and MRMR selections, which encompass the extracted features following the proposed MODWT enhancement as detailed in **Chapter 1**, demonstrate superior performance compared to those obtained through the exclusive reliance on features documented in the existing literature without the incorporation of MODWT. For instance, systolic RMSE is reduced from 5.89 mmHg to 5.60 mmHg when MRMR is employed, and from 6.93 mmHg to 5.77 mmHg when RReliefF is utilized. These results are applicable to XGBoost and NN models, and analogous outcomes are observed in the diastolic case and for MAE. However, it should be noted that the CFS selection method, which exhibits inferior performance with respect to RReliefF and MRMR, does not benefit from the MODWT enhancement.

A comparison of numerous ML models with a reduced dataset of 10,000 observations, as illustrated in **Table 16** and **Fig. 27**, reveals that the Optimizable GPR models yield superior results. However, the training process for both systolic and diastolic pressures has been time-consuming, requiring days for completion. It is important to note that the training of XGBoost models required approximately half an hour. However, the results in terms of RMSE differed by only 1.32 mmHg systolic and 0.43 mmHg diastolic with respect to the Optimizable GPR model using MRMR selected features. Furthermore, the difference in RMSE between the XGBoost and Optimizable GPR models was only 0.98 mmHg systolic and 0.42 mmHg diastolic using RReliefF selected features. In

CHAPTER 3

comparison, for the systolic pressure, the Optimizable GPR reduced the RMSE by 7% in comparison to XGBoost RMSE but increased the training time by 197 times. For the diastolic pressure, the RMSE was reduced by 5%, but the training time was increased by 107 times. Similar considerations apply to Ensemble (Bagged and Optimizable) and Exponential GPR methods. Therefore, these models may be deemed an appropriate option for the estimation of BP.

The use of MODWT enhancement allows to emphasize characteristic points of the PPG signal, including the diastolic point, which leads to excellent results in BP estimation. **Fig. 29** illustrates an intriguing relationship between the dataset size and the RMSE values. Indeed, the RMSE decreases as the number of observations in the training dataset increases. This results in the XGBoost model producing the values shown in **Table 12** and illustrated in **Fig. 30**, which depict the RMSE values for varying sizes (N) of the training dataset. A straightforward model can be formulated as follows:

$$RMSE = a \times \log_{10}(N) + b, \quad (7)$$

obtaining the least squares estimates $a = -2.6$ mmHg, $b = 24.1$ mmHg. This relation can be extrapolated up to $N = 1.5 \times 10^9$, where it is no longer significant, with an $RMSE = 0$ mmHg. As **Fig. 29** shows, the other models will exhibit a similar behavior. The RMSE of Optimizable Tree and Optimizable Ensemble will improve with N , similarly to XGBoost. Meanwhile, Exponential GPR will improve slowly. It is important to note that Optimizable models will benefit from tuning their hyperparameters when N changes.

CHAPTER 3

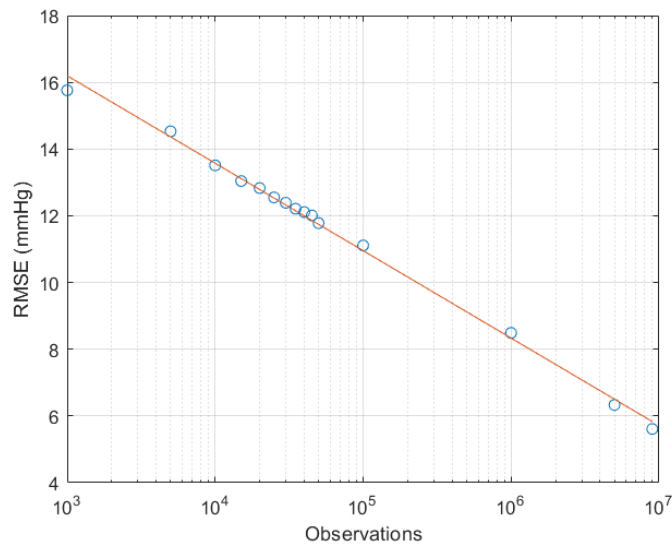


Fig. 30. Fitting of RMSE for SBP measurement varying the number of observations using XGBoost models.

It would be beneficial to investigate whether the RReliefF or MRMR feature selection methods result in superior outcomes. In a previous study [19], it was reported that the best RMSE and MAE were obtained using features selected by the RReliefF algorithm. This finding aligns with the results of this Chapter when considering **Table 16**. When the models are trained on a reduced dataset, features selected by RReliefF provide better RMSE regardless of the model chosen (including XGBoost), except for NN and Cubic SVM. In contrast, when the models were trained on the larger dataset of 9×10^6 observations, MRMR yielded marginally superior RMSE results for the XGBoost model, while RReliefF demonstrated superior performance for the NN model. Indeed, the systolic RMSE using the MRMR method is reduced by 0.17 mmHg for XGBoost models and increased by 0.75 mmHg for NN models when compared with the RReliefF method. A similar comparison of the MRMR diastolic RMSE reveals a decrease of 0.12 mmHg for XGBoost models and an increase of 0.58 mmHg for NN models with respect to RReliefF. Overall, the MRMR method has demonstrated the greatest efficacy in this study for the XGBoost model. It is therefore important to

CHAPTER 3

note that the relative performance of RReliefF and MRMR is dependent on the size of the training set and the ML model selected. Furthermore, for a high-performance model such as XGBoost, the features selected by MRMR resulted in a smaller RMSE for larger datasets.

Furthermore, another area that is not addressed during training and has not been examined in this study is individual calibration. However, the performance reported in this section already accounts for variability associated with individual differences. Indeed, further enhancement of the results may be accomplished through the implementation of individual calibration or TL methodologies, thereby ensuring the predictions are tailored to the specific subject. This challenging aspect is currently the subject of investigation by numerous researchers [105], [106], [107].

A more comprehensive comparison is presented in **Table 18**, as it was essential to evaluate a range of ML models and feature selection techniques. In numerous published works, a restricted number of features are extracted without the utilization of a feature selection method. In other works, the most used methods are principal component analysis (PCA), RReliefF, Pearson's correlation coefficients (PCC), and the maximum information coefficient (MIC). It should be noted that the table does not present all the analyses conducted in the cited works; rather, it shows only those that demonstrated optimal performance. Indeed, in some of these papers, the efficacy of multiple feature selection and ML methods has been evaluated. It is also noteworthy that the selected ML models are predominantly SVM for regression and models from the boosting framework. The results reported in the various papers are inferior to those obtained in this study. This discrepancy may be attributed to the absence of a methodology for selecting features and the disparate features employed. As evidenced by the table, the work of Chowdhury et al. [19] has yielded marginally superior outcomes (except for *SBP* RMSE). However, direct comparison of these results

CHAPTER 3

with those in this Chapter is not feasible, as the datasets differ, and the features selected by RReliefF include those demographics that were not employed in this study. The aforementioned features were not accessible in the version of the dataset utilized, which is more recent and larger.

Table 18. Comparison of several ML models and features selection methods.

Work	Method	Data Size	Features selection	Performance Evaluation	SBP (mmHg)	DBP (mmHg)
Kachuee et al. [18]	SVM	MIMIC II (1000 subjects)	Without selection	RMSE	/	/
				MAE	12.38	6.34
Kim et al. [66]	NN	180 recordings, 45 subjects	PCA	RMSE	/	/
				MAE	4.53	/
Cattivelli et al. [67]	Proprietary algorithm	MIMIC database (34 recordings, 25 subjects)	Only PAT peaks	RMSE	8.37	5.92
				MAE	/	/
Zhang et al. [68]	SVM	7000 samples from 32 patients	Without selection	RMSE	/	/
				MAE	11.64	7.62
Zadi et al. [69]	ARMA models	15 subjects	Without selection	RMSE	6.49	4.33
				MAE	/	/
Chowdhury et al. [19]	GPR	222 recordings, 126 subjects	RReliefF	RMSE	6.74	3.59
				MAE	3.02	1.74
Hasanzadeh et al. [21]	AdaBoost	MIMIC II 942 subjects	Without selection	RMSE	/	/
				MAE	8.22	4.17
Kachuee et al. [54]	AdaBoost	942 subjects	PCA	RMSE	/	/
				MAE	11.17	5.35
Wang et al. [70]	NN	58,795 PPG samples	Without selection	RMSE	/	/
				MAE	4.02	2.27
Kurylyak et al. [23]	NN	15,000 PPG heartbeats	Without selection	RMSE	/	/
				MAE	3.80	2.21
	XGBoost			RMSE	/	/

CHAPTER 3

Fleischhauer et al. [71]		MIMIC, Queensland, PPG BP (273 subjects and 259,986 single beats)	Without selection	MAE	6.37	/
Liu et al. [72]	SVM	MIMIC II 910 good PPG pulses cycles	Without selection	RMSE	/	/
				MAE	8.54	4.34
Zhang et al. [73]	GBR	MIMIC II 2842 samples from 12,000 data points	Without selection	RMSE	/	/
				MAE	4.33	2.54
Dey et al. [108]	LASSO regression	Own dataset (205 subjects)	Without selection	RMSE	/	/
				MAE	6.90	5.00
Mousavi et al. [79]	Adaboost R	MIMIC-II (441 subjects)	PCA	RMSE	/	/
				MAE	3.97	2.43
Duan et al. [109]	SVM	The University of Queensland Vital Signs Dataset (32 cases, 7678 samples)	PCC and MIC	RMSE	/	/
				MAE	4.77	3.67
Chowdhury et al. [94]	LR	PPG-BP (153 subjects)	Without selection	RMSE	/	/
				MAE	4.75	3.34
Proposed method	XGBoost	MIMIC III 9.1×10^6 PPG pulses from 1080 subjects	MRMR	RMSE	5.67	3.95
				MAE	3.12	2.11

3.5 CONCLUSION

Following the proposal of a features set and a ML model, this Chapter presents a more comprehensive analysis and performance comparison of different sets of significant features and ML algorithms. The primary objective has been to examine the potential of ML models for estimating BP using features extracted from the PPG signal. This approach offers a non-invasive alternative to traditional cuff-based BP monitoring, facilitating continuous and uninterrupted monitoring, which is a crucial aspect in telemedicine applications.

It has been demonstrated that the enhancement of the PPG signal by using MODWT leads to the training of ML models that demonstrate improved performance in estimating BP. Nevertheless, the scope of interest has not been confined to this particular aspect but has also encompassed a comparison of disparate sets of features that have been selected by three distinct algorithms. This comparison has revealed that both MRMR and RReliefF outperform CFS. Finally, multiple ML models were trained using varying dataset sizes to provide an overview of these algorithms within this research area, demonstrating the trade-off between prediction performance and training time. The combination of XGBoost, Ensemble, and Exponential GPR models with MODWT enhancement of the PPG signal demonstrated a favorable trade-off between training time and RMSE and MAE. In comparison, other models, such as Optimizable GPR, demonstrated a reduction in RMSE by 7% but an increase in training time by a factor of 197 relative to XGBoost.

The results presented here indicate that it is feasible to develop a portable device capable of acquiring PPG signals and implementing a BP estimator. The development of ML models that take into account the selection of features allows the realization of embedded systems. This is because the use of a reduced number of appropriately selected features ensures a lower computational cost, enabling

CHAPTER 3

onboard processing that allows savings in energy in battery-powered devices. Moreover, the examination of the performance of the disparate models enables the identification of an optimal balance between the model's complexity and its performance, thereby facilitating the determination of a less resource-intensive model that can effectively delineate the minimum requisite hardware specifications. Furthermore, an in-depth examination of the various feature selection methods and models, along with a comprehensive evaluation of their performance and the size of the dataset, is of paramount importance, particularly when dealing with limited data. The aforementioned analysis has a direct impact on the effectiveness and reliability of the resulting BP estimator. In light of these findings, the potential for monitoring BP using the PPG signal is becoming increasingly viable and suitable for monitoring patients' status in their homes, with the ultimate objective of enhancing their well-being.

ABP ESTIMATION THROUGH PPG SIGNAL ANALYSIS AND ADVANCED LOSS FUNCTION OPTIMIZATION

INTRODUCTION

Nowadays, PPG obtains increasing significant attention due to its potential for continuous estimation of BP. The application of ML and DL algorithms to PPG signals enables the analysis of these signals, thus facilitating the generation of accurate BP estimates [16], [17], [21], [22], [73], [78]. DL models, including convolutional neural networks (CNNs) and recurrent neural networks (RNNs), are perfect at processing intricate patterns within PPG waveforms, enabling the capture of subtle variations that are correlated with alterations in BP.

As a matter of fact, these models are trained on extensive datasets to enhance their accuracy and reliability. The combination of PPG and DL represents a promising path for the development of non-invasive, real-time BP monitoring systems. Such systems have the potential to transform hypertension management and improve patient outcomes through the implementation of more personalized and timely interventions [107], [110], [111], [112], [113], [114], [115]. It is clear that these networks are used extensively in many different applications, leading to the development of models that produce excellent results, not just for BP estimation [116], [117], [118], [119].

CHAPTER 4

Nevertheless, the estimation of BP using PPG is not a straightforward process, as this signal is susceptible to noise, including motion artifacts and individual differences.

It is therefore crucial to consider the inter-subjectivity aspect when evaluating methods for BP estimation from PPG signals [120], [121]. Incorporating data from several individuals allows DL models to more effectively capture the variability in PPG waveforms across different physiological conditions and anatomical differences. However, inter-subjectivity presents a significant challenge for researchers. It is crucial to collect and annotate different datasets that adequately represent various demographics and health conditions, which is a resource-intensive process. This variability encompasses factors such as skin tone, age, and overall cardiovascular health, which significantly impact the relationship between PPG signals and BP levels. Training models on a broad range of subjects enhances their ability to generalize and adapt to new individuals, thereby improving the accuracy and reliability of BP predictions. This approach mitigates biases that might arise from training on a homogeneous dataset and ensures that the models can perform effectively across various demographic groups, ultimately leading to more robust and inclusive healthcare applications. However, it is essential to ensure that models do not overfit specific characteristics of the training data while still capturing meaningful inter-subject variability. To address these challenges, it is necessary to implement a rigorous pipeline or dataset processing, to develop innovative model architectures, and to implement effective validation strategies that account for the diverse populations under consideration. Once the necessity for an inter-subject approach has been established, it is imperative to explore another critical aspect of DL models. One of the main aspects affecting the performance of the models is the loss function, which plays an important role in the training phase of a DL model, serving as the primary metric for optimization [122], [123]. The loss function is used to compute

CHAPTER 4

the differences between the predicted outputs of the model and the actual target values. This provides a measure of the model's performance and can be used as a proxy for performance evaluation. During the training phase, the objective is to minimize the loss function, which indicates that the model is improving its predictions. The selection of an appropriate loss function is of paramount importance for both ML and DL models. It not only ensures that the model learns effectively but also influences the convergence speed and the overall performance. It is important for tasks such as classification, regression, and other forms of predictive modeling, as it directly affects the model's capacity to generalize from training data to unseen data, thereby ensuring robust and reliable predictions.

The most commonly used loss functions, such as MSE and MAE, are ineffective in DL due to the limitations imposed by the activation functions employed in the final layer. These limitations result in reduced efficiency and accuracy during training, underscoring the need for specialized loss functions tailored to the unique characteristics of DL. Accordingly, the development of loss functions designed to align with specific objectives has emerged as a pivotal and pressing challenge within this field. While there are studies in the literature that concentrate on loss functions [124], [125], further investigation is necessary to gain a more comprehensive understanding of the matter. In light of these considerations, the objective of this Chapter has been to develop an enhanced loss function that could potentially contribute to more precise and reliable predictions. The proposed method consists in weighting the systolic and diastolic points more than the other points of the ABP signal, thus addressing the inherent challenges and inaccuracies typically associated with converting PPG to ABP. The Chapter is centered on the utilization of the PPG signal to accurately derive the ABP signal in an inter-subject approach by using DL models. This approach is designed to be applicable across different individuals, thereby increasing the

CHAPTER 4

reliability of the method in diverse populations. It should be noted that this scenario comprises three distinct sets of patients: the training set, the validation set, and the test set. The inter-subject approach avoids concerns regarding the potential of data leakage when there are samples in training and test sets that share the same patient. The objective is to guarantee a performance evaluation that is both realistic and challenging by removing the availability of data from the same patient (even if they are different data) to the algorithms during this phase. Consequently, the algorithms were only able to access cross-subject BP variability during the testing phase. To achieve this objective, a variety of DL models were employed, leveraging their capacity to discern intricate patterns and relationships within the data. This advancement has the potential to markedly enhance non-invasive BP monitoring, providing a more efficacious and reliable methodology for medical diagnostics and continuous health monitoring through the implementation of a specific loss function.

4.1 DATASETS

In this Chapter two distinct datasets have been utilized to validate the results: the dataset processed by Kachuee et al. [18], [54] using MIMIC II [31] and the MIMIC III Waveform Database processed following the steps presented in **Chapter 1**. The two datasets are mutually exclusive and differ in the processing methodologies employed to obtain the final data. In summary, MIMIC-III represents a more advanced, comprehensive, and user-friendly dataset compared to MIMIC-II, with broader data coverage and improved accessibility, making it a preferred choice for most medical research applications. However, both datasets have been used to analyze the impact of a different processing methodology and also to deploy the same dataset used in other works.

CHAPTER 4

4.1.1 MIMIC-III DATASET

The MIMIC-III waveform dataset is an extensive, freely accessible database that serves as a critical resource for medical research. The database contains de-identified health data from over 40,000 patients who have received care in the ICU. This dataset integrates a multitude of data types, including demographic information, vital signs such as pulse oximetry, BP, ECG, and respiration signals, as well as some annotations, thereby facilitating comprehensive analyses in healthcare research. A total of 150 patients from the MIMIC-III database, for whom both PPG and ABP signals were available, were selected for download. Subsequently, the reduced dataset, subsequently designated as Dataset A, was subjected to the identical processing procedure described in **Chapter 1**: alignment between PPG signals and the ABP signals computing the cross-correlation function; denoising of PPG signals by applying a second-order Butterworth filter with pass-band 0.5 Hz to 8 Hz; Z-score standardization; baseline correction removing a fourth-order fitted polynomial; a tenth-order lowpass Yule-Walker recursive filtering with an 8 Hz cut-off frequency applied to the ABP; quality and similarity tests to eliminate inappropriate signals. A total of 120 patients, representing 80% of the total sample size, were randomly selected for the training phase. The remaining 10% were allocated to the validation phase, while the other remaining 10% were reserved for the test phase. The final dataset comprises PPG and ABP signals from 1,024 samples, corresponding to an 8.192 s segment. This dataset will be referred to as Dataset A1. The decision regarding the number of samples was made to facilitate the training of DL models by using a power of two as the number of samples for each PPG and ABP signal, as well as to align with existing literature on this topic.

It is also important to note that this study has considered a wide range of cases, each with varying signal durations. It should be noted that an alternative configuration comprises PPG and ABP signals of 1,024 samples, corresponding

CHAPTER 4

to a duration of 30 s. This will be referred to as Dataset A2. Moreover, two supplementary configurations utilize the input of PPG, the first derivative (PPG'), and the second derivative (PPG'') to train the DL models. This was implemented with the objective of aligning the methodology with existing literature, thereby facilitating a comparative analysis of the results obtained. Furthermore, this configuration allows for the identification of two distinct cases. In one instance, the duration of the segments is 30 s (Dataset A3), while in the other, it is 8.192 s (Dataset A4). In both cases, the number of samples is 1,024. The aforementioned cases are also illustrated in **Fig. 31**. The signal obtained as a result of the MODWT enhancement was not employed in this Chapter for the purpose of facilitating a comparison with existing literature. This was due to the fact that the objective was to conduct a detailed study on loss functions and on several DL models.

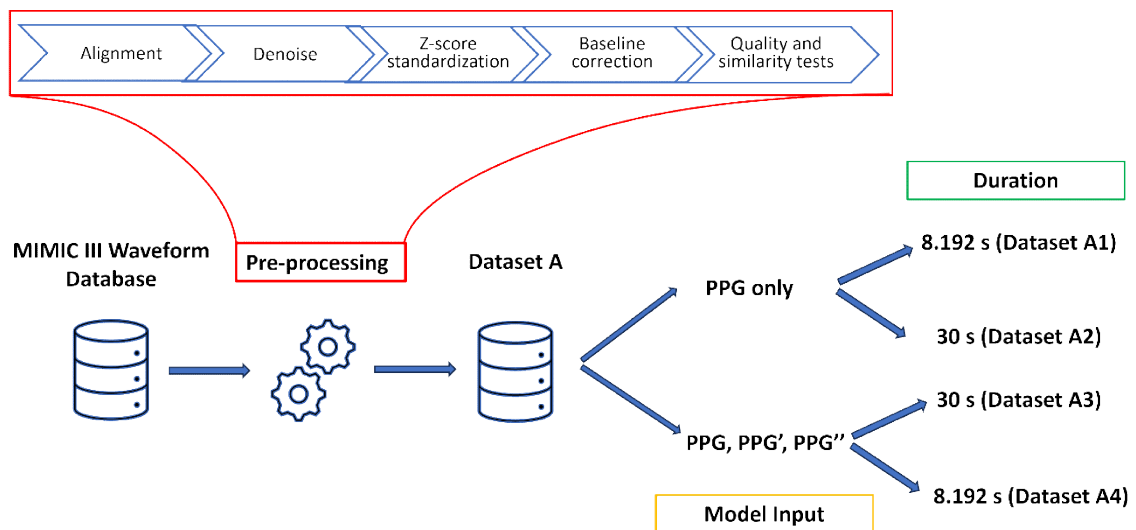


Fig. 31. Workflow of the processing for Dataset A.

4.1.2 MIMIC-II DATASET

The MIMIC II database encompasses a multitude of signals recorded by patient monitors at numerous hospitals between the years 2001 and 2008. The waveform signals were sampled at a frequency of 125 Hz with at least 8-bit accuracy.

CHAPTER 4

Kachuee et al. extracted PPG, ECG, and ABP waveform signals, which were then subjected to a series of key processing steps. These included the application of average filtering to smooth the signals, the removal of data blocks with unacceptable BP and HR values, and the elimination of those with persistent discontinuities despite smoothing. Additionally, the PPG autocorrelation function was computed to assess the similarity between consecutive pulses, and segments displaying significant alterations were also removed. The Kachuee's dataset has been downloaded from the UCI Machine Learning Repository [126], the dataset comprises 12,000 records of PPG, ECG, and ABP data from 942 patients. The processing code made by [114] has been used. The final dataset comprises segments of 1,024 samples, or 8.129 s, and will henceforth be referred to as Dataset B. The deployment of a widely used database is highly beneficial for the research project, as it enables the establishment of connections with existing literature and the verification of findings.

4.2 METHODS AND MODELS

This study employs the whole PPG signal to accurately estimate the ABP signal. It is imperative to employ the whole PPG signal, as it offers a more comprehensive representation of the data than the use of extracted features alone. Such data includes physiological information, such as variations in amplitude, shape, and timing, which are crucial for precise ABP estimation [114], [120], [127], [128]. It was evident that a mere examination of features is inadequate for capturing the inherent variations of the entire signal. Several factors influence BP, and these change over time. These aspects are of critical importance for the precise estimation of ABP. Such characteristics reflect the dynamic and complex nature of cardiovascular function, and thus must be taken into account. Static features are insufficient for capturing these variations, which

CHAPTER 4

may result in inaccuracies. The PPG signal comprises a multitude of intricate waveform patterns, including those indicative of systolic, diastolic, and dicrotic points. Each of these patterns offers valuable insights. The most effective means of processing the entire PPG signal is through the use of advanced ML and DL algorithms. These algorithms are capable of extracting and exploiting complex patterns and dependencies within the signal that would otherwise remain hidden when only limited features are used. This comprehensive approach enables the identification of previously unrecognized relationships between the PPG signal and ABP signal, thereby enhancing the accuracy of the estimation. This approach allows for more personalized ABP estimation by accommodating individual variations in cardiovascular characteristics, thereby enhancing the accuracy of BP monitoring and making it more tailored to individual patients.

4.2.1 MODELS

The advent of DL has brought a revolutionary change in numerous fields, including signal processing, through the development of highly sophisticated algorithms that are specifically designed to address a range of tasks. Among these, U-Net [129], [130], Long Short-Term Memory (LSTM) [17], Residual U-Net [121], and MultiRes U-Net [114] are particularly noteworthy for their effectiveness, especially when adapted for one-dimensional (1D) data.

The U-Net was originally designed for biomedical image segmentation. It has also been successfully adapted for 1D signal processing tasks, including time-series analysis and sequence data. The distinctive U-shaped configuration of the network captures contextual information and enables precise localization. This makes it highly suitable for tasks where accurate delineation of signal boundaries is of paramount importance.

LSTM networks are an effective type of RNN used in DL for processing 1D signals. LSTMs are good for tasks involving data in order, like time-series

CHAPTER 4

analysis, speech recognition and anomaly detection. This is because they can capture long-range dependencies and temporal patterns. LSTMs fix the vanishing gradient problem by keeping information in memory for a long time. This makes them very effective at understanding complex patterns and remembering important features from earlier steps. LSTMs can model 1D signals, predict future values and identify patterns. They are used in many areas, including healthcare and natural language processing and are ideal for tasks that require understanding of the sequential characteristics of 1D signals.

The Residual U-Net is an extension of the U-Net. It uses residual connections from ResNet. These connections help the network train deeper models more effectively. In a Residual U-Net, the output of each convolutional layer is added to its input, making it easier for gradients to propagate. This makes the network learn better and does complex 1D segmentation tasks better. It lets the model learn easier-to-optimize residual functions.

The MultiRes U-Net makes the U-Net architecture even better for 1D data by using multi-resolution analysis. The model combines U-Net with residual connections and a multi-resolution block to capture features at different scales. The MultiRes block has multiple convolutional layers with different kernel sizes, so the network can learn both fine and coarse features. This design helps the network to capture multi-scale information, which is important for accurately segmenting signals with different patterns and frequencies. Residual connections make the network trainable and robust.

Each of these architectures offers distinctive advantages in the context of 1D signal processing. U-Net is particularly adept at precise localization, Residual U-Net enhances training depth and efficiency, and MultiRes U-Net facilitates enhanced multi-scale feature extraction. These developments have rendered them indispensable tools in domains such as anomaly detection in time-series data, speech signal processing, and other applications where precise and accurate

CHAPTER 4

1D signal segmentation is crucial.

4.2.2 EXPERIMENTAL CONFIGURATION

This Chapter describes the implementation of the Residual U-Net model, as described by Costa et al. [121], as well as the two models described by Ibethaz et al. [114] in which the Approximation network is a 1D deeply supervised U-Net utilizing deep supervision, while the Refinement network is a 1D MultiRes U-Net. In contrast, the LSTM model has been implemented with four layers comprising 128 hidden nodes, and a dropout layer at the end of each layer with a rate of 0.2, the objective being to prevent overfitting. The learning rate for the model was set to the default value of 0.001, and the Adam optimizer was employed for the training process. The maximum number of training epochs was set to 50.

All subsequent results were obtained using Python 3.11.0 for training DL models and processing Dataset B. MATLAB R2023b was employed for processing Dataset A and evaluating the models. The MAE and RMSE have been employed as performance metrics for the DL models.

4.2.3 LOSS FUNCTION IMPLEMENTATION

As previously stated in the introduction to this Chapter, the utilization of an appropriate loss function is identified as a crucial factor in enhancing the performance of DL models. This aspect has underscored the necessity for further investigation, which is addressed in this Chapter. In view of this necessity, an alternative loss function, distinct from the MSE, was employed to ascertain the optimal one that would ensure improvement.

The loss function that has been implemented is designed to accurately detect systolic and diastolic points within the data set. The implemented function has a

CHAPTER 4

single, clear objective: to minimize the discrepancy between the ABP signal predicted from the PPG signal and the reference ABP signal. This approach enables the model to focus on the most clinically significant features of the signal, as the critical points have been assigned greater weight and higher penalties have been imposed for errors around these peaks. As a result, the model has demonstrated enhanced sensitivity and precision in identifying these key features. This approach ensures that the network prioritizes these points, thereby enhancing its overall performance in detecting anomalies or changes in the signal. This is crucial for accurate diagnosis and analysis in medical applications, such as monitoring cardiovascular health. This is achieved by utilizing a weight function that assigns greater significance to the two points of interest while assigning lesser significance to the remaining points of the signal. The implemented loss weight is shown in **Fig. 32**, compared with the ABP signal.

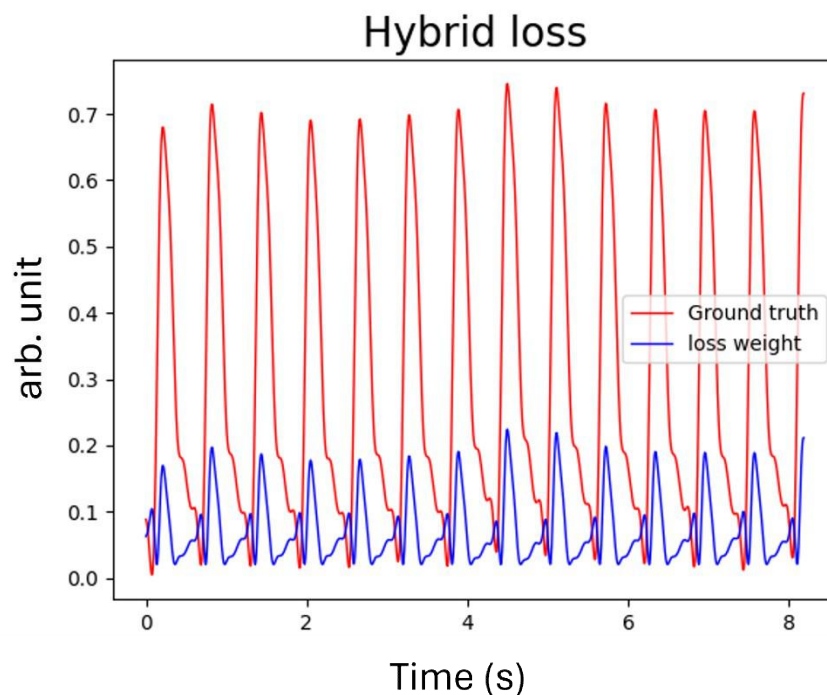


Fig. 32. Loss weight compared with the ABP signal to weight the systolic and diastolic peaks.

CHAPTER 4

This weight function has been implemented by subtracting the mean of the ABP signal from the ABP signal, as the vital signal in question is always positive. This allows for the translation of the signal and the obtaining of negative values. The power of two permits the obtaining of peaks when a systolic peak occurs, as well as when a diastolic point, or valley, occurs. Subsequently, the aforementioned weight function is added to its maximum value multiplied by 0.1. This decision was made in accordance with the necessity of never utilizing a weight with a value of zero. Thereafter, this weight function is utilized to calculate the loss function, which is achieved by multiplying it by the square of the difference between the true and predicted values. The resulting product is then averaged to obtain the mean value. It is explained in the following equations (8):

$$\begin{aligned}\mu_{ABP} &= \frac{1}{n} \sum_{i=1}^n y_i \\ z &= (ABP - \mu_{ABP})^2 \\ weight &= z + 0.1 \cdot \max(z) \\ SErr &= (ABP - \widehat{ABP})^2 \\ loss\ function &= \frac{1}{n} \sum_{i=1}^n (SE_i \cdot w_i)\end{aligned}\tag{8}$$

with $ABP = [y_1, \dots, y_n]$ as the reference signal, $\widehat{ABP} = [\hat{y}_1, \dots, \hat{y}_n]$ as the predicted signal, $weight = [w_1, \dots, w_n]$, $SErr = [SE_1, \dots, SE_n]$ and $n = 1024$ samples.

4.3 RESULTS

In this study, the deployment of a Residual U-Net as shown in [121] has been considered to obtain the ABP signal. Costa et al. paper [121] has been used as a reference because that study presents a comprehensive investigation of ML and

CHAPTER 4

DL models, employing both intra-subject and inter-subject training approaches. Moreover the workflow followed by [114] has been implemented using the two models, approximation and refinement, as mentioned above. In this Chapter, the aim has been to implement a loss function that could potentially enhance results in conjunction with models that have been previously explored in literature. Furthermore, it was possible to gain a more profound comprehension of the impact of input signal duration and the diverse inputs in DL models.

4.3.1 PPG AND ITS DERIVATIVES

In order to facilitate a comparison of the results with [121], PPG and its derivatives of 1024 samples corresponding to a duration of 8.192 s have been used.

This new input dataset has been designated as A4. The Residual U-Net was implemented using an inter-subject approach and MSE as the loss function. The training process utilized 500 epochs and a batch size of 256, with the Adam optimizer. During the fitting process, validation data was provided. The results are shown in **Table 19** and are reported as MAE computed on the test set, because this performance indicator has been reported in Costa et al. paper [121].

Table 19. Comparison of the results with Costa et al for Dataset A4.

	MAE SYS (mmHg)	MAE DIA (mmHg)
This work	15.46	7.19
Costa et al. [121]	18.60	10.94

The enhanced outcomes can be attributed to several factors, including the distinct processing techniques employed to generate the final dataset from the same database. This outcome is noteworthy, particularly in light of the inherent challenges associated with achieving enhancements in the inter-subject approach, which has proven to be a challenging endeavor.

CHAPTER 4

It's interesting to underline that by varying the duration of the signals from 8.192 s (Dataset A4) to 30 s (Dataset A3) without varying the number of samples which is always 1,024, or the model used or the loss function, the better results are obtained using Dataset A4 as shown in **Table 20**.

Table 20. Comparison of results varying the duration.

	RMSE SYS (mmHg)	RMSE DIA (mmHg)	MAE SYS (mmHg)	MAE DIA (mmHg)
8.192 s (Dataset A4)	19.66	9.65	15.46	7.19
30 s (Dataset A3)	21.44	11.59	17.16	8.26

Subsequently, an alternative loss function that differed from the MSE was employed in order to identify the one that would guarantee improvement.

In view of the superior outcomes yielded by Dataset A4 in both predictions, the subsequent table will focus on the utilization of this dataset and of Dataset A3, as well as on the deployment of the implemented loss function and MSE function. In **Table 21** the comparison of results between the use of MSE and the implemented loss function is shown by using RMSE and MAE. The Dataset A3 and A4 have been used.

CHAPTER 4

Table 21. Comparison of results between the use of MSE and the implemented loss functions using Residual U-Net and 30 s PPG and its derivatives (Dataset A3) and 8.192 s PPG and its derivatives (Dataset A4) on test set.

	Loss Function	RMSE SYS (mmHg)	RMSE DIA (mmHg)	MAE SYS (mmHg)	MAE DIA (mmHg)
8.192 s Dataset A4	MSE	19.66	9.65	15.46	7.19
30 s Dataset A3	MSE	21.44	11.59	17.16	8.26
8.192 s Dataset A4	Implemented loss function	19.10	9.56	14.98	7.16
30 s Dataset A3	Implemented loss function	19.94	9.85	15.79	7.64

The aforementioned results pertain to the utilization of 30 s PPG signals and their derivatives with 1,024 samples and 8.192 s PPG signals and their derivatives and two distinct loss functions. As illustrated in the table, the deployment of the implemented loss function facilitates an enhancement in systolic and diastolic predictions.

Thus, the combination of the Dataset A4 with the implemented loss function, in both the systolic and diastolic predictions, yields further improved results.

A comprehensive analysis of the data in the tables, with variations in the durations of signals and loss functions, reveals that the systolic and diastolic predictions using PPG and its derivatives with 8.192 s signals and MSE as the loss function yield improved results, while the use of 30 s signals demonstrates inferior outcomes. Furthermore, the utilization of PPG and its derivatives with 8.192 s signals and the implemented loss function enables additional enhancements. As a matter of fact, the combination of PPG and its derivatives is not affected by the type of prediction (systolic or diastolic), thereby enabling the attainment of superior results for both predictions through the utilization of 8.192 s signals.

CHAPTER 4

4.3.2 PPG SIGNALS AS ONLY INPUT

The following results have been obtained using the same Residual U-Net and the PPG signal as the only input (without derivatives) of the model but varying the signal duration and the loss function.

A first comparison was made by considering 8.192 s PPG signals of 1,024 samples (Dataset A1) and the use of MSE and of the implemented loss function, which is reported in **Table 22**.

Table 22. Comparison of results between the use of MSE and the implemented loss functions using an 8.192 s PPG signal and Residual U-Net (Dataset A1) on test set.

	RMSE SYS (mmHg)	RMSE DIA (mmHg)	MAE SYS (mmHg)	MAE DIA (mmHg)
MSE	17.95	8.04	14.19	6.01
Implemented loss	17.30	7.77	13.86	5.68

In this framework, another aspect analyzed is the duration of the input PPG signal, by comparing results for Dataset A1 and Dataset A2. It has been emphasized that the use of the implemented loss function tends to yield better outcomes. But also, that 8.192 s signals improve the result with respect to the use of 30 s signals as shown in **Table 23**.

CHAPTER 4

Table 23. Comparison of results by using the implemented loss function and MSE and two different lengths of the signal and Residual U-Net on the test set.

	Loss function	RMSE SYS (mmHg)	RMSE DIA (mmHg)	MAE SYS (mmHg)	MAE DIA (mmHg)
8.192 s PPG (Dataset A1)	Implemented loss function	17.30	7.77	13.86	5.68
30 s PPG (Dataset A2)		18.20	7.54	14.58	5.86
8.192 s PPG (Dataset A1)	MSE	17.95	8.04	14.19	6.01
30 s PPG (Dataset A2)		18.95	7.64	15.34	5.82

As a matter of fact, the use of only the PPG signal of 8.192 s and the implemented loss function for both predictions yields superior outcomes compared to the use of MSE. Moreover the 8.192 s signals give better results for systolic prediction than 30 s signals for both the loss functions considering RMSE and MAE. While the use of the implemented loss function consistently yields improvements, the signal duration when only the PPG signal is utilized has a notable impact on performance. In fact, it has been demonstrated that an 8.192 s signal produces superior results in the systolic prediction and inferior results in the diastolic prediction relative to a 30 s signal.

Other results are obtained on a LSTM model and on the models used by Ibethaz et al. [114] as shown in **Table 24** using Dataset A1. It is noteworthy that by varying the model, the systolic prediction is consistently enhanced when the implemented loss function is utilized, whereas the diastolic prediction is adversely affected. Consequently, the implemented loss function always improves the accuracy of the systolic prediction considering all the results shown.

CHAPTER 4

Table 24. Comparison of results by using the two different loss functions and different models on test set.

	Model	Loss Function	RMSE SYS (mmHg)	RMSE DIA (mmHg)	MAE SYS (mmHg)	MAE DIA (mmHg)
	LSTM	MSE	17.42	8.05	13.87	6.31
		Implemented loss function	15.97	8.55	12.56	6.33
Ibethaz et al. models	Approximation Model	MAE	18.18	7.80	14.68	6.02
	Refinement Model	MSE				
Ibethaz et al. models	Approximation Model	MAE	16.64	8.53	13.07	6.51
	Refinement Model	Implemented loss function				

4.3.3 SIGNALS FROM DATASET B

The next results are obtained with Dataset B, this dataset has been processed following Ibethaz's paper. In the **Table 25** the two approximation and refinement models that are employed by Ibethaz et al. are considered. However, the models were retrained, and the results were obtained on the test set using MATLAB, identifying the systolic and diastolic points on both reference and predicted ABP signals and calculating the errors and the performance indicators. This decision was made because Ibethaz et al. indicated that for each estimated ABP signal, the maximum and minimum values among many pulses were considered respectively as systolic and diastolic values, while it is considered that it is more appropriate to consider all systolic and diastolic values of the signal, rather than focusing on a single value.

CHAPTER 4

Table 25. Comparison of results by using Dataset B and the Approximation-Refinement models with different loss functions.

	Model	Loss function	RMSE SYS (mmHg)	RMSE DIA (mmHg)
Results on the retrained models	Approximation	MAE	6.21	3.95
	Refinement	MSE		
Proposed work	Approximation	Implemented loss function	7.42	4.97
	Refinement	Implemented loss function		
	Approximation	MAE	6.15	4.97
	Refinement	Implemented loss function		

As illustrated in the **Table 25** for the models utilized by Ibethaz et al., distinct combinations of loss functions were contemplated, including the integration of the implemented loss function for both models and the maintenance of the loss function for the Approximation model while modifying only the loss function of the refinement model. Evidently, the selection of a linear function for the Approximation model facilitates an enhancement over the use of the implemented loss function.

It is evident that the combination of the MAE function for the Approximation model and the implemented loss function for the Refinement guarantees an improvement in the systolic prediction, while this is not true for the diastolic prediction. This finding is consistent with the results obtained using the other

CHAPTER 4

dataset.

4.4 DISCUSSION

In the context of DL for 1D signal processing, the duration of the signal input exerts a pronounced influence on both the performance of the model and the complexity of the training process. Longer signals provide more comprehensive information, enabling the capture of extended temporal dependencies and subtle patterns. However, this increased comprehensiveness also increases the computational burden and risk of overfitting. Conversely, shorter signals may result in the omission of crucial patterns, leading to underfitting and poor generalization. Hence a quantitative evaluation was necessary.

Indeed, the first results demonstrate the effectiveness of using the PPG and its derivatives of 8.192 s as input for the Residual U-Net after the processing described in **Chapter 1** with results showing clear improvements in both systolic and diastolic prediction compared to Costa et al. [121]. Moreover, the use of 8.192 s signals produces superior results compared to 30 s signals. Furthermore, regardless of signal duration, the implemented loss function consistently enhances results. As a matter of fact, the use of 8.192 s signals and the implemented loss functions gives the best results.

In addition, the utilization of the implemented loss function in conjunction with the PPG signal as the only input (without derivatives) to the Residual U-Net has been demonstrated to result in enhanced performance in both systolic and diastolic predictions also varying the duration of the signals.

Nevertheless, when the model is modified such as LSTM or the cascade of Approximation and Refinement, the implemented loss function enables the attainment of enhanced outcomes solely with regard to the systolic prediction.

Additionally, it seems that varying the dataset and implementing the loss

CHAPTER 4

function in a similar way may yield improved results for the systolic prediction. Based on this consideration it's necessary to underline that the detection of the diastolic point of PPG signals represents a significant challenge, which may explain the motivation behind the different models that produce inferior results when using the implemented loss function. It may therefore be advisable to select the loss function based on the predicted variable. However, it's important to highlight that this deterioration does not occur when the PPG signal and its derivatives are employed.

4.5 CONCLUSION

This Chapter demonstrates that the application of DL to 1D biomedical signals and the implementation of a tailored loss function has the potential to markedly enhance diagnostic and monitoring capabilities. The study highlights that the efficacy of DL models can vary considerably depending on the features of the dataset and on the selected architectural configuration. The Residual U-Net model, with its robust residual connections and the incorporation of PPG and its derivatives, has the capacity to yield superior outcomes in comparison to existing literature with regard to both systolic and diastolic predictions.

Furthermore, the selection of the loss function is crucial for optimizing model performance. Prioritizing clinically significant features, such as systolic and diastolic points in biomedical signals, through the adaptation of loss functions improves the accuracy and reliability of these models. In this Chapter, two distinct loss functions and a variety of model architectures to ascertain the optimal performance for the given task have been employed. It has been shown that implementing a weighted loss function that assigns greater importance to critical points is an effective method for focusing the model on the most relevant aspects of the signal, leading to enhanced diagnostic outcomes. This approach

CHAPTER 4

guarantees that the DL model accurately represents the signal and emphasizes the most crucial parts for clinical interpretation. The use of the implemented loss function has allowed improvements for both systolic and diastolic predictions when used with Residual U-Net, regardless of the model input and segment duration. Furthermore, it consistently demonstrates superior performance in systolic prediction when the model and dataset are varied.

It is evident that comprehensive studies which compare disparate datasets, models, and loss functions are indispensable for the development of robust and generalizable DL solutions. By conducting experiments with different datasets, insights have been gained into how different models perform under varying conditions. This process allowed to ensure that the models are not overfitting to particular datasets but are, in fact, capable of generalizing effectively to novel, unseen data. Furthermore, varying the datasets has revealed that the models perform consistently in accordance with the same criterion. Another aspect that has been subjected to analysis has been the duration of the signals and the different inputs. This has allowed to highlight the superior performance achieved using 8.192 s signals. Additionally, the use of PPG signals as the only input of the model has also been shown to yield enhanced results.

In light of these considerations, it seems clear that a comprehensive understanding of the relationship between signal duration, loss functions, datasets, and model architecture is essential for the development of robust and accurate DL models for the prediction of systolic and diastolic BP. This aspect must be taken into account in accordance with the specific task at hand.

In conclusion, the development of DL models that demonstrate proficiency in processing 1D biomedical signals and the implementation of loss function will contribute to more accurate diagnostics, efficient monitoring, and improved patient outcomes. This will be important for more personalized and effective healthcare solutions.

HARDWARE IMPLEMENTATION FOR AN EMBEDDED SOLUTION

INTRODUCTION

This Chapter presents the design and implementation of a wearable embedded solution for the remote acquisition of physiological data in the framework of telemedicine [3], [4], [5], [6], [131], and it consists of two units. The master board contains the microcontroller, the power supply and the provision for the use of a display that is intended to facilitate greater interactivity. The slave board is equipped with a PPG sensor for monitoring HR, SpO₂, RR, BP, as well as an inertial measurement unit (IMU) with nine degrees of freedom. The placement in direct contact with the lower part of the wrist is strategic as it enhances the accuracy of the parameters while reducing interference with the user's daily movements in order to overcome the motion artifacts problem. The two boards are interconnected using a flat cable that can be easily integrated into a strap. A high-speed serial interface is used for communication between the boards. The firmware has been developed for the asynchronous acquisition of data from the sensors via interrupts, their subsequent processing, calculation of statistics, and transmission to the remote server.

The results demonstrate the efficacy of this design, indicating that the solution is suitable for continuous monitoring of vital parameters, with potential applications in healthcare. This study contributes to advancements in wearable

CHAPTER 5

technologies for the acquisition and monitoring of biomedical data, ensuring the possibility of further innovations. Embedded systems, which are designed to perform specific tasks within larger systems, provide an efficient and reliable means for capturing and processing biomedical data. The acquisition of these data using embedded systems and telemedicine is fundamental in healthcare, offering novel solutions for patient monitoring, diagnosis, and treatment.

It facilitates real-time acquisition and analysis of data, thereby enabling prompt and accurate medical assessments. Such systems are equipped with microcontrollers or specialized processors, which enable the execution of sophisticated algorithms for the processing and interpretation of biomedical signals in real time. This not only improves the speed and efficiency of medical responses but also enhances data security by reducing the necessity for data transmission to external servers.

Patients may be provided with wearable devices that are capable of continuously tracking their health metrics and transmitting data to healthcare providers via secure communication channels. This allows healthcare professionals to monitor patients' conditions, provide timely interventions, and offer consultations without the necessity of physical presence.

Nowadays, a measurement technique that is spreading for real-time monitoring of vital signs is PPG, which permits non-invasive optical measurement of changes of blood volume in tissues [26], [27], [132], [133]. As already discussed, this method employs a light source and a photodetector at the surface of the skin to measure the variations in light absorption, which correspond to the pulsatile nature of blood flow caused by heartbeats. PPG signals are extensively employed in wearable devices for the continuous monitoring of physiological parameters, including HR, SpO₂, RR, BP and stress levels. The simplicity of integration and the minimal discomfort associated with PPG sensors render them optimal for incorporation into wearable health and fitness trackers, allowing users to

monitor their health metrics in real-time and maintain an informed lifestyle [105], [134]. The existing literature reports the development of devices designed for BP estimation using PPG signals acquired at multiple sites, or PPG signals combined with ECG signals [135], [136].

5.1 HARDWARE DESIGN

The architecture of the developed wearable device is structured as a dual-board configuration according to the master-slave paradigm, a common approach in embedded systems that enhances efficiency and resource management, as shown in Fig. 33. In this configuration, the slave board is controlled by the master one, that coordinates its actions and facilitates communication. Moreover, this configuration permitted the physical separation of two sub-systems, with the sensors situated in the lower part of the wrist and the microcontroller (with the possibility of adding a display), positioned in the upper part of the wrist.

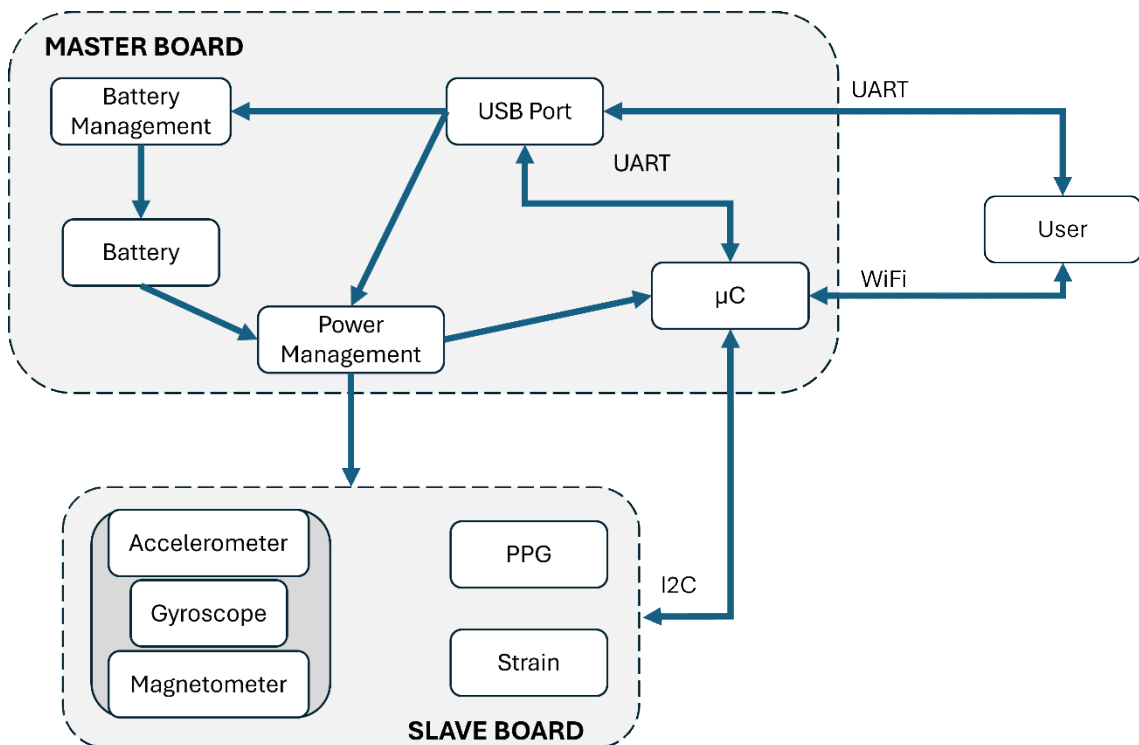


Fig. 33. Developed system architecture.

CHAPTER 5

In accordance with the proposed architecture, the designed master board, shown in **Fig. 34** is the control unit and contains the microcontroller, the conditioning electronics, the battery management system (BMS), and a Universal Serial Bus (USB) port for charging and communication, moreover it guarantees the power management of the system and of its components. It is the primary interface with the user, facilitating interaction through the Universal Asynchronous Receiver-Transmitter (UART) and Wi-Fi.

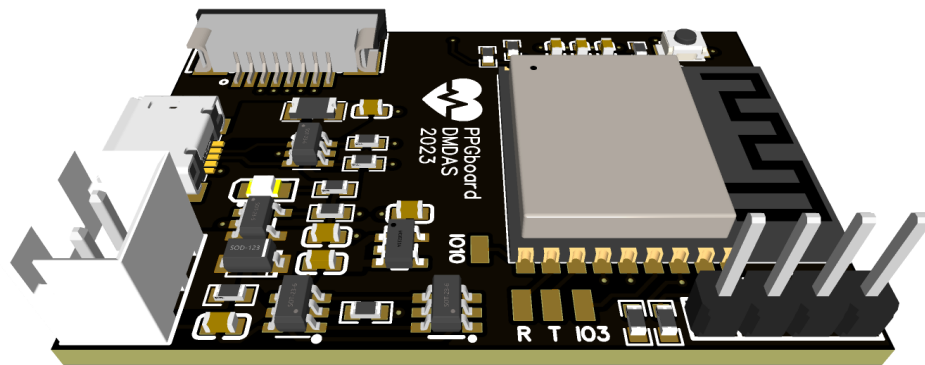


Fig. 34. Master BOARD.

The slave board is located on the lower part of the wrist and is dedicated to sensing. The master board is notified by the slave board, shown in **Fig. 35**, of new data and gives commands. The lower board includes a PPG sensor, a suite of nine-axis inertial sensors, and a piezoresistive force sensor. Its strategic placement enables more accurate data acquisition, less affected by wrist movements. The two boards communicate via an Inter Integrated Circuit (I2C) interface, ensuring efficient and low-latency data transfer.

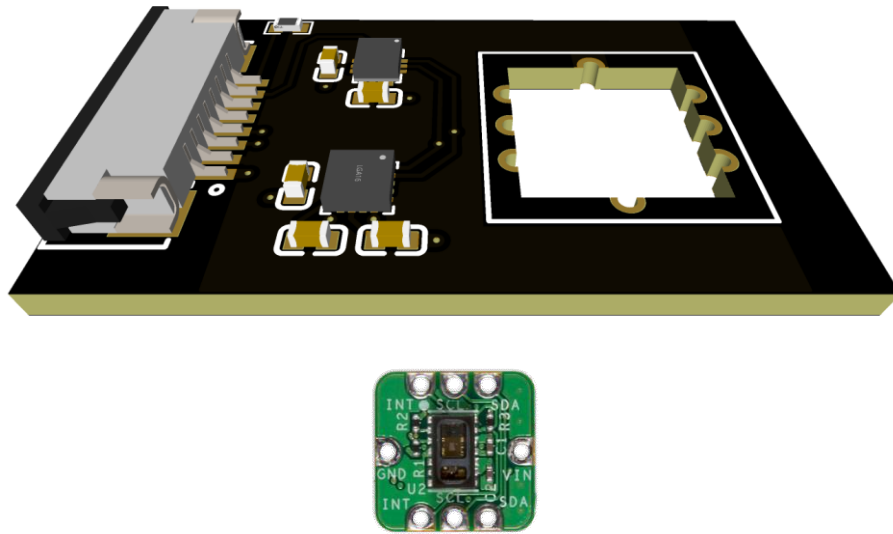


Fig. 35. Slave BOARD. The PPG sensor, not shown here, is soldered into the opening on the right side of the board.

This subdivision enables the optimization of component distribution, thereby enhancing the ergonomics and functionality of the device. Furthermore, it facilitates more effective management of hardware resources and acquisitions.

5.1.1 *DESIGN SPECIFICATIONS*

In the conceptualization stage, the design specifications were established as a reference point for the subsequent hardware design process. These requirements concern a range of aspects related to wearable devices, with the objective of ensuring their miniaturization, efficiency, convenience, and safety.

Firstly, it was essential to reduce the device's size and weight in order to guarantee that it could be worn on the wrist for extended periods without causing any discomfort to the patient. It was imposed a limit of approximately 40x30 mm for both boards considering the average wrist size. Similarly, the dimensions of the LiPo battery (12x31x4 mm) can be accommodated within a case, provided that the overall thickness is not excessive and does not present any anatomical issues. Considering the task to be pursued, it was imperative to utilize a microcontroller with a great processing capacity. This was crucial for the

CHAPTER 5

real-time analysis of data acquired by the sensors and the transmission of data to the server via Wi-Fi. The incorporation of a rechargeable lithium-ion battery was a strategic decision that facilitated the achievement of objectives pertaining to mobility and operational continuity. In fact, the battery enables the patient to utilize the device without the constant need for an external power source, thus ensuring freedom of movement and daily usability. However, the integration of a rechargeable battery necessitates the implementation of a BMS that ensures reliable and efficient charging, preventing overcharging and irreversible damage. Furthermore, since the selected components operate at lower voltages than those of the power supply, it was necessary to provide an appropriate power conditioning circuit comprising a step-down converter and protection ICs. A micro-USB port has been used given the minimal requirements imposed by the design specifications. As a matter of fact, the Micro USB port remains a proven and cost-effective solution. In order to facilitate the replacement of the battery in the event of a malfunction, a 2-pin JST PH connector was utilized. Regarding the sensors, it was necessary for the device to support: a PPG sensor for the detection of HR, SpO₂, RR, etc.; an IMU for the detection of motion and orientation; a force sensor for assessing how the device has been worn.

5.1.2 MICROCONTROLLER

The ESP32-C3 microcontroller was chosen for its features and versatility. It contains a 32-bit RISC-V core that has guaranteed flexibility in firmware development and optimization due to the open-source nature of its toolchain. It operates at a maximum frequency of 160 MHz and exhibits commendable energy efficiency in data processing. The microcontroller is augmented by an internal SRAM memory of 400 kB and a built-in flash memory of 384 kB. One of the most notable characteristics of the ESP32-C3-WROOM-02 module is its integration of a USB interface that enables direct connection without the necessity of additional

CHAPTER 5

components. The USB interface of the module is in accordance with the USB 2.0 specifications and supports Full-Speed mode, thereby ensuring reliable and fast data transmission. The incorporation of the USB interface into the design of the printed circuit board (PCB) has resulted in a notable reduction in the overall complexity and cost of the circuitry, as well as a considerable decrease in the size of the PCB itself. The microcontroller is reachable by an external host system, such as a workstation for firmware development, by means of a virtual COM port thereby facilitating interaction with the device and charging. The module offers advanced connectivity, including Wi-Fi 4 (802.11 b/g/n) and Bluetooth Low Energy 5.0 (BLE). The implementation of Wi-Fi has guaranteed the establishment of a robust communication link and high-speed data transfer with a remote server for data collection. The module's interface with sensors is ensured by the presence of the I2C bus and support for interrupt signals, including both timer and hardware interrupts. The ESP32-C3 has been designed to operate in conditions of low power availability, which is a critical and often underrated aspect of battery-powered wearables. As a matter of fact, it is designed to be highly energy-efficient, with a deep-sleep mode that significantly reduces energy consumption. Additionally, it is capable of intelligently managing the frequency of the clock and disabling non-essential peripherals, further enhancing its energy-saving capabilities.

5.1.3 POWER MANAGEMENT

The power management system has to provide a stable power supply to the various components of the proposed measurement system, while simultaneously protecting them from potential failures or abnormal conditions. The limited battery capacity and the necessity for careful energy management have been taken into account to ensure prolonged operational autonomy without access to recharging sources.

CHAPTER 5

The power management system is situated on the main board, which is subdivided into three subsystems: battery management, battery protection, output voltage adjustment.

The lithium-ion battery is charged by the integrated MCP73832T, a linear controller manufactured by Microchip Technology for single-cell LiPo batteries shown in Fig. 36. This integrated circuit was selected for its capacity to provide safe and controlled charging, which is essential for extending the battery life cycle.

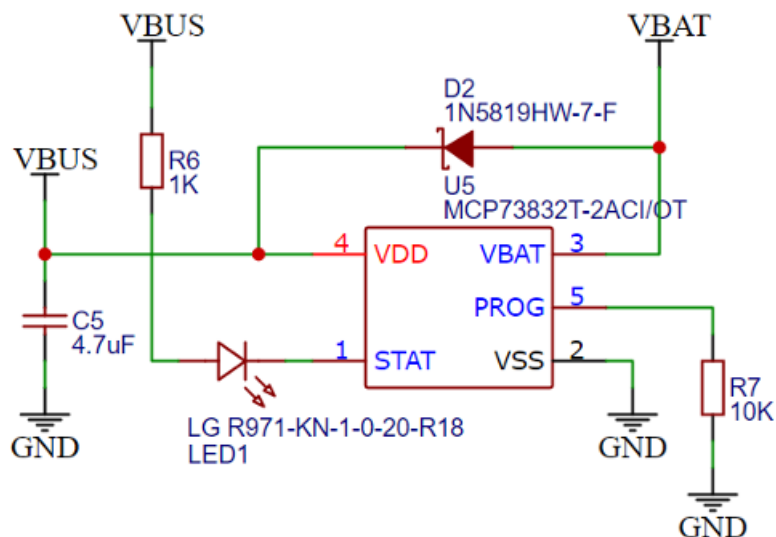


Fig. 36. The schematic of power management circuit based on MCP73832T.

One feature of the MCP73832T is its capacity to regulate the charging current and voltage through the implementation of a three-stage charging methodology: current constant, constant voltage, and end charge phases. During the first phase, the integrated circuit applies a constant charging current until the battery voltage reaches the desired regulation level. Subsequently, during the second phase, it gradually reduces the current until the recharge is complete. Moreover, a programming resistor with a value of 10 k Ω is incorporated into the integrated

CHAPTER 5

circuit's output to limit the charging current to 100 mA to preserve battery health. A Schottky diode, specifically the 1N5819HW model, has been also incorporated. By connecting a LED to the STAT pin of the MCP73832T, it was possible to implement a battery charge status indicator. Specifically, the LED illuminates during charging and turns off when charging is complete. The remaining passive components of the battery management subsystem play an important role in stabilizing the operation of the integrated circuit. For example, the 4.7 μF capacitor is responsible for filtering noise and stabilizing the input voltage, which greatly improves the effectiveness of the charging process. The device battery is safeguarded and regulated by a circuit comprising the DW01A integrated circuit and the FS8205 dual MOSFET in **Fig. 37**.

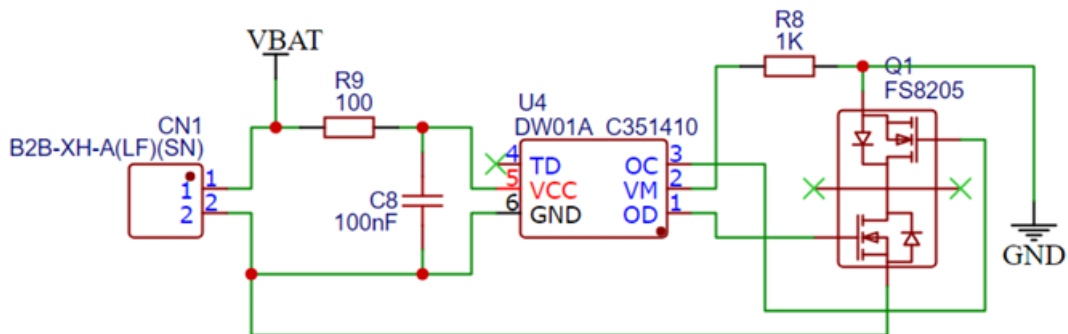


Fig. 37. Schematic of DW01A and of FS8205.

The DW01A is an integrated circuit that monitors the voltage of the battery and the current being sourced or sinked, thereby ensuring that the battery remains within its safety limits. In the event of an overcurrent or over-discharge condition being detected, the integrated circuitry will interrupt the circuit in order to prevent damage to the battery. This mechanism is achieved by the activation or deactivation of the dual FS8205 MOSFET, which serves as an electronic switch for battery connection. The FS8205 is configured as a two-way switch, enabling

CHAPTER 5

or preventing current flow contingent on the conditions monitored by DW01A. In the event of an abnormal condition, such as a short circuit, DW01A commands the FS8205 to immediately cease the flow of current, thereby protecting the battery and the entire system. One of the distinctive features of the microcontroller is its ability to operate at a voltage of 3.3 V, which can be derived from the 5 V supplied in input via port USB or from the 4.2 V supplied via lithium-ion battery. To ensure a stable supply voltage compatible with the various components of the system, the TLV757P voltage regulator, produced by Texas Instruments, was utilized as shown in **Fig. 38**. This is a linear regulator that performs the function of converting the input voltage to an output voltage of 3.3 V.

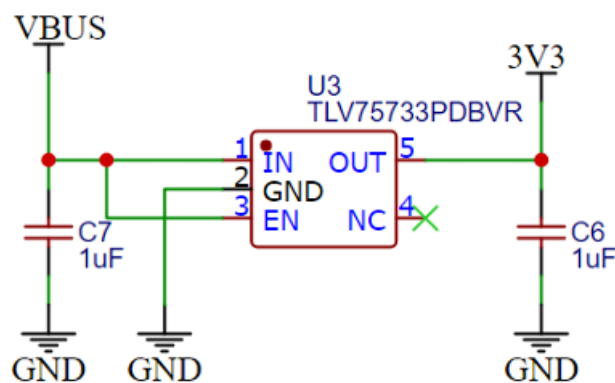


Fig. 38. Schematic of TLV757P.

This LDO (Low Dropout Regulator) has been selected for its particularly low voltage drop, this allows for higher energy efficiency than other integrated systems in the same category. Once more, two 1 μF capacitors were situated at the input and output of the voltage regulator, respectively, with the objective of performing the functions of filtering and stabilizing voltages. This was done in order to reduce electrical noise and improve transient response.

5.1.4 SAFETY

To prevent the entire solution from being compromised by overvoltage and overcurrent, a fuse and a bidirectional diode array were incorporated as shown in Fig. 39. Additionally, a 100 nF capacitor was placed on the line input power supply to filter high noise and stabilize the voltage supplied to the system.

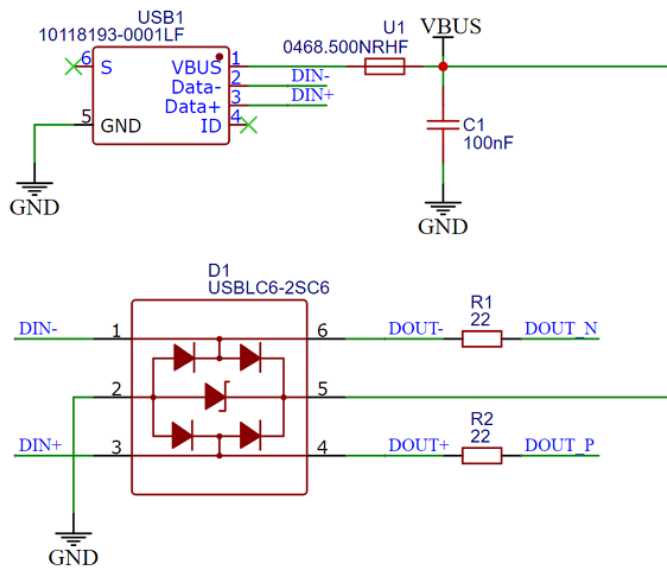


Fig. 39. Protection circuit.

The incorporation of 22 Ω resistors (R1 and R2) on the DOUT+ and DOUT- lines reduced reflection phenomena that typically compromise signal integrity and transmission. This adaptation is necessary to meet the 90 Ω differential characteristic impedance required for USB data lines, thereby enhancing the reliability of communication. The Littelfuse 1206 Slo-Blo Fuse Series 468 is a thin-film device that serves to protect the circuit from overcurrent. It opens when the current exceeds the threshold value and automatically resets once the current returns to a safe level. This functionality helps to prevent damage to downstream components. The USBL6C6 protection integrated circuit from STMicroelectronics

CHAPTER 5

is a diode array designed to safeguard against transient overvoltage and electrostatic discharge. The dual-diode configuration provides bidirectional protection, absorbing and redirecting voltage spikes to ground while safeguarding the microcontroller pins from surges that may occur during USB cable insertion or removal, up to a maximum of ± 15 kV. The low capacitance (3.5 pF) and low internal resistance of the integrated circuit (1Ω) maintain signal integrity and data transfer rate. The incorporation of this integrated circuit was of great importance to guarantee the durability and reliability of the system in operational environments susceptible to electromagnetic interference and static discharge.

5.2 SENSORS

The three digital sensors chosen for this project are Maxim Integrated MAX30102, BMI270 from Bosch Sensortech, and QMC5883L from QST Corporation.

These sensors were selected for their ability to provide a framework that is accurate and highly representative of the conditions of the patient, from physiological parameters to his movement.

An additional analog sensor has been added to the system, namely thin film piezoresistive force sensor, to be installed between the lower board and the wrist for the monitoring and compensation of the forces exerted by the wrist during the acquisition of the patient's biomedical parameters. It is a resistive sensor, whose resistance varies in accordance with the pressure exerted by the wrist, so a simple voltage divider was incorporated into the circuitry to convert changes in resistance into changes in voltage. To facilitate communication between the hosted sensors and the secondary board and microcontroller, an 8-pin flat cable was utilized. This type of cable has been demonstrated to be ideal for its flexibility and capacity to adapt to the anatomical shape of the wrist, as well as

CHAPTER 5

its ability to be easily integrated and hidden in a strap. The utilization of the flat cable has led to the inclusion of FPC (Flexible Printed Circuit) connectors, which ensure a stable electrical connection, thereby reducing the likelihood of accidental disconnection.

5.2.1 MAX30102

The MAX30102 is an optical sensor designed by Maxim, shown in **Fig. 40**, for the measurement of HR and SpO₂ by using the PPG technique.

The device employs two LEDs to emit light at specific wavelengths, specifically red and infrared. The light emitted by these LEDs penetrates the tissue and is partially reflected by the blood. Through the use of a photodiode, it is possible to capture the variations caused by the heart pulses, thereby converting them into signals. These signals are then digitized by an 18-bit Analog to Digital Converter (ADC), resulting in the acquisition of accurate information regarding HR and SpO₂.

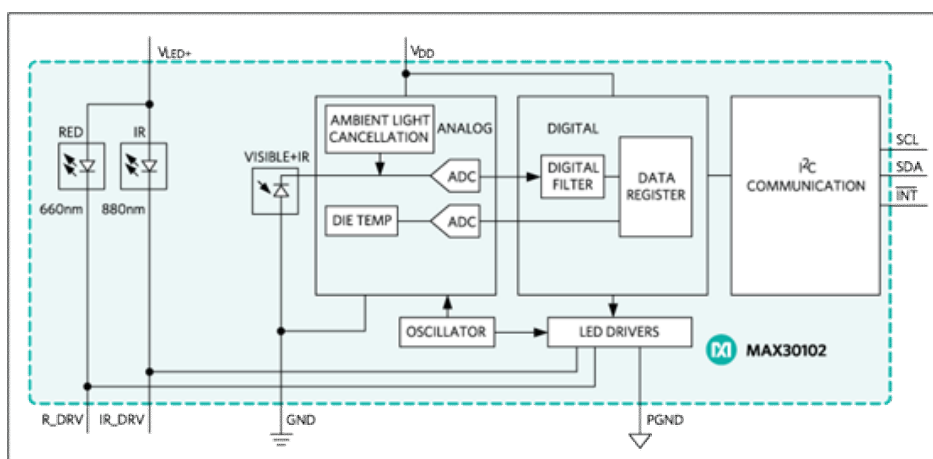


Fig. 40. Functional diagram of the MAX30102 [137].

The MAX30102 sensor has not been utilized in its standalone configuration as shown in **Fig. 41**. It was preferred to use the MAXREFDES117 module which, in addition to MAX30102, also houses: the MAX1921, which is a step-down

CHAPTER 5

converter that adapts the supply voltage to the sensor requirements (1.8 V) and its LEDs (3.3 V); and the MAX14595 that is a level translator that adapts the logical levels of the sensor to the microcontroller.

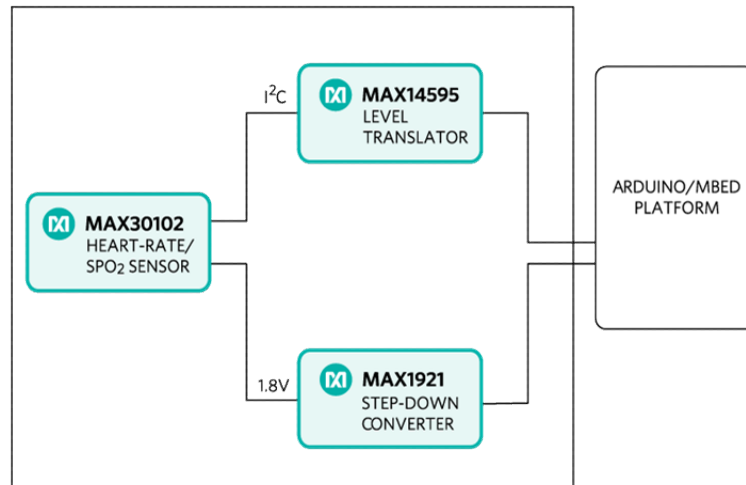


Fig. 41. Components of the MAXREFDES117 [138].

5.2.2 BMI270

The BMI270 is a 6-axis IMU manufactured by Bosch Sensortech for incorporation into wearable and portable applications. This device contains a triaxial MEMS (micro electro-mechanical systems) accelerometer and a triaxial gyroscope, which are utilized for motion detection and the management of wrist orientation. One of the defining characteristics of the BMI270 is its minimal energy consumption, perfect in applications where the solution is battery powered. The BMI270 can operate within a dynamic range of ± 2 g to ± 16 g for the accelerometer and ± 125 deg/s to ± 2000 deg/s for the gyroscope. Both have a 16-bit resolution, in particular 0.06 mg/LSB for the accelerometer and 0.004 dps/LSB for the gyroscope. The output data rate (ODR) is from 12.5 Hz to 1.6 kHz for the accelerometer and from 25 Hz to 6.4 kHz for the gyroscope. While the noise density is $160 \mu\text{g}/\sqrt{\text{Hz}}$ for the accelerometer and $0.008 \text{ dps}/\sqrt{\text{Hz}}$ for the gyroscope. The device offers a low-power mode and a suspension mode, as well as an I2C

CHAPTER 5

bus interface.

5.2.3 QMC5883L

The QMC5883L is a triaxial magnetometer, manufactured by QST Corporation. The device employs AMR (anisotropic magneto-resistive) technology, enabling it to attain up to ± 8 G range, a resolution of $0.1 \mu\text{T}$ and high accuracy in fact it enables 1° to 2° compass heading accuracy. The QMC5883L is designed for integration into low-power devices, with a typical current consumption of less than $100 \mu\text{A}$ under standard operating conditions. Furthermore, the sensor's power efficiency is enhanced when it is on standby or sleep mode, which contributes to the extension of battery life when the system is not connected to a power source. The 16-bit ADC transmits the output data to the microcontroller via the I2C interface.

5.3 PCB DESIGN

A classic two-layer stack-up was used to design the two boards, with the feeder polygons on the top layer and the copper fill polygons on the bottom layer. The top layer is used primarily for signal and power, while the bottom layer is used for ground and very short signal traces. The use of polygons in the top layer allows power voltages to be distributed with a significant reduction in resistive losses. The ground plane of the bottom layer serves as a common reference for the circuit and contributes to effective management of interference and electrical noise. The thickness of each printed circuit is 1.6 mm, with a solder mask of 0.01 mm. The corresponding layer is 0.035 mm, and the core is 1.5 mm. Signal integrity has been considered in the design of the PCB layout.

The initial phase of the process was the placement of the components on the two boards. During the placement phase, it was essential to take the necessary

CHAPTER 5

precautions to ensure a stable and clean power supply. This involved placing the filter supply capacitors near the components that required them. The function of the filter capacitors is to stabilize the voltage and to attenuate current fluctuations, which could otherwise result in the generation of noise and interference within the circuit. The placement of the components near the power pins of the integrated circuits allows for a reduction in the inductance and resistance of the connections. Once the placement of the components was finished, the tracks were traced. To further improve the layout and management of the connections between the two layers of each board, vias were used. These are through holes that allow track connections between layers, facilitating the creation of an efficient electrical path and improving space management on the board. The utilization of vias was optimized with the objective of minimizing parasitic inductances. Additionally, special attention was given to the minimization of ground loops and the management of electromagnetic interference, with the aim of ensuring that signals passed through the circuit without distortion. Any power or ground planes were interrupted beneath the microcontroller antenna. This was crucial for the prevention of electromagnetic interference, which could otherwise affect the overall performance of the system, because the presence of a feed or ground plane could have resulted in disturbances thereby reducing signal quality and communication range. Moreover, the area beneath the antenna was maintained free from any conductive traces to guarantee the optimal functionality of the microcontroller communication system. A cut-out was created on the slave board to facilitate the integration of the MAXREFDES117, thereby maximizing the quality of the sensor's adhesion to the wrist. The configuration of the cut-out enables the creation of holes that closely resemble those with a castellated structure, while simultaneously reducing the cost burden associated with production. In fact, this approach allows for the same functionality to be achieved in a more cost-effective

CHAPTER 5

manner, but with a slightly less refined result.

5.4 SYSTEM FUNCTIONALITIES

The device firmware has been optimized to facilitate the simultaneous processing of multiple sensors. The device establishes a connection with the Wi-Fi network and transmits its local IP address within the network via the serial port. The device boot time is calculated, and the local time is synchronized through a request to the Network Time Protocol (NTP) server, which is initiated via Hypertext Transfer Protocol (HTTP). A Hypertext Markup Language (HTML) page for the purpose of modifying parameters is accessible at the communicated local IP address. The device remains in a listening state until the required configuration parameters have been correctly specified, accompanied by a notification of the outcome. Afterwards, the selected sensors are enabled, and the setup operations are performed. The system is capable of asynchronous acquisition from the sensors, which is triggered by interrupt signals and permits the insertion of collected data into circular buffers. When the predefined number of samples has been acquired, the data is transformed into a format conforming to a purposely defined communication protocol. Upon completion of the acquisitions, the device transmits the formatted data to the server, which is then acknowledged with a positive message indicating the completion of the acquisition task. Subsequently, the signals from the server can be processed to obtain biomedical parameters, such as HR, SpO₂, RR, BP. An interface has been developed in MATLAB to visualize the acquired PPG signals and estimate key vital parameters. The ultimate goal is to enhance the processing algorithms for more accurate vital parameter estimation, including BP. In order to achieve this, a dataset must be created, which should be collected using the prototype designed to acquire PPG signals and the corresponding BP readings obtained

CHAPTER 5

with a sphygmomanometer. The MATLAB interface enables the configuration of acquisition parameters for the PPG signal, taking into account the specific characteristics of the sensor as shown in **Fig. 42**. Furthermore, it enables the generation of a text file comprising patient data, which is crucial for the compilation of a comprehensive dataset.

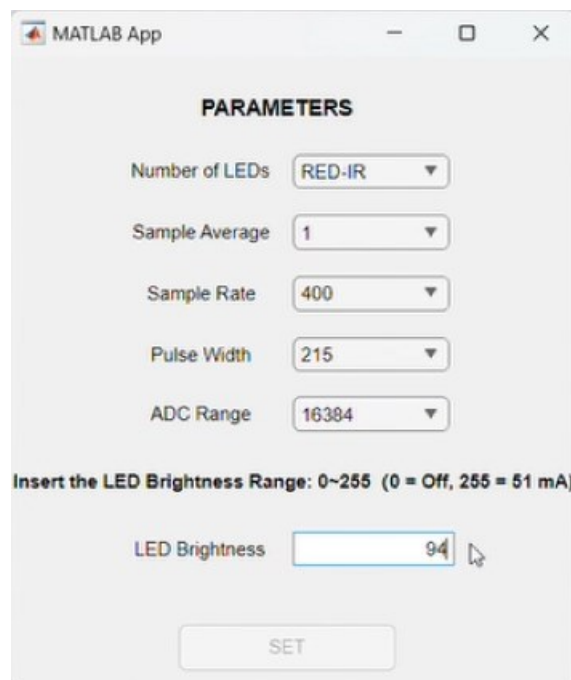


Fig. 42. Parameters for the acquisition.

The **Fig. 43** shows an example of signal acquisition in the red and infrared wavelengths, along with the estimation of vital parameters. This process will be further enhanced by the inclusion of BP estimation.

CHAPTER 5



Fig. 43. MATLAB interface for PPG signal acquisition and vital parameters.

The integration of data coming from the accelerometer, gyroscope and magnetometer can be very useful since it will permit to study motion artifacts that may compromise vital signs measurement. Indeed, a useful application of the proposed system can be the monitoring of a person even while driving, giving valuable information about the driver's condition such as fatigue, drowsiness, stress, and distraction. In this case the challenge lies in the vehicle vibration caused by road's condition, vehicle's type, and shock absorbers, that can reduce the quality of vital sign measurements. The development of such a driver monitoring system (DMS) [139] may enable the study of the comfort and safety of the driver, which is related to road roughness, environmental conditions, and physiological indicators.

5.5 CONCLUSION

The results obtained demonstrate the effectiveness of the modular design adopted, which not only optimized the distribution of components while improving the ergonomics of the device, but also enabled efficient management of hardware resources and data acquisition. Furthermore, experimental tests confirmed the proper functioning of the wearable device, demonstrating its ability to host a web page for setting sensor parameters, acquiring data, formatting it, and sending it to the server. Nevertheless, it became evident that the management of multiple acquisitions necessitates further enhancement. The proposed solution offers potential applications in various areas, including healthcare, driver's health [139], continuous monitoring of HR, RR, SpO₂, BP, which will facilitate further developments in the field of wearable technologies. In the future, further optimizations, integration of new sensors, and implementation of advanced algorithms for data analysis will allow for the expansion of system functionalities and applications for non-invasive monitoring of biomedical parameters.

OTHER BIOMEDICAL APPLICATION FOR A TELEMEDICINE SOLUTION⁵

INTRODUCTION

Wearable technologies for health monitoring, including smartwatches and fitness trackers, have captured the attention of consumers in recent years. Wearable devices are no longer just for tracking simple fitness measurements like steps. They are also used to monitor important health data and telemedicine systems transmit data to healthcare professionals, ensuring proper assistance. This is best achieved through the use of wireless communication protocols like Wi-Fi or Bluetooth technology, as demonstrated in [140].

The literature contains several systems that measure and share medical parameters, making vital signs measurements available online [140], [141], [142], [143], [144], [145]. However, the integration of measuring devices from different manufacturers has remained a significant challenge. Many systems are based on purposely developed hardware, which further complicates matters. This Chapter presents the software development for integrating a new Bluetooth medical device, Checkme Pro, manufactured by Viatom[®], into a web-based telemedicine solution. This telemedicine solution fully exploits the potential of the medical device, which can also be worn using a wristband or waist belt. This activity has

⁵ This Chapter is based on [5].

CHAPTER 6

been conducted as part of a telemedicine project carried out by a company in the medical sector. The goal was to implement the hospital at home paradigm.

The chosen architecture, based on a smartphone app, a database, and a web app, provided the necessary flexibility to tailor it to the project's needs. Specific implementation solutions were used to enable real-time monitoring of patients at home, based solely on measurement data. Furthermore, this work addressed the need to store additional health data not originally calculated by the medical device, including glycemia, BP, and SpO₂ classification.

The manufacturer currently provides only two options for downloading data to a PC: a cabled connection or an app to save data to a smartphone via Bluetooth. The user receives a PDF report for each measurement. An Android app has been developed and it allows patients to download data using Bluetooth connectivity, send it to a database, and visualize it in a web app. This overcomes the limits of the manufacturer's solution. This integration will allow data to be included in a telemedicine system. This data can then be retrieved from a database and displayed in a telehealth room via a dashboard. Furthermore, although numerous Bluetooth-compatible devices are currently on the market, most of these devices only store data locally on the smartphone, which severely limits their potential for use in telemedicine. The smartphone allows the use of medical device anywhere, making the telemedicine solution portable and enabling data transmission to a doctor for analysis, diagnosis, treatment prescription, or advice. This allows to monitor useful parameters non-invasively.

The system has recently been enhanced with a new feature: the ability to obtain BP from ECG and PPG after calibration with an auxiliary device, namely a digital sphygmomanometer, which communicates with the medical device via Bluetooth. Each user must be calibrated every three months. To do this, it's possible to acquire daily check signals using the medical device and BP measurements using the sphygmomanometer at the same time. The medical

CHAPTER 6

device uses PTT to obtain systolic BP by acquiring ECG and PPG waveforms simultaneously during the daily check function. This innovative method for BP measurement is currently being researched [12].

6.1 ARCHITECTURE OVERVIEW

For clarity, the different architectural styles must be classified according to the aspects given in [146]: the communication type is defined by factors such as Service Oriented Architecture (SOA) and message bus; the deployment type is defined by factors such as client/server, N-Tier, and multitenant cloud; the structure type, such as component-based and layered architecture.

SOA enables communication between a service and its provider, ensuring adaptability and integration into a highly distributed system. However, SOA is a monolithic architecture, and microservices have emerged as the architectural style of choice for decomposing business tasks into a distributed system of services. In this context, Representational State Transfer (REST) is the most commonly used architecture for creating web service application programming interfaces (APIs) that can be used with HTTP. It imposes a set of constraints on the design of web services.

A message bus architecture guarantees communication between software systems or subsystems using a message-oriented middleware approach.

N-Tier separates features into segments for tiers located on physically separate computers. The client/server architecture is a two-tier architecture that separates the system into two applications. The client makes requests to the server, while the server contains a database and the relevant stored procedures that implement the application logic. Cloud computing is the new model for network access to shared resources.

This Chapter presents a three-tier architecture, as illustrated in **Fig. 44**. It consists

CHAPTER 6

of the Android app that reads data from the medical device via Bluetooth and shows and stores it on the smartphone; the server accepts data sent by the smartphone and stores it on a MariaDB database; the web dashboard retrieves data from the database and shows it to users and healthcare professionals.

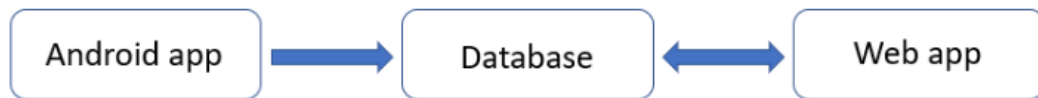


Fig. 44. Block diagram of architecture developed.

6.2 SOLUTION'S IMPLEMENTATION

The Android app is the solution for connecting a smartphone with that medical multi-parametric vital sign monitor. This device is a low-risk, portable medical device that has been classified and certified as Class 1 by the US Food and Drug Administration (or equivalently as Class I under the EU Medical Devices Regulation). It supports dual mode connectivity: Bluetooth Classic and BLE 4.0. This medical device allows for the monitoring of vital signs using internal sensors as well as external accessories. It can measure HR using a single lead ECG, temperature, SpO₂, sleep, and motor activity. Furthermore, BP and glycemia can be accurately measured using auxiliary sensors via Bluetooth connectivity.

The application can read and download data from the medical device using Bluetooth connectivity. It also allows to read downloaded data and send it by HTTP requests to a database, where it can be displayed in a web app that has been specifically developed for this purpose.

6.2.1 COMMUNICATION PROTOCOL OF THE CHECKME PRO

This project uses Bluetooth technology to download data from the medical device

CHAPTER 6

to an Android device. The user interface was created in Android Studio using the software development kit (SDK) of the medical device and Kotlin programming language.

Bluetooth technology is the optimal wireless data transmission standard for exchanging information between different devices. It is an economical and secure method that uses the 2.4 GHz frequency in the ISM band (Industrial Scientific and Medical band) [147]. The medical device supports both Bluetooth 2.0 and BLE 4.0, with a frequency range between 2.4 Hz and 2.4835 Hz, allowing to create a point-to-point network topology with a maximum distance of 100 m indoors. The Bluetooth SPP and SPPLP profiles are supported, which emulate a serial cable connection.

As stated in the communication protocol provided by the manufacturer, the medical device acts as a slave during each communication session, with the connection requested by a master. Command packets are sent from the master to the slave, which replies with a data packet. In case of a CRC (Cyclic Redundancy Check) error or if a timeout occurs, the command packet is retransmitted.

Once the medical device is located, data can be accessed from the smartphone. It uses the device's Universally Unique Identifier (UUID) and two UUIDs for notification and writing to manage the connection between the medical device and the Android device. The Bluetooth interfacing protocol uses command and response packets. The *BTConstant.java* file of the software project defines the command packet lengths and values.

6.2.2 ANDROID APP

In order to receive data, it is necessary to connect the medical device in question with an Android mobile device that is Bluetooth 4.0 compliant and on which the developed application has been installed. Upon detection of the medical device in Bluetooth mode, the acquired data may be downloaded via a designated

CHAPTER 6

protocol. Subsequently, the downloaded data are stored in smartphone memory, thereby enabling the user to access the data in offline mode. To enhance flexibility, all data are managed internally via a data class bean in Kotlin, which enables the initialization of values that are subsequently modified following data retrieval.

The user interface was developed using XML files due to the fact that Android Studio provides a straightforward XML vocabulary and also offers a layout editor that allows for the construction of XML layouts through a drag-and-drop interface. The data visualization functions permit the user to view information pertaining to a specific user ID that has been selected. Subsequently, a menu may be visualized, displaying all the different acquisitions of vital signs and the measurements made. For each measurement, emoji are displayed alongside the data to facilitate comprehension for non-expert users. The use of different emoji is managed by the medical device, therefore only the corresponding bytes can be managed. **Fig. 45** illustrates several measurements performed with the daily check function, as well as systolic non-invasive BP obtained after proper calibration. **Fig. 46** depicts a scenario where calibration was not performed.

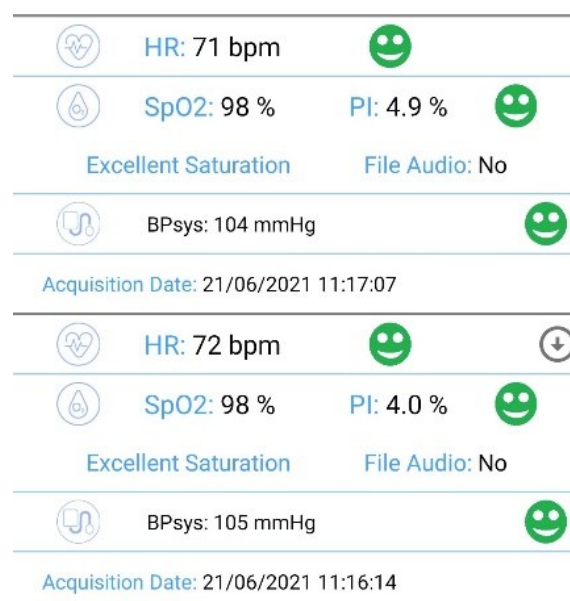


Fig. 45. Daily check measurements, after calibration of BP by means of a

CHAPTER 6

sphygmomanometer. The second measurement (top) is repeated about 1 minute after the first one (bottom).

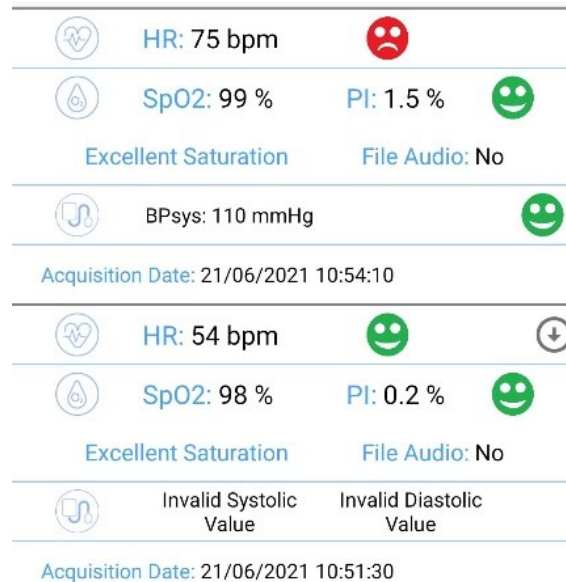


Fig. 46. Daily check measurements, before (bottom) and after (top) calibration of BP by means of a sphygmomanometer.

Communication with the server has been developed with a specific HTTP API, with the purpose of sending data to a database web application. All data are inserted in JavaScript Object Notation (JSON) strings using the Jackson library, and an ObjectMapper has been created to facilitate the serialization of an object of type Bean into JSON. Subsequently, the HTTP request was configured by defining the type and properties of the aforementioned strings. Subsequently, the *OutputStreamWrite* class and its *write()* method were employed to transmit the data string to the Uniform Resource Locators (URL) of the database. Furthermore, device information can be obtained and transmitted to the database via an HTTP POST request.

Fig. 47 illustrates the interface through which data can be transmitted via HTTP requests to the database.

CHAPTER 6

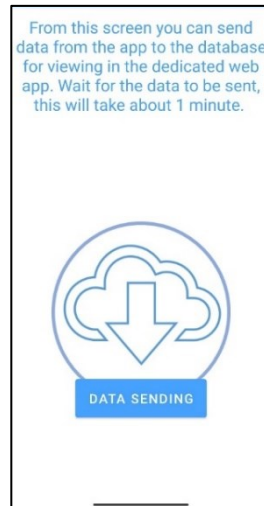


Fig. 47. Data sending screen.

It is possible to send data to the web application via several different connection threads. On the server side, Hypertext Preprocessor (PHP) scripts are employed for the purpose of data reception and the establishment of a database connection for the storage of the data.

In order to facilitate communication with the server, it was necessary to create an *.xml* file for the purpose of configuring the network security. This allows applications to customize their own settings in a declarative manner, without the need to modify the application code. In this file, the URL of the server in question should be specified.

Moreover, the “My Device” menu provides access to information regarding the device in question. Upon establishing a connection with the medical device, the JSON string is returned and can be conveniently displayed or transmitted via an HTTP POST request to the database for visualization in the web application. In the event that the medical device is not connected, the general details of the device are displayed.

6.2.3 DATABASE STORAGE

The server application was developed using XAMPP, a software platform

CHAPTER 6

comprising Apache HTTP Server, MariaDB database, and tools for PHP and Perl programming languages. Indeed, the software includes a PHP 8.0.8 interpreter and the “phpMyAdmin” 5.1.1 application for the management of web-based databases. All data are inserted into the database via PHP scripts, which are used to create new tables and to insert data using PHP functions.

Several HTTP requests to particular URLs refer to scripts written in the PHP programming language, which are used for the creation of tables and the entry of data. As the data were transmitted in the JSON string format, it was essential to correctly parse the string and verify its integrity. A total of 12 tables were created for the purpose of collecting various types of measurement data. The tables are utilized for the collection of users’ data, SpO₂ and pulse index (PI), BP, glucose levels, temperature, sleep monitoring, and motor activity. Additionally, there are tables for the collection of daily check acquisitions, ECG metadata (including the timestamp, electrode placement, and identified health status), and information about the device. In addition, two further tables have been employed for the purpose of collecting ECG waveforms from the daily check and ECG measurements. These also include ECG information such as QRS, QT, QTc, ST durations, HR, filtering mode, and electrode placement. In addition, the database also stores health status bytes, which are the result of a classification performed by the medical device based on the ECG waveform. Glycemia, BP, and SpO₂ classifications that are not performed by the medical device are instead calculated by the Android application through the use of thresholding and stored in the database.

All the tables were populated in a uniform manner, with distinct parameters for each, and each table has its own primary key.

As a prerequisite to accessing the database, two scripts are employed to define the requisite database parameters and to establish a connection.

To facilitate the storage of data, a series of PHP scripts were developed to

CHAPTER 6

accommodate the diverse range of measured quantities. In each script, the function `file_get_contents()` enables the reception of JSON data in the form of a file from the smartphone and its subsequent reading into a string. Subsequently, the JSON string is decoded using the `json_decode()` function, which converts it into an associative array. For each key, the corresponding value is retrieved and stored in the database using the SQL command `INSERT INTO`. In the event that a database table does not already exist, one will be automatically created.

6.2.4 WEB DASHBOARD

The web application has been developed using HTML and PHP on the XAMPP server. The user interface is structured with a homepage and a menu, which allows the user to select the desired function. The data may be presented to the user in tabular form or with plots. From the menu, the user may select a specific measurement quantity. **Fig. 48** illustrates the customized web app and its menu. The data are organized as follows: in the “Measurements” section, users can view the following data: personal information; ECG data with electrode placement; SpO₂ data with acquisition type, PI, and HR; sleep monitoring data with time, minimum, and mean SpO₂; temperatures and acquisition type; and other pertinent data; in the “Graphs” section, users can view the time behavior of all measurements. As an illustration, the daily check section enables the user to select HR, SpO₂, PI, and the systolic value of BP, and to plot these variables. The plotting of ECGs and other quantities has been implemented using JpGraph, which is a crucial feature for providing an overview of a patient’s health condition and monitoring improvements following a therapeutic intervention.

CHAPTER 6

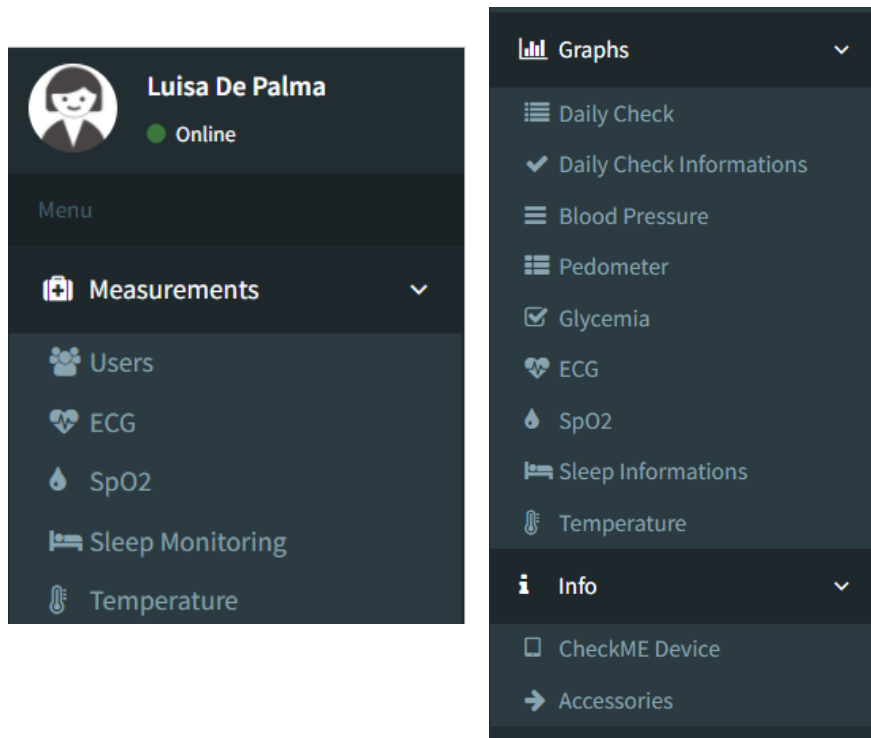


Fig. 48. Sections of the web app menu.

For each measurement, a query is generated and executed against the database in order to retrieve the requisite data and display it. Another implemented function is the selection of all data pertinent to a specific user ID. Furthermore, the final section enables the retrieval of data pertaining to the device and accessories utilized. All fields that may be populated by the user are validated, and the user is alerted in the event of an error. Fig. 49 illustrates the user IDs and their corresponding personal data in tabular form, whereas Fig. 50 depicts the HR time behavior in a graphical format.






Users					
	Id	Name	Sex	Weight	Height
	1	Guest	M	--	--
	2	giovanni	M	77 kg	170 cm
	3	Luisa	F	62 kg	162 cm
	4	PROVA	F	60 kg	160 cm
	5	Altro	M	70 kg	170 cm

Fig. 49. Personal data of user section.

CHAPTER 6

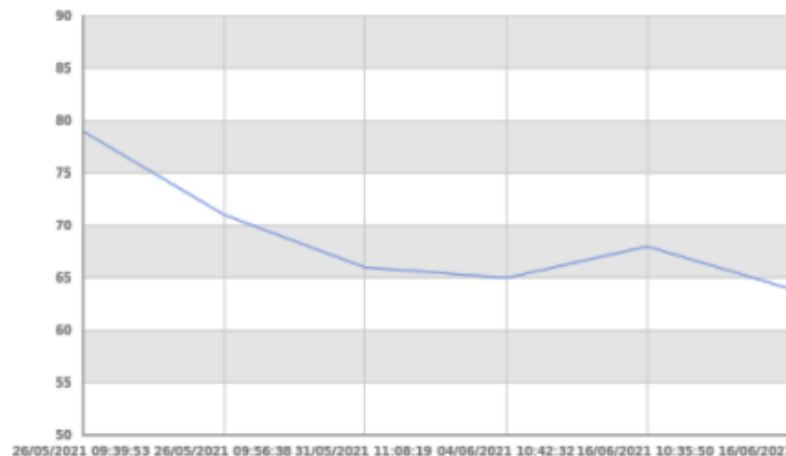


Fig. 50. Plot of HR with timestamp of acquisitions. View of web app screen.

6.3 VALIDATION

The simulation and validation processes are of great importance in numerous fields of engineering, including, but not limited to, photonics [148], sensor networks [149], and bioengineering as it pertains to surgical procedures [150]. Consequently, a series of tests were performed on the Android application to simulate the vast majority of potential usage scenarios. It was of fundamental importance to conduct back-end testing to ensure the accuracy and integrity of the database schema, tables, and triggers. Consequently, a series of operations were executed, including record insertions, queries, and deletions, to ascertain the accuracy and integrity of each action initiated by the Android application. Subsequently, cross-browser compatibility testing was conducted to ascertain the availability of web app features and functionalities for users of disparate browsers, with the objective of verifying graphic and layout consistency. Furthermore, the criteria for input field validation were also verified.

A validation test was conducted to ascertain the equivalence of the data stored in the database and that displayed by Android and web applications. A further comparison was conducted between the data displayed by both applications and those presented by the desktop application provided by the manufacturer.

CHAPTER 6

Furthermore, the responsiveness and ease of use have been verified.

The data illustrated in **Fig. 45** pertain to acquisitions obtained from the same patient using the certified medical device, with a one-minute interval between acquisitions. It is evident that the SpO₂ remains unaltered, whereas the other quantities exhibit a minimal change. The HR exhibited a decrease from 72 to 71 bpm, while the systolic BP value demonstrated a slight decline from 105 to 104 mmHg. Additionally, the PI exhibited a modest increase from 4.0% to 4.9%. As illustrated in **Fig. 46**, the emoji associated with the initial acquisition indicate a potential issue based on the analysis of the ECG waveform conducted by the medical device. Despite the normal HR of 75 bpm, the irregular rhythm suggests a possible concern. The medical device is programmed to perform a series of condition classifications. For instance, an HR reading above 100 bpm is classified as high, while an HR below 50 bpm is classified as low. Additionally, the device is equipped with a classification system for QRS and ST duration.

For the BP measurements illustrated in **Fig. 45**, a calibration procedure was conducted in accordance with the manufacturer's instructions using the digital sphygmomanometer Air BP, which is capable of measuring BP with an accuracy of 3 mmHg. To calibrate the device, both the cuff and the medical device were placed at heart height to initiate BP measurement with Air BP, activating the daily check function of the medical device. Subsequently, it was necessary to manually input the systolic pressure data into the medical device. This procedure was repeated two times. It should be noted that calibration is a process that differs from one patient to another and must therefore be performed at regular three-month intervals. In the absence of calibration data, non-invasive BP measurement is rendered invalid, as illustrated in the lower portion of **Fig. 46**.

Subsequently, a performance test was conducted by comparing data transmitted by the medical device to both the Android and web applications, as well as parameters set on a vital signs' simulator, the Fluke ProSim 8, which served as a

CHAPTER 6

reference point. The medical device was utilized to obtain and transmit ECG and SpO₂ data to the Android application, which subsequently relayed this information to the web application for remote storage. **Fig. 51** depicts the configuration utilized for the validation process. During the validation process, a series of simulations were conducted to assess the device's performance under various patient conditions, including normal, hypertension, hypotension, tachycardia, and bradycardia. **Table 26** presents the data utilized for the validation of the measurements acquired by the Checkme Pro, with a comparison to the data provided by Fluke ProSim 8. The Checkme Pro device has an uncertainty of 2 bpm for HR, whereas for SpO₂ it is 2% in the range 80% - 100%, and 3% in the range 70% - 79%, as indicated in reference. Therefore, the values provided by the telemedicine system are within the specified uncertainty of the reference system for SpO₂ measurements.

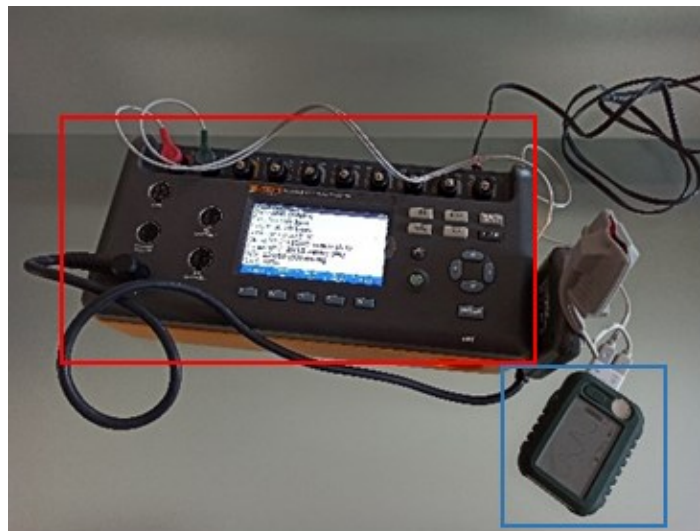


Fig. 51. Experimental setup used for validation with Fluke ProSim 8 (red box) and Checkme Pro medical device (blue box).

CHAPTER 6

Table 26. Data used to validate the measurements acquired by the medical device. Reference values are provided by Fluke ProSim 8.

Condition	Reference HR (bpm)	Acquired HR (bpm)	Reference SpO₂ (%)	Acquired SpO₂ (%)	SpO₂ Relative error (%)
Normal	60	60	97	98	1.0
Hypertension	130	130	94	96	2.1
Hypotension	40	40	95	97	2.1
Tachycardia	180	180	88	91	3.4
Bradycardia	30	30	85	89	4.7

6.4 CONCLUSION

The primary objective has been to develop a telemedicine system that enables patients and healthcare professionals to access vital parameter measurements, thereby facilitating a comprehensive assessment of the patient's health status. This system allows for the evaluation of the necessity for further examinations or treatment modifications and the observation of therapeutic outcomes.

The web application enables the presentation of data in tabular form, the insertion of inputs, and the visualization of graphs of variables of interest. This allows for the visualization of disparate data sets, as well as the daily check data associated with non-invasive measurements of vital signs, including BP, ECG, and SpO₂. A healthcare professional, including a physician, nurse, or other trained individual, can oversee the patient's health and provide necessary assistance when required.

As the use of telemedicine becomes increasingly prevalent, tools such as those can ensure continuous monitoring for patients, thereby enhancing their safety even in the absence of a physician. The Android app interface, enabled by Bluetooth connectivity, facilitates straightforward and intuitive data transfer,

CHAPTER 6

displaying all information associated with measurements made by the medical device. Additionally, the ability to navigate between screens and send data to a database enables users to display them on the web app. Furthermore, the web app allows for graphical visualization of trends in variables of interest over time. This work has demonstrated the feasibility of leveraging Bluetooth connectivity in a commercial medical device, thereby overcoming its inherent limitations in data sharing capabilities and enabling its integration into a telemedicine system. Another limitation that can be addressed by the proposed system is the fact that data are analyzed by the medical device using fixed thresholds and parameters that are not subject to control and, in particular, do not take into account the age of the patient in order to evaluate the HR condition. Therefore, a potential future development could be the management of data to enable the classification of HR using age-dependent thresholds.

A noteworthy attribute is the potential for leveraging the daily assessment functionality of the medical device and the proposed telemedicine solution to obtain BP readings in a non-invasive manner. This is particularly crucial in identifying hypertension, as accurate BP measurement is a key diagnostic indicator. This approach obviates the necessity for a sphygmomanometer, not only for the initial calibration, given the requisite positioning and potential discomfort during measurement. The deployment of the developed telemedicine system will facilitate the aggregation of data from multiple patients, thereby enabling the assessment of the accuracy of the non-invasive BP measurement technique. This technique has demonstrated to be highly accurate, and it has the potential to confer significant benefits in terms of health and economic outcomes [39].

*ECG WAVE SEGMENTATION FOR AN AUTOMATIC ANALYSIS*⁶

INTRODUCTION

CVDs affect a significant proportion of the population in developing countries, resulting in a considerable burden of morbidity and mortality. CVD encompasses a range of conditions that can affect the heart or blood vessels. Atherosclerosis, for instance, is a disease that can lead to several cardiovascular issues, including myocardial infarction and stroke. Additionally, it can cause arrhythmia and affect the function of the heart valves [152]. It is therefore of the utmost importance to detect these CVDs at the earliest possible stage. A highly effective method for predicting and diagnosing CVDs is ECG. An ECG is the primary diagnostic tool for recording the electrical activity of the heart. The analysis of key segments of this vital sign is the most common method for identifying cardiac pathologies affecting the heart. Additionally, it is a non-invasive, cost-effective, and safe procedure. From this perspective, the proliferation of wearable [153], [154] and wireless devices [155], [156], which can be utilized for specific tasks in telemedicine [1], [5], [157], [158], [159] and for patient home monitoring, represents an important advancement for the individual health improvement. These devices facilitate the monitoring of vital signs and associated parameters,

⁶ This Chapter is based on [151].

CHAPTER 7

including HR [11], [25], [160], [161], SpO₂, RR, and others.

ECG measures the electrical activity of the heart over time. This activity is caused by the action potentials that are generated and propagated in the organ during each cardiac cycle. In more detail, the electrical impulses that cause the contraction and relaxation of myocardial fibers can be measured via electrodes placed on the surface of the skin. These electrodes allow the potential difference to be recorded, and this is made possible by the conductivity of the interstitial fluids in the human body.

Once an ECG signal has been acquired, a voltage reading (measured in millivolt) is obtained as a function of time. A typical ECG signal is characterized by the following peaks: P, Q, R, S, and T, as illustrated in **Fig. 52**. These peaks represent the depolarization and repolarization of the atria and ventricles, whose impulses spread along the routes of the cardiac conduction system.

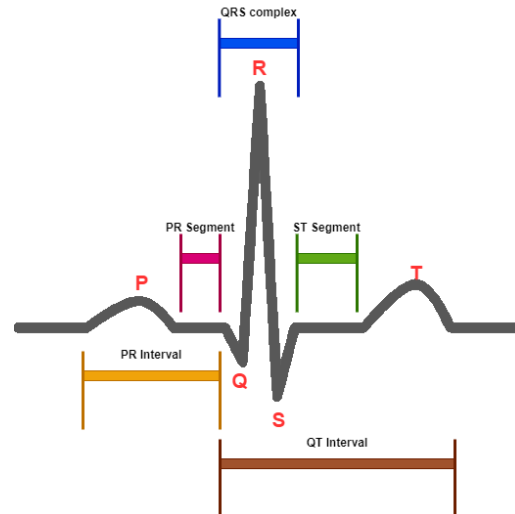


Fig. 52. ECG signal morphology of a cardiac cycle.

The QRS complex is the depolarization of both ventricles. The P wave is the result of the depolarization of the atrium. The PR segment represents the phase of the passage of the impulse to the ventricles and the beginning of the atrial diastole. The T wave represents the ventricular diastole [162], [163]. Cardiac diagnosis is based on the morphology of the ECG waves and the duration of each segment.

CHAPTER 7

The segmentation of the ECG signal is crucial for helping doctors and caregivers diagnose and monitor heart conditions.

Literature has recently proposed different methods to improve ECG wave segmentation. The automatic segmentation is challenging due to the great variability in the shape of the QRS complex between different individuals, the less marked P wave, and the various morphologies of the T wave related to the condition of the myocardium. Furthermore, there is no universal method for defining the exact positions of the characteristic points.

The most effective methods include Pan-Tompkins's algorithm [164], Short Time Fourier Transform (STFT) [165], Wavelet transform (WT) [166], [167], Empirical Mode Decomposition (EMD) and the associated Hilbert spectral analysis for nonstationary signals [168], [169], [170], [171], [172], and other algorithms as reported in [173]. Furthermore, most algorithms are based on transforming or filtering the ECG signal to highlight relevant sections and identify points of interest. Other techniques include the exploitation of CNN, SVM, and DL approaches [174], [175], [176], [177], [178].

Many proposed algorithms in literature have successfully segmented the QRS complex, but the detection of P and T waves still needs improvement. It is clear that the algorithms in literature allow the identification of peaks without indicating the beginning and end of the waves. This temporal information is useful for diagnostic purposes. This Chapter presents a new method for ECG segmentation that does not rely on artificial intelligence. It combines WT with a purpose-built algorithm to detect the QRS complex, P and T waves. The method is demonstrated by a system comprising a Data Acquisition (DAQ) device overseen by a LabVIEW Virtual Instrument and a Sparkfun one-lead heart rate monitor based on Analog Devices AD8232 amplifier. The system acquires the ECG signal and performs pre-processing, while the waves' segmentation and analysis of results are done in MATLAB R2022b.

7.1 ACQUISITION SYSTEM

The ECG signal before the amplification exhibits a relatively low amplitude, with a range on the order of mV and displays artifacts and noise. The signal may be affected by 50 Hz interference, deviation from the baseline, and the electrical activity of other muscles, which can compromise the quality of the information contained in the signal. Typically, the utilization of an operational amplifier in conjunction with an appropriate filtering mechanism is essential for the generation of a more suitable ECG signal. In this study, the ECG signal is acquired using the AD8232 single-lead heart rate monitor, which employs only three electrodes. This HR monitor is an integrated signal conditioning block that can be used for ECG and other biopotential measurement applications. It is capable of producing an ECG signal with a clearly distinguishable output, exhibiting the characteristic waves of a single cardiac cycle. Its deployment enables the extraction, amplification, and filtering of small biopotential signals in the presence of noise, such as that generated by electrode movement or remote positioning.

The HR monitor AD8232 board, illustrated in **Fig. 53**, is equipped with nine pins that facilitate its integration with any analog acquisition system. The nomenclature of the pins is as follows: SDN, LO+, LO-, OUTPUT, 3.3V, GND. Additionally, there are pins designated RA (right arm), LA (left arm), and RL (right leg) that can be connected and utilized with the user's own signal conditioning circuits. The raw ECG signal is obtained by subtracting the biopotential recorded from the RA from that recorded from the LA, with the RL serving as the reference point. This signal can be acquired from the RA, LA, and RL pins. However, it is not yet conditioned, which makes it challenging to interpret. This is because the signal is weak in amplitude and corrupted by noise.

CHAPTER 7

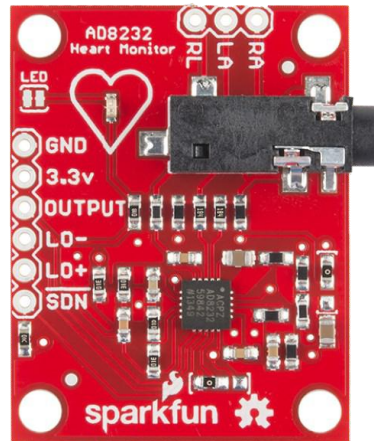


Fig. 53. AD8232 single lead heart rate monitor in a break-out board developed by Sparkfun.

In order to reduce the noise in the HR monitor output signal, it is essential that the three electrodes are correctly positioned. Accordingly, the positioning of the sensor pads is based on the Einthoven triangle, as illustrated in **Fig. 54**.

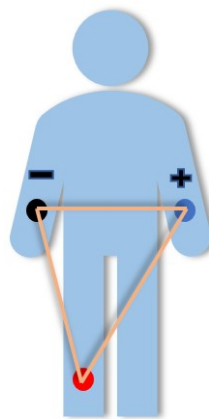


Fig. 54. Positioning of electrodes based on Einthoven triangle (black pad corresponds to the right arm, blue pad corresponds to the left arm and the red one to the right leg).

In this study, the data from the HR monitor were acquired using a DAQ board from National Instruments, and the subsequent processing was conducted using LabVIEW. **Fig. 55** depicts the experimental setup, wherein the DAQ device, the

CHAPTER 7

AD8232, and the bench power supply are illustrated. The DAQ device utilized is a NI USB 6212, which is a 16-bit board with a maximum sampling frequency of 400 kHz.

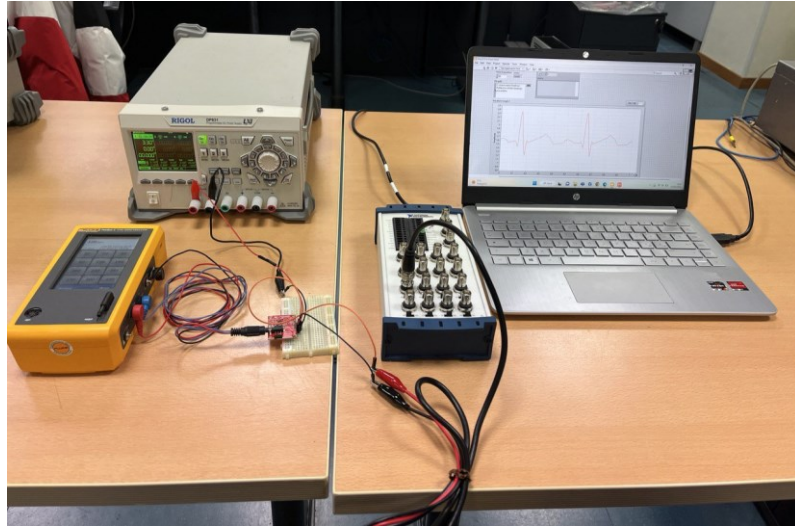


Fig. 55. Experimental setup for ECG acquisition.

7.2 ECG SEGMENTATION

An ECG is a straightforward and expeditious diagnostic tool that produces a graphical representation of the electrical impulses generated by the heart. It is a widely utilized technique for the detection of cardiac dysfunction. Indeed, the segmentation and feature extraction processes are essential for the generation of a diagnosis. This section presents a novel approach to the segmentation of QRS complexes, T waves, and P waves in ECG waveforms, with the aim of facilitating the early detection of cardiac diseases.

Despite the numerous algorithms that have been proposed and successfully demonstrated the ability to segment QRS complexes in ECG data, there remains a gap of effective detectors for P and T waves. The proposed algorithm is based on a threshold calculated using the Otsu method to detect R-peaks in the ECG waveform. Moreover, it enables the segmentation of all other ECG waves

CHAPTER 7

through the application of wavelet filters and a local maxima algorithm. The segmentation of each waveform is defined by both its onset and offset.

7.2.1 RAW SIGNAL ACQUISITION

The ECG signal was obtained using the DAQ device, with the parameters for the acquisition set by the front panel to fully utilize the ADC range. The sampling rate has been set to 200 Hz, with a maximum voltage value of +5 V and a minimum voltage value of -5 V. Prior to the analysis and extraction of the ECG signal parameters, a pre-processing step was required to detrend the signal and reduce the 50 Hz disturbance. Accordingly, LabVIEW has been employed to filter the signal using WT, with the requisite parameters duly established [179]. A threshold frequency of 0.35 and a db06 mother wavelet with a symmetric extension were employed to compute the detrend. Subsequently, wavelet denoising was performed using an undecimated WT with db06 and 8 levels. For the threshold settings, a single-level rescaling method and a universal thresholding rule with a soft threshold were employed. **Fig. 56** and **Fig. 57** illustrate the raw and processed ECG signals, respectively.

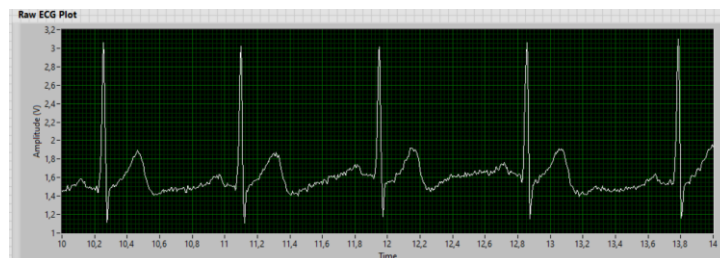


Fig. 56. Raw ECG signal.

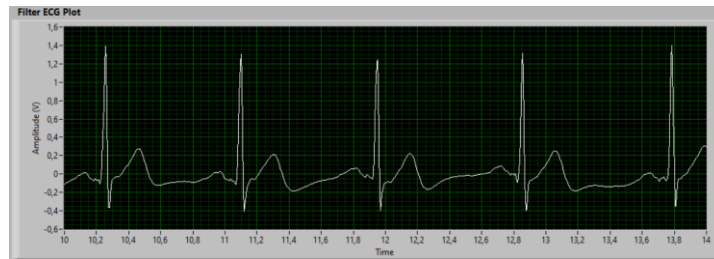


Fig. 57. Filtered ECG signal.

In this study, real ECG signals and simulations at varying HR have been obtained and analyzed. The Fluke ProSim 4 was employed for the purpose of simulating an ECG signal.

7.2.2 R-PEAK DETECTION

The proposed algorithm enables the detection of the R-peak position and amplitude in the unprocessed ECG signal, as well as the onset and offset of the QRS complex. As illustrated in Fig. 58, the R-peak position and amplitude are identified within the unprocessed ECG signal.

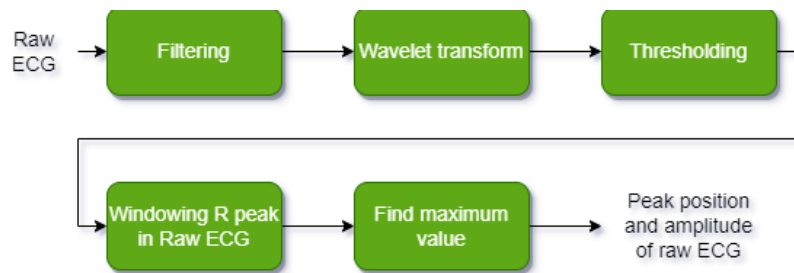


Fig. 58. R-peak detection algorithm.

Following the aforementioned signal processing, an undecimated WT with db02 as the mother wavelet, a multiple levels rescaling method with 10 levels, and a universal thresholding rule with a soft threshold have been applied. This step is essential for the purpose of mitigating P and T waves from each cardiac cycle, thereby leaving only the QRS complex for each cardiac cycle. The resulting signal after WT is illustrated in Fig. 59.

CHAPTER 7

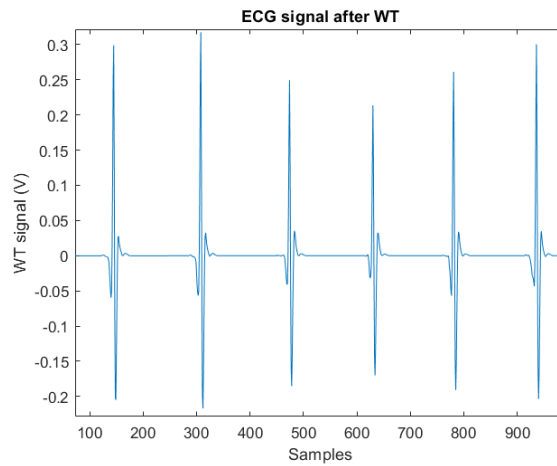


Fig. 59. ECG signal after WT.

Secondly, an image processing technique [180] has been employed to detect R-peaks using a threshold value derived from Otsu's method [181], a non-parametric and unsupervised approach to automatic threshold selection based on the histogram. By applying the aforementioned threshold to the wavelet-filtered signal, each R-peak is identified within a window, which is represented as a square signal in **Fig. 60**.

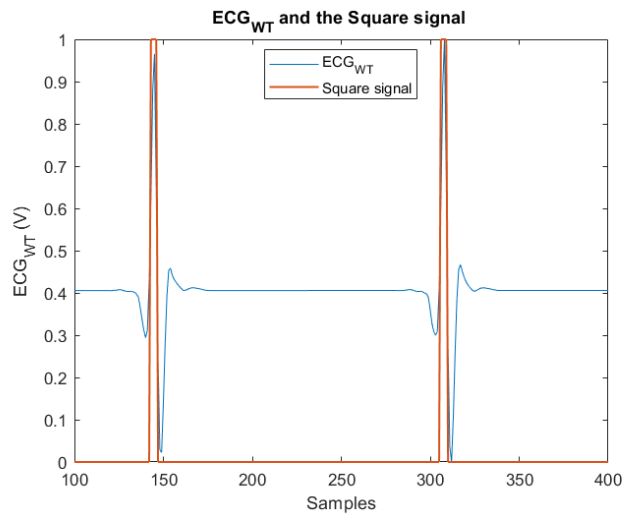


Fig. 60. ECG signal after WT transform (blue) and square signal (red).

Subsequently, the maximum value of the raw ECG signal is identified, which corresponds to the R-peak as illustrated in **Fig. 61**.

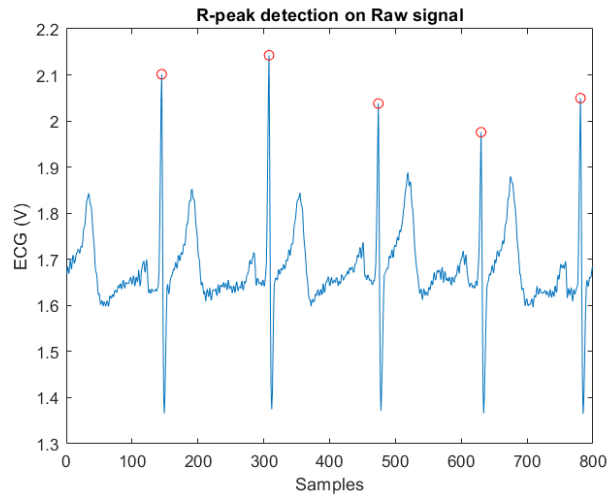


Fig. 61. R-peak detection on Raw ECG signal.

After having determined R-peak position, the mean HR can be computed, evaluating the mean time of R-R segments:

$$HR = \frac{\text{mean}(R - R)}{60}$$

7.2.3 QRS ONSET AND OFFSET DETECTION

In order to ascertain the onset and offset of the QRS complex, the STD of the wavelet-filtered signal is calculated over a sliding window comprising 5 elements, including the centered sample. The window is constructed with 5 elements backward in the sequence (k_a), 5 elements forward (k_b), and the centered sample. The length of this window is empirically determined based on the sample frequency utilized to acquire the ECG signal. For a sample frequency of 100 Hz, the optimal values for both k_a and k_b are 1. The resulting signal is illustrated in **Fig. 62**.

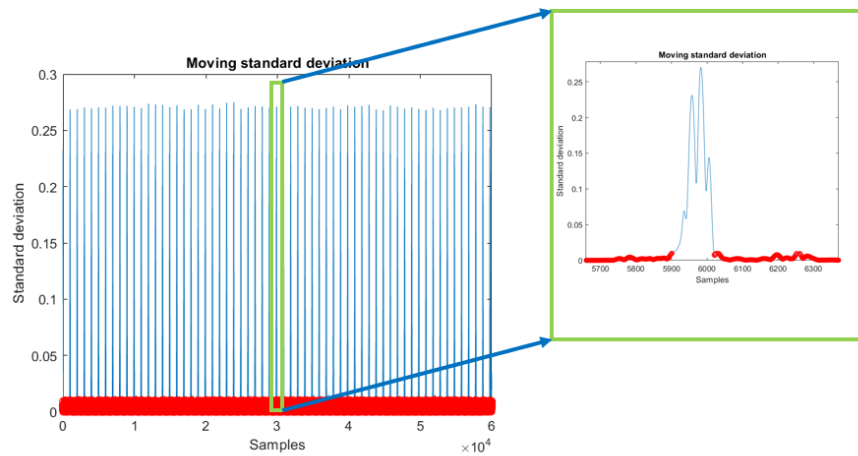


Fig. 62. Standard deviation of sliding window (blue) and zeros detected from zero-crossing algorithm.

Subsequently, the zero-crossing algorithm is employed to identify the onset and offset of the QRS complex. The onset is defined as the final zero value of the STD on the left of the i -th R-peak, while the offset is defined as the initial zero value of the STD signal on the right of the i -th R-peak.

In order to identify the Q wave, it is necessary to determine the minimum value within the onset of the QRS complex and the time elapsed between the R-peak and the onset. Similarly, the S wave is obtained by identifying the minimum between the R-peak and the offset of the QRS complex.

The segmentation of the QRS complex based on this algorithm is illustrated in **Fig. 63.**

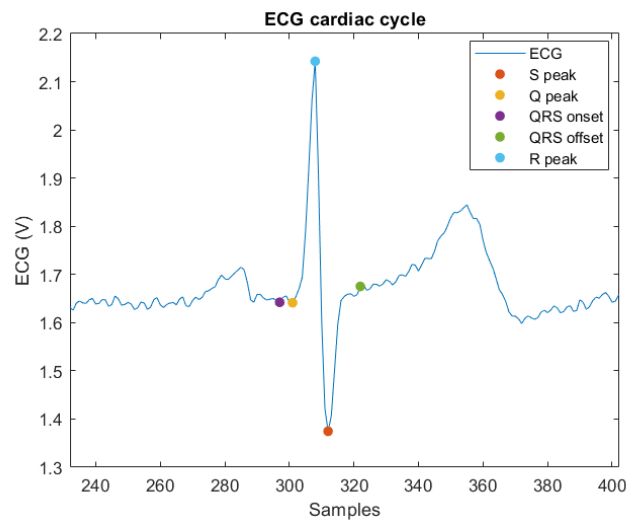


Fig. 63. QRS complex segmentation.

7.2.4 P WAVE SEGMENTATION

The detection of the P wave is of critical importance due to its relatively small amplitude in comparison to that of the R-peak. Furthermore, the visibility of the P wave is often compromised due to the interference of noise at its onset and offset.

Accordingly, the algorithm illustrated in Fig. 64 is proposed.

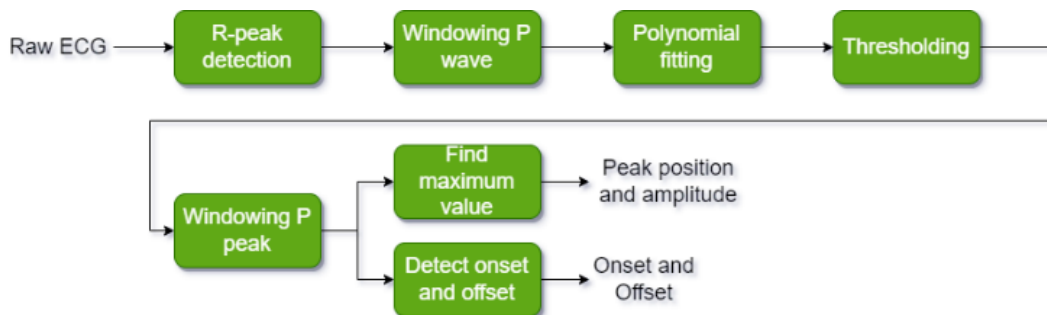


Fig. 64. P wave and T wave detection algorithms.

Following the identification of R-peaks, a windowing technique was applied to the signal for each peak (except for the first and last, in order to avoid uncompleted cycles). This defined a signal portion, beginning at the onset of each ECG cardiac cycle and extending to the corresponding QRS onset, which

CHAPTER 7

included the P wave. A fourth-degree polynomial fitting was performed on the aforementioned signal portion, which was then subjected to Otsu's method thresholding. The maximum value within this window has been designated as the P-peak, and the edges of the window have been identified as the onset and offset of the P wave, as illustrated in **Fig. 65**.

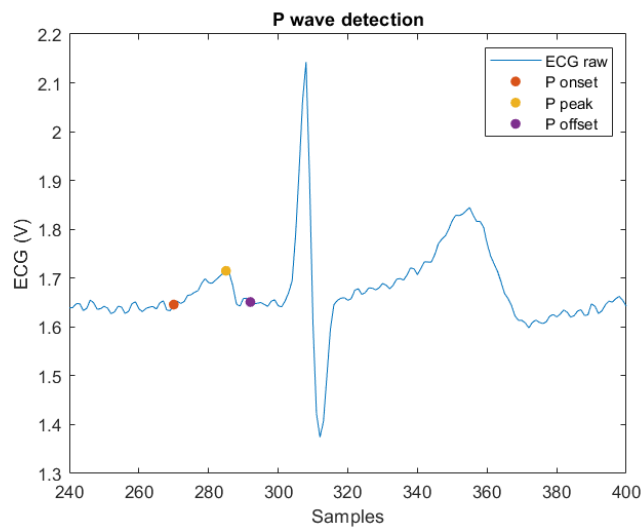


Fig. 65. P wave segmentation.

7.2.5 T WAVE SEGMENTATION

The detection of the T wave presents a significant challenge due to its smaller size in comparison to the R-peak, coupled with the presence of noise that obscures the boundaries. Furthermore, the lack of universal detection rules presents a challenge in the detection of both the T wave and the P wave. Consequently, researchers have concentrated their efforts on defining automatic detection algorithms.

In this Chapter, the same approach previously utilized for P-wave detection is employed for T-wave detection.

Indeed, a windowing technique has been applied to the ECG signal from the corresponding QRS offset to the end of the cardiac cycle for each R-peak. Subsequently, a fourth-degree polynomial fitting and Otsu's thresholding have

CHAPTER 7

been employed. The T-peak has been defined as the maximum value within the aforementioned window, and the boundaries have been defined as the two edges, as illustrated in **Fig. 66**.

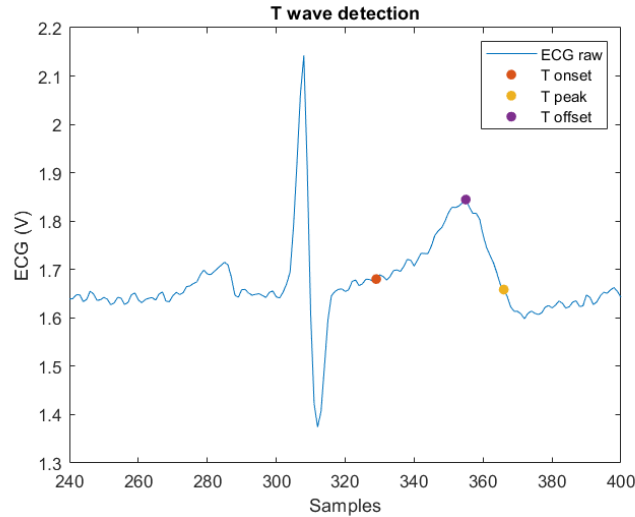


Fig. 66. T wave segmentation.

7.3 RESULTS

The proposed algorithm was applied to 100 cardiac cycles of three different patients, whose ECG signals were acquired using the system developed in this work. The following results were obtained. **Fig. 67** provides a more detailed illustration of the number of points of interest detected by the algorithm for the P wave, T wave, and QRS complex in all the recorded data acquired by the single-lead HR monitor. As illustrated in the **Fig. 67**, the QRS complex is consistently identified, along with the T and P peaks. Conversely, the accuracy of the onset and offset detection of these two waves exhibits a decline.

CHAPTER 7

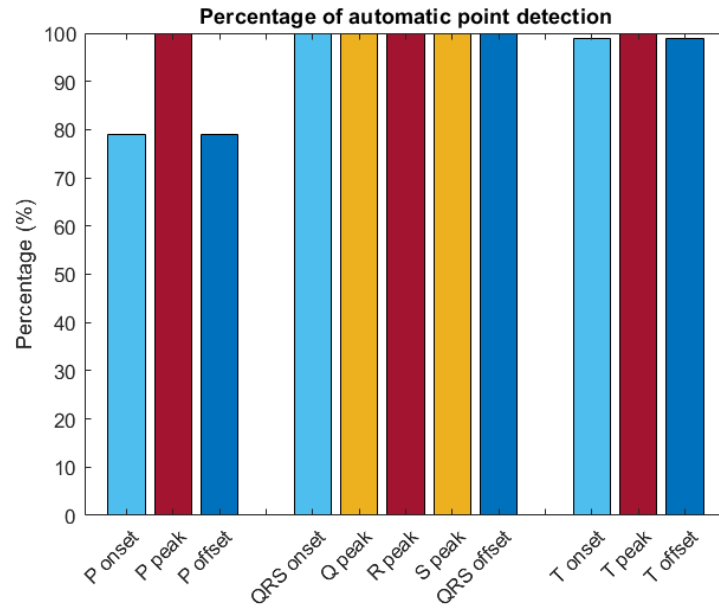


Fig. 67. Percentage of detection.

Table 27 presents the mean time error and the STD for all points of interest within the ECG waveform. The discrepancies between the locations of points identified by the proposed algorithm and those marked by handcrafted annotations were calculated to obtain the aforementioned errors.

Table 27. Mean time error and standard deviation for each ECG wave, onsets, and offsets.

	Mean (s)	STD (s)
P onset	-0.045	0.052
P peak	0.000	0.053
P offset	0.000	0.012
QRS onset	-0.010	0.012
Q peak	0.000	0.002
R peak	0.000	0.001
S peak	0.000	0.000
QRS offset	0.015	0.011
T onset	-0.002	0.014
T peak	0.005	0.001
T offset	-0.010	0.011

Furthermore, **Fig. 68** illustrates the IOU (intersection over union) for the P wave,

CHAPTER 7

QRS complex, and T wave. As illustrated in the figure, the maximum value is observed for the T wave, while the minimum value is observed for the P wave.

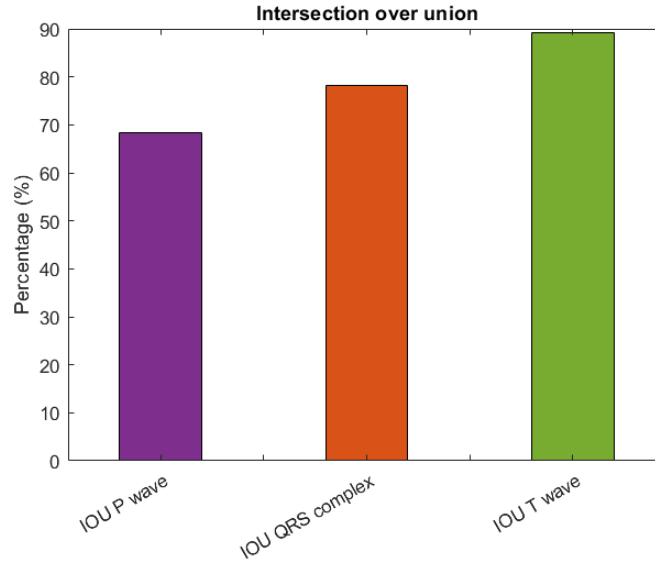


Fig. 68. IOU for all the ECG waves.

7.4 CONCLUSION

This Chapter presents a novel approach for ECG segmentation based on WT combined with Otsu's method, which can be applied to ECG signals acquired by a single lead HR monitor.

Regarding the acquired records, the algorithm enables the detection of R-peaks with a score of 100%, thereby facilitating the precise determination of the heart rate. Moreover, the QRS complex of all ECG recordings with noise has been correctly segmented with a low time error. Moreover, the approach enables the detection of P and T waves, which are more challenging to segment. This remains an unresolved issue in the literature.

CONCLUSION

In this thesis accurate BP measurement methods from PPG signals using ML and DL techniques have been proposed. To achieve this objective, it was necessary to analyze the PPG signal and the ABP signal and identify the characteristics points useful for BP estimation. To this end, an enhancement technique using the wavelet was proposed to improve the PPG signal and facilitate the extraction of features useful for training ML models. The utilization of the wavelet, in conjunction with the extraction of novel features, has been demonstrated to be advantageous. This is evidenced by the fact that, when employing three distinct feature selection algorithms, these features were identified as being among the most significant, and also by the high accuracy of the results obtained. A comprehensive discussion and analysis of these findings has been presented in **Chapter 1**. Following the identification of the significant feature set, **Chapter 2** has been dedicated to training ML models, namely XGBoost and NN, to estimate systolic and diastolic pressure values. This Chapter has presented improvements over existing literature using the XGBoost model and the selected significant features, which were identified using the MRMR selection algorithm. A further analysis has been therefore carried out in **Chapter 3** to investigate the results obtained using different feature selection methods and feature sets, including or excluding the new features introduced in **Chapter 1**. A comparison of various ML models was also conducted to determine the optimal trade-off between training time and results. The size of the dataset was also taken into account. Then the objective of **Chapter 4** has been to examine the utilization of DL models

CONCLUSION

for the estimation of the ABP signal from the PPG signal, rather than from the features. This Chapter has presented an analysis of the performance of several DL models, with a focus on the impact of varying datasets, input signal duration, model input, and the use of different loss functions. Since the final aim of this thesis was to develop a telemedicine solution that incorporates a wearable device for the acquisition of PPG signals and the estimation of BP, **Chapter 5** has outlined the preliminary prototype that has been developed for this purpose. In the final Chapters, **Chapter 6** and **Chapter 7**, some potential telemedicine solutions for other biomedical applications have been put forward for consideration.

All the aspects analyzed in this thesis could be integrated into a comprehensive system to improve patient health by monitoring not only BP but also other vital signs.

APPENDIX A

Table A1 below defines the more relevant features calculated on PPG signals, which are in the set of selected features shown in **Chapter 1**. They are grouped by domain (e.g. energy, width-related, amplitude related, ...) and they are noted as: (*) calculated on x_{FILT} (i.e. before MODWT enhancement), (°) calculated on x_{MODWT} (i.e. after MODWT enhancement), (-) calculated on the normalized signal x_{NORM} , (+) new feature and (#) already known feature.

In the table the following notation has been used: f_s is signal sampling frequency; $\mathbf{x} = [x_1, \dots, x_i, \dots, x_N]$ is the sampled PPG pulse signal of length N , with $i = 1, \dots, N$; $MODWT\{\mathbf{x}\}_{lk}$ is the MODWT wavelet coefficient up to scale 2^L , with $L = \lfloor \log_2 N \rfloor$, calculated at scale 2^l , with $l = 1, \dots, L$ and location k , with $k = 1, \dots, N$; X is the PPG chunk.

Table A1. Features.

Symbol	Definition	Notes				
Energy-related features						
$sigN2$	Squared signal Energy $sigN2 = \sum_{i=1}^N x_i ^2$	*				+
$wtN2$	Squared signal energy obtained from summing the wavelet coefficients over all levels $wtN2 = \sum_{l=1}^L \sum_{k=1}^N MODWT\{\mathbf{x}\}_{lk} ^2$			°		+
Width-related features						
w	Width of the pulse	*	°			#

APPENDIX A

	$w = \frac{N}{f_s}$					
<i>diaw33</i>	Width from DP to the subsequent intersection of x with level $0.33 \times ASP$	*				#
<i>diaw50</i>	Width from DP to the subsequent intersection of x with level $0.50 \times ASP$	*				#
<i>diaw66</i>	Width from DP to the subsequent intersection of x with level $0.66 \times ASP$	*				#
<i>diaw75</i>	Width from DP to the subsequent intersection of x with level $0.75 \times ASP$	*				#
<i>sysw33</i>	Width from intersection of x with level $0.33 \times ASP$ to SP	*				#
Amplitude-related features						
<i>ASP</i>	Amplitude of the systolic peak of x	*	o			#
<i>ADP</i>	Amplitude of the diastolic peak of x	*	o	-		#
<i>ADN</i>	Amplitude of the dicrotic notch of x	*	o	-		#
<i>RP</i>	$RP = \frac{ADP}{ASP}$ also known as the augmentation index		o			#
<i>D1</i>	$D1 = ASP - ADN$		o		+	
<i>D2</i>	$D2 = ADP - ADN$		o		+	
<i>RD</i>	$RD = \frac{D1}{D2}$		o		+	
<i>AMS</i>	Amplitude of the max slope point (MSP) of x	*		-		#
$\frac{ADN}{ASP}$	Ratio between <i>ADN</i> and <i>ASP</i> of x	*				#
Time-related features						
<i>TP</i>	Time interval from DP to the SP of x	*	o			#
<i>TSP</i>	Time interval from x_1 to the SP of x	*	o			#
<i>TDP</i>	Time interval from x_1 to the DP of x	*	o			#
<i>TDN</i>	Time interval from x_1 to the DN of x	*	o			#
<i>TIP</i>	Time interval from x_1 to the IP of x	*				#
<i>T1</i>	Time interval from the DN to the SP of x		o		+	
<i>T2</i>	Time interval from the DP to the DN of x		o		+	
<i>p2pi</i>	The peak-to-peak interval is the distance between SP_{i+1} and SP_i	*				#
Mean of $\frac{TP}{p2pi}$	Mean of ratio between <i>TP</i> and <i>p2pi</i> of x	*				#
Mean of $\frac{TDN}{p2pi}$	Mean of ratio between <i>TDN</i> and <i>p2pi</i> of x	*				#
$\frac{1}{TDN - TSP}$	Reciprocal of difference between <i>TDN</i> and <i>TSP</i> of x	*				#
$\frac{1}{TIP - TSP}$	Reciprocal of difference between time interval of IP (<i>TIP</i>) and <i>TSP</i> of x	*				#
$\frac{ADP}{PI - TDN}$	The ratio of <i>ADP</i> to the differences	*				#

APPENDIX A

	between pulse interval (PI) and TDN of x					
$\frac{1}{TP}$	Stiffness of the large arteries: the inverse of TP of PPG pulse	*				#
$\frac{ADN}{PI - TDN}$	The ratio of AND to the differences between PI and TDN of x	*				#
$\frac{TDP}{p2pi}$	Ratio of TDP and $p2pi$ of x	*				#
PI	Pulse interval of x is the distance between x_1 and x_N	*				#
Area-related features						
$A1$	Area under the curve from x_1 to the DN of x	*	o			#
$A2$	Area under the curve from DN to x_N	*	o			#
RA	$RA = \frac{A2}{A1}$		o		+	
<i>Area from x_1 to MSP</i>	Area under the curve from x_1 to MSP of x	*				#
<i>Area from IP to DP</i>	Area under the curve from IP to DP of x	*				#
<i>Area from DP to x_N</i>	Area under the curve from DP to x_N of x	*				#
Statistic features						
<i>Mean</i>	Mean of x $\mu = \frac{\sum_{i=1}^N x_i}{N}$	*	o	-		#
<i>STD</i>	Standard deviation of x $\sigma = \sqrt{\frac{\sum_{i=1}^N (x_i - \mu)^2}{N - 1}}$	*	o	-		#
<i>75 - per</i>	75-th percentile of x	*				#
<i>IQR</i>	Inter Quartile Range of x $IQR = Q_3 - Q_1$ where Q_3 is the third quartile and Q_1 is the first quartile	*				#
<i>Mean of PPG before standardization</i>	Mean of PPG signal before standardization	*				#
<i>STD of PPG before standardization</i>	STD of PPG signal before standardization	*				#
<i>Sk</i>	Skewness of x $Sk = \frac{\sum_{i=1}^N (x_i - \mu)^3}{N \sigma^3}$	*				#
Time domain features						
<i>RMS</i>	Root mean square $RMS = \sqrt{\frac{\sum_{i=1}^N x_i ^2}{N}}$	*	o	-	+	
<i>SF</i>	Shape factor of pulse $SF = \frac{RMS}{MAV}$ where MAV is the mean absolute value	*	o	-	+	

APPENDIX A

	$MAV = \frac{\sum_{i=1}^N x_i }{N}$				
<i>SNR</i>	Signal to noise ratio $SNR = \frac{P_x}{P_n}$ where P_x is the power of \mathbf{x} and P_n is the power of noise	*	o		+
<i>THD</i>	Total harmonic distortion $THD = \sqrt{\sum_{j=2}^{n_h} \frac{h_j}{h_1}} \times 100$ where h_1 is the power at the fundamental frequency, h_j is the power at the j -th harmonic component, and n_h is the number of components	*	o		+
<i>SINAD</i>	Signal to noise and distortion ratio in decibels $SINAD = 20 \log \frac{P_x}{(P_n + P_d)}$ where P_d is the power of distortion	*	o		+
<i>CrF</i>	Crest factor: $CrF = \frac{ASP}{RMS}$	*	o		+
<i>ClF</i>	Clearance factor: $ClF = \frac{ASP}{\left(\frac{\sum_{i=1}^N \sqrt{ x_i }}{N}\right)^2}$	*	o	-	+
<i>IF</i>	Impulse factor: that is the ratio between ASP and MAA $IF = \frac{ASP}{MAA}$ where MAA is the mean of the absolute amplitude	*	o	-	+
Frequency domain features					
<i>MeaF</i>	Mean frequency of the power spectrum of \mathbf{x}	*	o		+
<i>MedF</i>	Median frequency of the power spectrum of \mathbf{x}	*	o		+
<i>AP</i>	Average band power of \mathbf{x}	*	o		+
<i>OB</i>	Occupied bandwidth at 99% of \mathbf{x}	*	o		+
<i>HB</i>	Half-power bandwidth at 3 dB of \mathbf{x}	*	o		+
<i>PSA</i>	Peak spectral amplitude of \mathbf{x}	*	o		+
<i>SPL</i>	Spectral peak location of \mathbf{x}	*	o		+
Features related to the first and second derivative					
<i>a1</i>	The first maximum peak from the first derivative of \mathbf{x}	*			#

APPENDIX A

a_2	The first maximum peak from the second derivative of x after a_1	*				#
b_1	The first minimum peak from the first derivative of x after the a_1 occurred	*				#
b_2	The first minimum peak from the second derivative of x after a_2	*				#
ta_1	The time interval from x_1 to the time at which a_1 occurred of x	*				#
ta_2	The time interval from x_1 to the time at which a_2 occurred of x	*				#
tb_1	The time interval from x_1 to the time at which b_1 occurred	*				#
tb_2	The time interval from x_1 to the time at which b_2 occurred	*				#
Mean of tb_1	Mean of the time intervals from x_1 to the time at which b_1 occurred	*				#
Mean of tb_2	Mean of the time intervals from x_1 to the time at which b_2 occurred	*				#
Mean of $\frac{tb_1 - tb_2}{p2\pi}$	Mean of the ratios of difference between tb_1 and tb_2 and $p2\pi$	*				#
Mean of $\frac{tb_1}{p2\pi}$	Mean of ratio between tb_1 and $p2\pi$ of x	*				#
Mean of $\frac{tb_2}{p2\pi}$	Mean of ratio between tb_2 and $p2\pi$ of x	*				#
Mean of $\frac{ta_1}{p2\pi}$	Mean of ratio between ta_1 and $p2\pi$ of x	*				#
Mean of $\frac{b_1}{a_1}$	Mean of the ratio between b_1 and a_1 of x	*				#
Mean of ta_2	Mean of ta_2 of x	*				#
Mean of a_2	Mean of a_2 of x	*				#
Mean of $\frac{ta_2}{p2\pi}$	Mean of ratio between ta_2 and $p2\pi$ of x	*				#
FFT features						
Area from 2 to 5	Area under the curve from 2 Hz to 5 Hz for the FFT of X	*				#
Peak1	The amplitude of the first peak from the FFT of X	*				#
Freq1	The frequency at which the first peak from the FFT of X occurred	*				#
Freq2	The frequency at second peak from the FFT of X	*				#
Area from 0 to 2	Area under the curve from 0 Hz to 2 Hz for the FFT of X	*				#
$\frac{Freq1}{Freq3}$	The ratio of $Freq1$ to the frequency at third peak from the FFT ($Freq3$) of X	*				#

APPENDIX A

$\frac{Freq1}{Freq2}$	The ratio of <i>Freq1</i> to the frequency at second peak from the FFT (<i>Freq2</i>) of <i>X</i>	*				#
<i>Fmax</i>	The value of highest frequency in the spectrum of <i>X</i>	*				#
$\frac{Area\ from\ 0\ to\ 2}{Area\ from\ 2\ to\ 5}$	Ratio between <i>Area from 0 to 2</i> and <i>Area from 2 to 5</i>	*				#
Non-linear functions of features						
<i>Logarithm IP</i>	Logarithm of location of IP (<i>LIP</i>) of <i>x</i> <i>Logarithm IP = ln LIP</i>	*				#
<i>Logarithm of DN</i>	Logarithm of location of DN (<i>LDN</i>) of <i>x</i> <i>Logarithm DN = ln LDN</i>	*				#

REFERENCES

- [1] F. Attivissimo, L. De Palma, A. Di Nisio, M. Scarpetta, and A. M. L. Lanzolla, "Photoplethysmography Signal Wavelet Enhancement and Novel Features Selection for Non-Invasive Cuff-Less Blood Pressure Monitoring," *Sensors*, vol. 23, no. 4, Art. no. 4, Jan. 2023, doi: 10.3390/s23042321.
- [2] F. Attivissimo, V. I. D'Alessandro, L. De Palma, A. M. L. Lanzolla, and A. Di Nisio, "Non-Invasive Blood Pressure Sensing via Machine Learning," *Sensors*, vol. 23, no. 19, p. 8342, Oct. 2023, doi: 10.3390/s23198342.
- [3] Y. Fan, P. Xu, H. Jin, J. Ma, and L. Qin, "Vital sign measurement in telemedicine rehabilitation based on intelligent wearable medical devices," *IEEE Access*, vol. 7, pp. 54819–54823, 2019, doi: 10.1109/ACCESS.2019.2913189.
- [4] C. Pintavirooj, T. Keatsamarn, and T. Treebupachatsakul, "Multi-parameter vital sign telemedicine system using web socket for covid-19 pandemics," *Healthc. Switz.*, vol. 9, no. 3, 2021, doi: 10.3390/healthcare9030285.
- [5] L. De Palma, F. Attivissimo, A. Di Nisio, A. M. L. Lanzolla, M. A. Ragolia, and M. Spadavecchia, "Development of a web-based system for interfacing a portable Bluetooth vital sign monitor," in *2022 IEEE International Symposium on Medical Measurements and Applications, MeMeA 2022 - Conference Proceedings*, 2022. doi: 10.1109/MeMeA54994.2022.9856526.
- [6] B. G. Celler and R. S. Sparks, "Home telemonitoring of vital signs - Technical challenges and future directions," *IEEE J. Biomed. Health Inform.*, vol. 19, no. 1, pp. 82–91, 2015, doi: 10.1109/JBHI.2014.2351413.
- [7] X.-F. Teng *et al.*, "Wearable Medical Systems for p-Health," *IEEE Rev. Biomed. Eng.*, vol. 1, pp. 62–74, 2008, doi: 10.1109/RBME.2008.2008248.
- [8] P. Arpaia *et al.*, "Conceptual design of a machine learning-based wearable soft sensor for non-invasive cardiovascular risk assessment," *Meas. J. Int. Meas. Confed.*, vol. 169, 2021, doi: 10.1016/j.measurement.2020.108551.
- [9] D. Shao, Y. Yang, C. Liu, F. Tsow, H. Yu, and N. Tao, "Noncontact monitoring breathing pattern, exhalation flow rate and pulse transit time," *IEEE Trans. Biomed. Eng.*, vol. 61, no. 11, pp. 2760–2767, 2014, doi: 10.1109/TBME.2014.2327024.
- [10] P. Arpaia, N. Moccaldi, R. Prevete, I. Sannino, and A. Tedesco, "A Wearable EEG Instrument for Real-Time Frontal Asymmetry Monitoring in Worker Stress Analysis," *IEEE Trans. Instrum. Meas.*, vol. 69, no. 10, pp. 8335–8343, 2020, doi: 10.1109/TIM.2020.2988744.
- [11] M. Scarpetta, M. Spadavecchia, G. Andria, M. A. Ragolia, and N. Giaquinto, "Accurate simultaneous measurement of heartbeat and respiratory intervals using a smartphone," *J. Instrum.*, vol. 17, no. 07, p. P07020, Jul. 2022, doi: 10.1088/1748-0221/17/07/P07020.
- [12] R. C. Block *et al.*, "Conventional pulse transit times as markers of blood pressure changes in humans," *Sci. Rep.*, vol. 10, no. 1, 2020, doi: 10.1038/s41598-020-73143-8.

REFERENCES

- [13] J. C. Bramwell and A. V. Hill, "The velocity of the pulse wave in man," *Proc R Soc Lond B Biol Sci*, vol. 93, no. 652, pp. 298–306, 1922.
- [14] L. A. Geddes, M. H. Voelz, C. F. Babbs, J. D. Bourland, and W. A. Tacker, "Pulse Transit Time as an Indicator of Arterial Blood Pressure," *Psychophysiology*, vol. 18, no. 1, pp. 71–74, 1981, doi: 10.1111/j.1469-8986.1981.tb01545.x.
- [15] M. Elgendi *et al.*, "The use of photoplethysmography for assessing hypertension," *Npj Digit. Med.*, vol. 2, no. 1, 2019, doi: 10.1038/s41746-019-0136-7.
- [16] G. Slapni Č Ar, N. Mlakar, and M. Luštrek, "Blood pressure estimation from photoplethysmogram using a spectro-temporal deep neural network," *Sens. Switz.*, vol. 19, no. 15, 2019, doi: 10.3390/s19153420.
- [17] L. N. Harfiya, C.-C. Chang, and Y.-H. Li, "Continuous blood pressure estimation using exclusively photoplethysmography by lstm-based signal-to-signal translation," *Sensors*, vol. 21, no. 9, 2021, doi: 10.3390/s21092952.
- [18] M. Kachuee, M. M. Kiani, H. Mohammadzade, and M. Shabany, "Cuff-less high-accuracy calibration-free blood pressure estimation using pulse transit time," in *Proceedings - IEEE International Symposium on Circuits and Systems*, 2015, pp. 1006–1009. doi: 10.1109/ISCAS.2015.7168806.
- [19] M. H. Chowdhury *et al.*, "Estimating blood pressure from the photoplethysmogram signal and demographic features using machine learning techniques," *Sens. Switz.*, vol. 20, no. 11, 2020, doi: 10.3390/s20113127.
- [20] H. Tjahjadi and K. Ramli, "Noninvasive blood pressure classification based on photoplethysmography using K-nearest neighbors algorithm: A feasibility study," *Inf. Switz.*, vol. 11, no. 2, 2020, doi: 10.3390/info11020093.
- [21] N. Hasanzadeh, M. M. Ahmadi, and H. Mohammadzade, "Blood Pressure Estimation Using Photoplethysmogram Signal and Its Morphological Features," *IEEE Sens. J.*, vol. 20, no. 8, pp. 4300–4310, 2020, doi: 10.1109/JSEN.2019.2961411.
- [22] Y.-C. Hsu, Y.-H. Li, C.-C. Chang, and L. N. Harfiya, "Generalized deep neural network model for cuffless blood pressure estimation with photoplethysmogram signal only," *Sens. Switz.*, vol. 20, no. 19, pp. 1–18, 2020, doi: 10.3390/s20195668.
- [23] Y. Kurylyak, F. Lamonaca, and D. Grimaldi, "A Neural Network-based method for continuous blood pressure estimation from a PPG signal," in *Conference Record - IEEE Instrumentation and Measurement Technology Conference*, 2013, pp. 280–283. doi: 10.1109/I2MTC.2013.6555424.
- [24] Q. Qananwah, A. Dagamseh, H. Alquran, K. S. Ibrahim, M. Alodat, and O. Hayden, "A comparative study of photoplethysmogram and piezoelectric plethysmogram signals," *Phys. Eng. Sci. Med.*, vol. 43, no. 4, pp. 1207–1217, Dec. 2020, doi: 10.1007/s13246-020-00923-x.
- [25] L. De Palma, M. Scarpetta, and M. Spadavecchia, "Characterization of Heart Rate Estimation Using Piezoelectric Plethysmography in Time- and Frequency-domain," in *IEEE Medical Measurements and Applications, MeMeA 2020 - Conference Proceedings*, 2020. doi: 10.1109/MeMeA49120.2020.9137226.
- [26] D. Castaneda, A. Esparza, M. Ghamari, C. Soltanpur, and H. Nazeran, "A review on wearable photoplethysmography sensors and their potential future applications in health care," *Int J Biosens Bioelectron*, vol. 4, no. 4, pp. 195–202, 2018.
- [27] T. Tamura, Y. Maeda, M. Sekine, and M. Yoshida, "Wearable photoplethysmographic sensors—past and present," *Electronics*, vol. 3, no. 2, pp.

REFERENCES

- 282–302, 2014, doi: 10.3390/electronics3020282.
- [28] D. Nachman *et al.*, “Comparing blood pressure measurements between a photoplethysmography-based and a standard cuff-based manometry device,” *Sci. Rep.*, vol. 10, no. 1, 2020, doi: 10.1038/s41598-020-73172-3.
- [29] B. Moody, G. Moody, M. Villarroel, G. Clifford, and I. Silva, “MIMIC-III Waveform Database Matched Subset,” *PhysioNet*, 2020.
- [30] A. E. W. Johnson *et al.*, “MIMIC-III, a freely accessible critical care database,” *Sci. Data*, vol. 3, 2016, doi: 10.1038/sdata.2016.35.
- [31] A. L. Goldberger *et al.*, “PhysioBank, PhysioToolkit, and PhysioNet: components of a new research resource for complex physiologic signals,” *Circulation*, vol. 101, no. 23, pp. E215–220, 2000.
- [32] I. Silva and G. Moody, “An open-source toolbox for analysing and processing physionet databases in matlab and octave,” *J Open Res Softw*, vol. 2, no. 1, 2014.
- [33] X. Xing and M. Sun, “Optical blood pressure estimation with photoplethysmography and fft-based neural networks,” *Biomed. Opt. Express*, vol. 7, no. 8, pp. 3007–3020, 2016, doi: 10.1364/BOE.7.003007.
- [34] H. Shin and S. D. Min, “Feasibility study for the non-invasive blood pressure estimation based on ppg morphology: Normotensive subject study,” *Biomed. Eng. Online*, vol. 16, no. 1, 2017, doi: 10.1186/s12938-016-0302-y.
- [35] M. Elgendi, “On the analysis of fingertip photoplethysmogram signals,” *Curr. Cardiol. Rev.*, vol. 8, no. 1, pp. 14–25, 2012, doi: 10.2174/157340312801215782.
- [36] S. G. Khalid, J. Zhang, F. Chen, and D. Zheng, “Blood Pressure Estimation Using Photoplethysmography Only: Comparison between Different Machine Learning Approaches,” *J. Healthc. Eng.*, vol. 2018, 2018, doi: 10.1155/2018/1548647.
- [37] T. Otsuka, T. Kawada, M. Katsumata, and C. Ibuki, “Utility of second derivative of the finger photoplethysmogram for the estimation of the risk of coronary heart disease in the general population,” *Circ. J.*, vol. 70, no. 3, pp. 304–310, 2006, doi: 10.1253/circj.70.304.
- [38] S. Sun *et al.*, “Finger and forehead photoplethysmography-derived pulse-pressure variation and the benefits of baseline correction,” *J. Clin. Monit. Comput.*, vol. 33, no. 1, pp. 65–75, 2019, doi: 10.1007/s10877-018-0140-5.
- [39] X. Xing, Z. Ma, M. Zhang, Y. Zhou, W. Dong, and M. Song, “An Unobtrusive and Calibration-free Blood Pressure Estimation Method using Photoplethysmography and Biometrics,” *Sci. Rep.*, vol. 9, no. 1, 2019, doi: 10.1038/s41598-019-45175-2.
- [40] W. Zong, T. Heldt, G. B. Moody, and R. G. Mark, “An open-source algorithm to detect onset of arterial blood pressure pulses,” in *Computers in Cardiology*, 2003, pp. 259–262. doi: 10.1109/cic.2003.1291140.
- [41] J. X. Sun, A. T. Reisner, and R. G. Mark, “A signal abnormality index for arterial blood pressure waveforms,” in *Computers in Cardiology*, 2006, pp. 13–16.
- [42] H. Rabbani, R. Nezafat, and S. Gazor, “Wavelet-domain medical image denoising using bivariate laplacian mixture model,” *IEEE Trans. Biomed. Eng.*, vol. 56, no. 12, pp. 2826–2837, 2009, doi: 10.1109/TBME.2009.2028876.
- [43] G. Andria, F. Attivissimo, G. Cavone, N. Giaquinto, and A. M. L. Lanzolla, “Linear filtering of 2-D wavelet coefficients for denoising ultrasound medical images,” *Meas. J. Int. Meas. Confed.*, vol. 45, no. 7, pp. 1792–1800, 2012, doi: 10.1016/j.measurement.2012.04.005.

REFERENCES

- [44] F. Adamo, G. Andria, F. Attivissimo, A. M. L. Lanzolla, and M. Spadavecchia, "A comparative study on mother wavelet selection in ultrasound image denoising," *Meas. J. Int. Meas. Confed.*, vol. 46, no. 8, pp. 2447–2456, 2013, doi: 10.1016/j.measurement.2013.04.064.
- [45] S. Gurumoorthy, N. B. Muppalaneni, and G. S. Kumari, "Eeg signal denoising using haar transform and maximal overlap discrete wavelet transform (Modwt) for the finding of epilepsy," *In*, 2020.
- [46] Z. Zhang, Q. K. Telesford, C. Giusti, K. O. Lim, and D. S. Bassett, "Choosing wavelet methods, filters, and lengths for functional brain network construction," *PLoS ONE*, vol. 11, no. 6, 2016, doi: 10.1371/journal.pone.0157243.
- [47] R. Sundarasekar *et al.*, "Internet of Things with Maximal Overlap Discrete Wavelet Transform for Remote Health Monitoring of Abnormal ECG Signals," *J. Med. Syst.*, vol. 42, no. 11, 2018, doi: 10.1007/s10916-018-1093-4.
- [48] S. C. Millasseau, R. P. Kelly, J. M. Ritter, and P. J. Chowienczyk, "Determination of age-related increases in large artery stiffness by digital pulse contour analysis," *Clin. Sci.*, vol. 103, no. 4, pp. 371–377, 2002, doi: 10.1042/cs1030371.
- [49] M. A. Hall, "Correlation-based Feature Selection for Discrete and Numeric Class Machine Learning," in *Proceedings of the Seventeenth International Conference on Machine Learning*, in ICML '00. San Francisco, CA, USA: Morgan Kaufmann Publishers Inc., Jun. 2000, pp. 359–366.
- [50] K. Kira and L. A. Rendell, "Feature selection problem: traditional methods and a new algorithm," in *Proceedings Tenth National Conference on Artificial Intelligence*, 1992, pp. 129–134.
- [51] I. Kononenko, E. Šimec, and M. Robnik-Šikonja, "Overcoming the Myopia of Inductive Learning Algorithms with RELIEFF," *Appl. Intell.*, vol. 7, no. 1, pp. 39–55, 1997, doi: 10.1023/A:1008280620621.
- [52] G. Roffo, "Ranking to Learn and Learning to Rank: On the Role of Ranking in Pattern Recognition Applications, CoRR abs/1706.05933," *Rank. Learn Learn. Rank Role Rank. Pattern Recognit. Appl.*, 2017.
- [53] C. Ding and H. Peng, "Minimum redundancy feature selection from microarray gene expression data," *J. Bioinform. Comput. Biol.*, vol. 3, no. 2, pp. 185–205, 2005, doi: 10.1142/S0219720005001004.
- [54] M. Kachuee, M. M. Kiani, H. Mohammadzade, and M. Shabany, "Cuffless Blood Pressure Estimation Algorithms for Continuous Health-Care Monitoring," *IEEE Trans. Biomed. Eng.*, vol. 64, no. 4, pp. 859–869, 2017, doi: 10.1109/TBME.2016.2580904.
- [55] A. Chakraborty, D. Goswami, J. Mukhopadhyay, and S. Chakrabarti, "Measurement of Arterial Blood Pressure through Single-Site Acquisition of Photoplethysmograph Signal," *IEEE Trans. Instrum. Meas.*, vol. 70, 2021, doi: 10.1109/TIM.2020.3011304.
- [56] Z. Li and W. He, "A continuous blood pressure estimation method using photoplethysmography by grnn-based model," *Sensors*, vol. 21, no. 21, 2021, doi: 10.3390/s21217207.
- [57] R. K. Pandey, T.-Y. Lin, and P. C.-P. Chao, "Design and implementation of a photoplethysmography acquisition system with an optimized artificial neural network for accurate blood pressure measurement," *Microsyst. Technol.*, vol. 27, no. 6, pp. 2345–2367, 2021, doi: 10.1007/s00542-020-05109-9.

REFERENCES

- [58] J. Guo *et al.*, "An XGBoost-based physical fitness evaluation model using advanced feature selection and Bayesian hyper-parameter optimization for wearable running monitoring," *Comput. Netw.*, vol. 151, pp. 166–180, 2019, doi: 10.1016/j.comnet.2019.01.026.
- [59] A. Prabha, J. Yadav, A. Rani, and V. Singh, "Intelligent estimation of blood glucose level using wristband PPG signal and physiological parameters," *Biomed. Signal Process. Control*, vol. 78, 2022, doi: 10.1016/j.bspc.2022.103876.
- [60] X. Che, M. Li, W. Kang, F. Lai, and J. Wang, "Continuous blood pressure estimation from two-channel PPG parameters by XGBoost," in *IEEE International Conference on Robotics and Biomimetics, ROBIO 2019*, 2019, pp. 2707–2712. doi: 10.1109/ROBIO49542.2019.8961600.
- [61] H. Shin, "XGBoost Regression of the Most Significant Photoplethysmogram Features for Assessing Vascular Aging," *IEEE J. Biomed. Health Inform.*, vol. 26, no. 7, pp. 3354–3361, 2022, doi: 10.1109/JBHI.2022.3151091.
- [62] L. Gao and Y. Ding, "Disease prediction via Bayesian hyperparameter optimization and ensemble learning," *BMC Res. Notes*, vol. 13, no. 1, 2020, doi: 10.1186/s13104-020-05050-0.
- [63] M. E. Gregg, T. A. Matyas, and J. E. James, "A new model of individual differences in hemodynamic profile and blood pressure reactivity," *Psychophysiology*, vol. 39, no. 1, pp. 64–72, 2002, doi: 10.1111/1469-8986.3910064.
- [64] A. Sherwood, C. A. Dolan, and K. C. Light, "Hemodynamics of Blood Pressure Responses During Active and Passive Coping," *Psychophysiology*, vol. 27, no. 6, pp. 656–668, 1990, doi: 10.1111/j.1469-8986.1990.tb03189.x.
- [65] D. DeMers and D. Wachs, "Physiology, mean arterial pressure," *StatPearls*, 2020.
- [66] J. Kim, B. Cho, S. Im, M. Jeon, I. Kim, and S. Kim, "Comparative study on artificial neural network with multiple regressions for continuous estimation of blood pressure," *Proc IEEE 27th Annu Conf Eng Med Biol*, pp. 6942–6945, 2005.
- [67] F. S. Cattivelli and H. Garudadri, "Noninvasive cuffless estimation of blood pressure from pulse arrival time and heart rate with adaptive calibration," in *Proceedings - 2009 6th International Workshop on Wearable and Implantable Body Sensor Networks, BSN 2009*, 2009, pp. 114–119. doi: 10.1109/BSN.2009.35.
- [68] Y. Zhang and Z. Feng, "A SVM method for continuous blood pressure estimation from a PPG signal," in *ACM International Conference Proceeding Series*, 2017, pp. 128–132. doi: 10.1145/3055635.3056634.
- [69] A. Soltan zadi, R. Alex, R. Zhang, D. E. Watenpaugh, and K. Behbehani, "Arterial blood pressure feature estimation using photoplethysmography," *Comput. Biol. Med.*, vol. 102, pp. 104–111, 2018, doi: 10.1016/j.combiomed.2018.09.013.
- [70] L. Wang, W. Zhou, Y. Xing, and X. Zhou, "A novel neural network model for blood pressure estimation using photoplethysmography without electrocardiogram," *J. Healthc. Eng.*, vol. 2018, 2018, doi: 10.1155/2018/7804243.
- [71] V. Fleischhauer, A. Feldheiser, and S. Zaunseder, "Beat-to-Beat Blood Pressure Estimation by Photoplethysmography and Its Interpretation," *Sensors*, vol. 22, no. 18, 2022, doi: 10.3390/s22187037.
- [72] M. Liu, L.-M. Po, and H. Fu, "Cuffless blood pressure estimation based on photoplethysmography signal and its second derivative," *Int. J. Comput. Theory Eng.*, vol. 9, no. 3, pp. 202–206, 2017.

REFERENCES

- [73]G. Zhang, S. Shin, J. Jung, M. Li, and Y. T. Kim, "Machine learning Algorithm for Non-invasive Blood Pressure Estimation Using PPG Signals," in *Proceedings - 2022 IEEE 5th International Conference on Artificial Intelligence and Knowledge Engineering, AIKE 2022*, 2022, pp. 94–97. doi: 10.1109/AIKE55402.2022.00022.
- [74]G. S. Stergiou *et al.*, "A universal standard for the validation of blood pressure measuring devices: Association for the Advancement of Medical Instrumentation/European Society of Hypertension/International Organization for Standardization (AAMI/ESH/ISO) Collaboration Statement," *Hypertension*, vol. 71, no. 3, pp. 368–374, 2018, doi: 10.1161/HYPERTENSIONAHA.117.10237.
- [75]Assoc. Adv. Med. Instrum. Am. Natl. Stand. Man. Electron. Autom. Sphygmomanometers, 2003.
- [76]E. O'Brien, B. Waeber, G. Parati, J. Staessen, and M. G. Myers, "Blood pressure measuring devices: Recommendations of the European Society of Hypertension," *Br. Med. J.*, vol. 322, no. 7285, pp. 531–536, 2001, doi: 10.1136/bmj.322.7285.531.
- [77]M. Rong and K. Li, "A multi-type features fusion neural network for blood pressure prediction based on photoplethysmography," *Biomed. Signal Process. Control*, vol. 68, 2021, doi: 10.1016/j.bspc.2021.102772.
- [78]Y.-H. Li, L. N. Harfiya, and C.-C. Chang, "Featureless Blood Pressure Estimation Based on Photoplethysmography Signal Using CNN and BiLSTM for IoT Devices," *Wirel. Commun. Mob. Comput.*, vol. 2021, 2021, doi: 10.1155/2021/9085100.
- [79]S. S. Mousavi, M. Firouzmand, M. Charmi, M. Hemmati, M. Moghadam, and Y. Ghorbani, "Blood pressure estimation from appropriate and inappropriate PPG signals using A whole-based method," *Biomed. Signal Process. Control*, vol. 47, pp. 196–206, 2019, doi: 10.1016/j.bspc.2018.08.022.
- [80]G. Mancia *et al.*, "2013 ESH/ESC guidelines for the management of arterial hypertension: The Task Force for the management of arterial hypertension of the European Society of Hypertension (ESH) and of the European Society of Cardiology (ESC)," *Eur. Heart J.*, vol. 34, no. 28, pp. 2159–2219, 2013, doi: 10.1093/eurheartj/eh151.
- [81]D. G. Altman and J. M. Bland, "Measurement in medicine: The analysis of method comparison studies," *Statistician*, vol. 32, pp. 307–317, 1983.
- [82]N. Ö. Doğan, "Bland-Altman analysis: A paradigm to understand correlation and agreement," *Turk. J. Emerg. Med.*, vol. 18, no. 4, pp. 139–141, 2018, doi: 10.1016/j.tjem.2018.09.001.
- [83]D. Giavarina, "Understanding Bland Altman analysis," *Biochem. Medica*, vol. 25, no. 2, pp. 141–151, 2015, doi: 10.11613/BM.2015.015.
- [84]A. Di Nisio, L. De Palma, M. A. Ragolia, A. M. L. Lanzolla, and F. Attivissimo, "Performance comparison of machine learning algorithms for the estimation of blood pressure using photoplethysmography," *Biomed. Signal Process. Control*, vol. 99, p. 106838, Jan. 2025, doi: 10.1016/j.bspc.2024.106838.
- [85]S. Sun *et al.*, "Systolic blood pressure estimation using ECG and PPG in patients undergoing surgery," *Biomed. Signal Process. Control*, vol. 79, p. 104040, Jan. 2023, doi: 10.1016/j.bspc.2022.104040.
- [86]F. Attivissimo, A. D. Nisio, A. M. L. Lanzolla, and M. A. Ragolia, "Analysis of Position Estimation Techniques in a Surgical EM Tracking System," *IEEE Sens. J.*, vol. 21, no. 13, pp. 14389–14396, Jul. 2021, doi: 10.1109/JSEN.2020.3042647.

REFERENCES

- [87] B. Sun, C. Wang, X. Chen, Y. Zhang, and H. Shao, "PPG signal motion artifacts correction algorithm based on feature estimation," *Optik*, vol. 176, pp. 337–349, Jan. 2019, doi: 10.1016/j.ijleo.2018.09.085.
- [88] D. Pollreisz and N. TaheriNejad, "Detection and Removal of Motion Artifacts in PPG Signals," *Mob. Netw. Appl.*, vol. 27, no. 2, pp. 728–738, Apr. 2022, doi: 10.1007/s11036-019-01323-6.
- [89] Y. Zheng, C. Wu, P. Cai, Z. Zhong, H. Huang, and Y. Jiang, "Tiny-PPG: A lightweight deep neural network for real-time detection of motion artifacts in photoplethysmogram signals on edge devices," *Internet Things*, vol. 25, p. 101007, Apr. 2024, doi: 10.1016/j.iot.2023.101007.
- [90] Y. Chen *et al.*, "A Wearable Physiological Detection System to Monitor Blink From Faint Motion Artifacts by Machine Learning Method," *IEEE Sens. J.*, vol. 23, no. 21, pp. 26126–26135, Nov. 2023, doi: 10.1109/JSEN.2023.3312975.
- [91] F. Attivissimo, V. I. D'Alessandro, A. Di Nisio, G. Scarcelli, J. Schumacher, and A. M. L. Lanzolla, "Performance evaluation of image processing algorithms for eye blinking detection," *Measurement*, vol. 223, p. 113767, Dec. 2023, doi: 10.1016/j.measurement.2023.113767.
- [92] S. González, W.-T. Hsieh, and T. P.-C. Chen, "A benchmark for machine-learning based non-invasive blood pressure estimation using photoplethysmogram," *Sci. Data*, vol. 10, no. 1, p. 149, Mar. 2023, doi: 10.1038/s41597-023-02020-6.
- [93] P. Chakraborty and C. Tharini, "Non-invasive cuff free blood pressure and heart rate measurement from photoplethysmography (PPG) signal using machine learning," *Wirel. Pers. Commun.*, vol. 134, no. 4, pp. 2485–2497, Feb. 2024, doi: 10.1007/s11277-024-11070-x.
- [94] A. Chowdhury, D. Das, A. B. M. Eldaly, R. C. C. Cheung, and M. H. Chowdhury, "Photoplethysmogram-based heart rate and blood pressure estimation with hypertension classification," *IPEM-Transl.*, vol. 9, p. 100024, Mar. 2024, doi: 10.1016/j.ipemt.2024.100024.
- [95] S. Sarkar and S. K. Pahuja, "Current Developments in Cuff-Free Non-invasive Continuous Blood Pressure Estimation Using Photoplethysmography," *Biomed. Mater. Devices*, vol. 2, no. 2, pp. 743–758, Sep. 2024, doi: 10.1007/s44174-023-00146-0.
- [96] T. Chen and C. Guestrin, "XGBoost: A Scalable Tree Boosting System," in *Proceedings of the 22nd ACM SIGKDD International Conference on Knowledge Discovery and Data Mining*, in KDD '16. New York, NY, USA: Association for Computing Machinery, Aug. 2016, pp. 785–794. doi: 10.1145/2939672.2939785.
- [97] X. Glorot and Y. Bengio, "Understanding the difficulty of training deep feedforward neural networks," in *Proceedings of the Thirteenth International Conference on Artificial Intelligence and Statistics*, JMLR Workshop and Conference Proceedings, Mar. 2010, pp. 249–256. Accessed: Aug. 01, 2024. [Online]. Available: <https://proceedings.mlr.press/v9/glorot10a.html>
- [98] J. Fox, *Regression Diagnostics: An Introduction*. SAGE Publications, 2019.
- [99] L. Breiman, J. Friedman, R. A. Olshen, and C. J. Stone, *Classification and Regression Trees*. New York: Chapman and Hall/CRC, 2017. doi: 10.1201/9781315139470.
- [100] C. Cortes and V. Vapnik, "Support-vector networks," *Mach. Learn.*, vol. 20, no. 3, pp. 273–297, Sep. 1995, doi: 10.1007/BF00994018.
- [101] C. E. Rasmussen, "Gaussian Processes in Machine Learning," in *Advanced*

REFERENCES

- Lectures on Machine Learning: ML Summer Schools 2003, Canberra, Australia, February 2 - 14, 2003, Tübingen, Germany, August 4 - 16, 2003, Revised Lectures*, O. Bousquet, U. von Luxburg, and G. Rätsch, Eds., Berlin, Heidelberg: Springer, 2004, pp. 63–71. doi: 10.1007/978-3-540-28650-9_4.
- [102] Q. V. Le, T. Sarlos, and A. J. Smola, “Fastfood: Approximate Kernel Expansions in Loglinear Time,” Aug. 13, 2014, *arXiv*: arXiv:1408.3060. doi: 10.48550/arXiv.1408.3060.
- [103] L. Breiman, “Bagging predictors,” *Mach. Learn.*, vol. 24, no. 2, pp. 123–140, Aug. 1996, doi: 10.1007/BF00058655.
- [104] J. Prusa, T. M. Khoshgoftaar, and N. Seliya, “The Effect of Dataset Size on Training Tweet Sentiment Classifiers,” in *2015 IEEE 14th International Conference on Machine Learning and Applications (ICMLA)*, Dec. 2015, pp. 96–102. doi: 10.1109/ICMLA.2015.22.
- [105] C.-F. Wang *et al.*, “Upper-Arm Photoplethysmographic Sensor with One-Time Calibration for Long-Term Blood Pressure Monitoring,” *Biosensors*, vol. 13, no. 3, Art. no. 3, Mar. 2023, doi: 10.3390/bios13030321.
- [106] M. Proenca, G. Bonnier, D. Ferrario, C. Verjus, and M. Lemay, “PPG-Based Blood Pressure Monitoring by Pulse Wave Analysis: Calibration Parameters are Stable for Three Months,” *Annu. Int. Conf. IEEE Eng. Med. Biol. Soc. IEEE Eng. Med. Biol. Soc. Annu. Int. Conf.*, vol. 2019, pp. 5560–5563, Jul. 2019, doi: 10.1109/EMBC.2019.8857740.
- [107] J. Leitner, P.-H. Chiang, and S. Dey, “Personalized Blood Pressure Estimation Using Photoplethysmography: A Transfer Learning Approach,” *IEEE J. Biomed. Health Inform.*, vol. 26, no. 1, pp. 218–228, Jan. 2022, doi: 10.1109/JBHI.2021.3085526.
- [108] J. Dey, A. Gaurav, and V. N. Tiwari, “InstaBP: Cuff-less Blood Pressure Monitoring on Smartphone using Single PPG Sensor,” in *2018 40th Annual International Conference of the IEEE Engineering in Medicine and Biology Society (EMBC)*, Jul. 2018, pp. 5002–5005. doi: 10.1109/EMBC.2018.8513189.
- [109] K. Duan, Z. Qian, M. Atef, and G. Wang, “A feature exploration methodology for learning based cuffless blood pressure measurement using photoplethysmography,” in *2016 38th Annual International Conference of the IEEE Engineering in Medicine and Biology Society (EMBC)*, Aug. 2016, pp. 6385–6388. doi: 10.1109/EMBC.2016.7592189.
- [110] P. Nandi and M. Rao, “A Novel CNN-LSTM Model Based Non-Invasive Cuff-Less Blood Pressure Estimation System,” in *2022 44th Annual International Conference of the IEEE Engineering in Medicine & Biology Society (EMBC)*, Jul. 2022, pp. 832–836. doi: 10.1109/EMBC48229.2022.9871777.
- [111] J. Joung *et al.*, “Continuous cuffless blood pressure monitoring using photoplethysmography-based PPG2BP-net for high intrasubject blood pressure variations,” *Sci. Rep.*, vol. 13, no. 1, p. 8605, May 2023, doi: 10.1038/s41598-023-35492-y.
- [112] C. Qin, Y. Li, C. Liu, and X. Ma, “Cuff-Less Blood Pressure Prediction Based on Photoplethysmography and Modified ResNet,” *Bioengineering*, vol. 10, no. 4, Art. no. 4, Apr. 2023, doi: 10.3390/bioengineering10040400.
- [113] M. Kim, H. Lee, K.-Y. Kim, and K.-H. Kim, “Deep Learning Model for Blood Pressure Estimation from PPG Signal,” in *2022 IEEE International Conference on Metrology for Extended Reality, Artificial Intelligence and Neural Engineering*

REFERENCES

- (MetroXRINE), Oct. 2022, pp. 1–5. doi: 10.1109/MetroXRINE54828.2022.9967606.
- [114] N. Ibtehaz *et al.*, “PPG2ABP: Translating Photoplethysmogram (PPG) Signals to Arterial Blood Pressure (ABP) Waveforms,” *Bioengineering*, vol. 9, no. 11, Art. no. 11, Nov. 2022, doi: 10.3390/bioengineering9110692.
- [115] W. Wang, L. Zhu, F. Marefat, P. Mohseni, K. Kilgore, and L. Najafizadeh, “Photoplethysmography-Based Blood Pressure Estimation Using Deep Learning,” in *2020 54th Asilomar Conference on Signals, Systems, and Computers*, Nov. 2020, pp. 945–949. doi: 10.1109/IEEECONF51394.2020.9443447.
- [116] V. I. D’Alessandro, L. D. Palma, F. Attivissimo, A. D. Nisio, and A. M. L. Lanzolla, “U-Net convolutional neural network for multisource heterogeneous iris segmentation,” in *2023 IEEE International Symposium on Medical Measurements and Applications, MeMeA 2023 - Conference Proceedings*, 2023. doi: 10.1109/MeMeA57477.2023.10171896.
- [117] V. I. D’Alessandro, F. Adamo, L. De Palma, D. Lotano, and M. Scarpetta, “U-Net Convolutional Neural Network for Optic Disc Segmentation,” in *2023 IEEE International Conference on Metrology for eXtended Reality, Artificial Intelligence and Neural Engineering (MetroXRINE)*, Oct. 2023, pp. 1087–1091. doi: 10.1109/MetroXRINE58569.2023.10405762.
- [118] N. Ibtehaz and M. S. Rahman, “MultiResUNet: Rethinking the U-Net architecture for multimodal biomedical image segmentation,” *Neural Netw.*, vol. 121, pp. 74–87, Jan. 2020, doi: 10.1016/j.neunet.2019.08.025.
- [119] M. Chan, V. G. Ganti, and O. T. Inan, “Respiratory Rate Estimation Using U-Net-Based Cascaded Framework From Electrocardiogram and Seismocardiogram Signals,” *IEEE J. Biomed. Health Inform.*, vol. 26, no. 6, pp. 2481–2492, Jun. 2022, doi: 10.1109/JBHI.2022.3144990.
- [120] Q. Tang, Z. Chen, R. Ward, C. Menon, and M. Elgendi, “Subject-Based Model for Reconstructing Arterial Blood Pressure from Photoplethysmogram,” *Bioengineering*, vol. 9, no. 8, Art. no. 8, Aug. 2022, doi: 10.3390/bioengineering9080402.
- [121] T. B. D. S. Costa *et al.*, “Blood Pressure Estimation From Photoplethysmography by Considering Intra- and Inter-Subject Variabilities: Guidelines for a Fair Assessment,” *IEEE Access*, vol. 11, pp. 57934–57950, 2023, doi: 10.1109/ACCESS.2023.3284458.
- [122] Y. Tian, D. Su, S. Lauria, and X. Liu, “Recent advances on loss functions in deep learning for computer vision,” *Neurocomputing*, vol. 497, pp. 129–158, Aug. 2022, doi: 10.1016/j.neucom.2022.04.127.
- [123] Q. Wang, Y. Ma, K. Zhao, and Y. Tian, “A Comprehensive Survey of Loss Functions in Machine Learning,” *Ann. Data Sci.*, vol. 9, no. 2, pp. 187–212, Apr. 2022, doi: 10.1007/s40745-020-00253-5.
- [124] Z. Shen *et al.*, “Uncertainty quantification of cuffless blood pressure estimation based on parameterized model evidential ensemble learning,” *Biomed. Signal Process. Control*, vol. 92, p. 106104, Jun. 2024, doi: 10.1016/j.bspc.2024.106104.
- [125] K. Sel, A. Mohammadi, R. I. Pettigrew, and R. Jafari, “Physics-informed neural networks for modeling physiological time series for cuffless blood pressure estimation,” *Npj Digit. Med.*, vol. 6, no. 1, pp. 1–15, Jun. 2023, doi: 10.1038/s41746-023-00853-4.
- [126] Kachuee, M., Kiani, M., Mohammadzade, H., & Shabany, M., “Cuff-Less Blood

REFERENCES

- Pressure Estimation [Dataset].” UCI Machine Learning Repository., 2015. doi: <https://doi.org/10.24432/C5B602>.
- [127] J. Cheng, Y. Xu, R. Song, Y. Liu, C. Li, and X. Chen, “Prediction of arterial blood pressure waveforms from photoplethysmogram signals via fully convolutional neural networks,” *Comput. Biol. Med.*, vol. 138, p. 104877, Nov. 2021, doi: 10.1016/j.compbiomed.2021.104877.
- [128] M. Yu, Z. Huang, Y. Zhu, P. Zhou, and J. Zhu, “Attention-based residual improved U-Net model for continuous blood pressure monitoring by using photoplethysmography signal,” *Biomed. Signal Process. Control*, vol. 75, p. 103581, May 2022, doi: 10.1016/j.bspc.2022.103581.
- [129] S. Mahmud *et al.*, “A shallow U-Net architecture for reliably predicting blood pressure (BP) from photoplethysmogram (PPG) and electrocardiogram (ECG) signals,” *Sensors*, vol. 22, no. 3, p. 919, 2022.
- [130] T. Athaya and S. Choi, “An estimation method of continuous non-invasive arterial blood pressure waveform using photoplethysmography: A U-Net architecture-based approach,” *Sensors*, vol. 21, no. 5, p. 1867, 2021.
- [131] F. Khoshmanesh, P. Thurgood, E. Pirogova, S. Nahavandi, and S. Baratchi, “Wearable sensors: At the frontier of personalised health monitoring, smart prosthetics and assistive technologies,” *Biosens. Bioelectron.*, vol. 176, p. 112946, Mar. 2021, doi: 10.1016/j.bios.2020.112946.
- [132] S. M. Lopez-Silva *et al.*, “Heuristic algorithm for photoplethysmographic heart rate tracking during maximal exercise test,” *J. Med. Biol. Eng.*, vol. 32, no. 3, pp. 181–188, 2012, doi: 10.5405/jmbe.898.
- [133] S. K. Longmore, G. Y. Lui, G. Naik, P. P. Breen, B. Jalaludin, and G. D. Gargiulo, “A comparison of reflective photoplethysmography for detection of heart rate, blood oxygen saturation, and respiration rate at various anatomical locations,” *Sens. Switz.*, vol. 19, no. 8, 2019, doi: 10.3390/s19081874.
- [134] P. Wei, R. Guo, J. Zhang, and Y. T. Zhang, “A New Wristband Wearable Sensor Using Adaptive Reduction Filter to Reduce Motion Artifact,” in *2008 International Conference on Information Technology and Applications in Biomedicine*, May 2008, pp. 278–281. doi: 10.1109/ITAB.2008.4570636.
- [135] R. Lazazzera, Y. Belhaj, and G. Carrault, “A New Wearable Device for Blood Pressure Estimation Using Photoplethysmogram,” *Sensors*, vol. 19, no. 11, Art. no. 11, Jan. 2019, doi: 10.3390/s19112557.
- [136] B. De Marchi, M. Frigerio, S. De Nadai, G. Longinotti-Buitoni, and A. Aliverti, “Blood Pressure Continuous Measurement through a Wearable Device: Development and Validation of a Cuffless Method,” *Sensors*, vol. 21, no. 21, Art. no. 21, Jan. 2021, doi: 10.3390/s21217334.
- [137] “MAX30102 Datasheet and Product Info | Analog Devices.” Accessed: Dec. 10, 2024. [Online]. Available: <https://www.analog.com/en/products/max30102.html>
- [138] “MAXREFDES117 | reference design | Analog Devices.” Accessed: Dec. 10, 2024. [Online]. Available: <https://www.analog.com/en/resources/reference-designs/maxrefdes117.html#rd-overview>
- [139] L. De Palma, A. D. Nisio, A. Lanzolla, D. Lotano, A. Pignatelli, and M. A. Ragolia, “Development of a System for Monitoring Driver Comfort via Smartphones,” in *2024 IEEE International Symposium on Medical Measurements and Applications*

REFERENCES

- (MeMeA), Jun. 2024, pp. 1–6. doi: 10.1109/MeMeA60663.2024.10596743.
- [140] L. Pepa, M. Capecchi, F. Verdini, M. G. Ceravolo, and L. Spalazzi, “An architecture to manage motor disorders in Parkinson’s disease,” in *2015 IEEE 2nd World Forum on Internet of Things (WF-IoT)*, 2015, pp. 615–620. doi: 10.1109/WF-IoT.2015.7389124.
- [141] P. Maia *et al.*, “A Web Platform for Interconnecting Body Sensors and Improving Health Care,” *Procedia Comput. Sci.*, vol. 40, pp. 135–142, Jan. 2014, doi: 10.1016/j.procs.2014.10.041.
- [142] E. O. Méndez and S. Ren, “Design of cyber-physical interface for automated vital signs reading in electronic medical records systems,” in *2012 IEEE International Conference on Electro/Information Technology*, 2012, pp. 1–10. doi: 10.1109/EIT.2012.6220696.
- [143] J. Mohammed, C.-H. Lung, A. Ocneanu, A. Thakral, C. Jones, and A. Adler, “Internet of Things: Remote Patient Monitoring Using Web Services and Cloud Computing,” in *2014 IEEE International Conference on Internet of Things (iThings), and IEEE Green Computing and Communications (GreenCom) and IEEE Cyber, Physical and Social Computing (CPSCom)*, 2014, pp. 256–263. doi: 10.1109/iThings.2014.45.
- [144] P. K. Khosla, M. Mittal, L. M. Goyal, and K. Chachra, “Mitigate the Impact of Covid-19: Telehealth,” in *Predictive and Preventive Measures for Covid-19 Pandemic*, P. K. Khosla, M. Mittal, D. Sharma, and L. M. Goyal, Eds., Singapore: Springer, 2021, pp. 1–17. doi: 10.1007/978-981-33-4236-1_1.
- [145] Y. E. Rivera Julio, “Design ubiquitous architecture for telemedicine based on mhealth Arduino 4G LTE,” in *2016 IEEE 18th International Conference on e-Health Networking, Applications and Services (Healthcom)*, 2016, pp. 1–6. doi: 10.1109/HealthCom.2016.7749440.
- [146] A. M. Plaza, J. Díaz, and J. Pérez, “Software architectures for health care cyber-physical systems: A systematic literature review,” *J. Softw. Evol. Process*, vol. 30, no. 7, p. e1930, 2018, doi: 10.1002/smr.1930.
- [147] M. A. Ragolia, F. Attivissimo, A. Di Nisio, A. M. L. Lanzolla, and M. Scarpetta, “Reducing effect of magnetic field noise on sensor position estimation in surgical EM tracking,” in *2021 IEEE International Symposium on Medical Measurements and Applications (MeMeA)*, 2021, pp. 1–6. doi: 10.1109/MeMeA52024.2021.9478723.
- [148] A. Annunziato, F. Anelli, J. Gates, C. Holmes, and F. Prudenzeno, “Design of Polarization-Maintaining FBGs Using Polyimide Films to Improve Strain-Temperature Sensing in CFRP Laminates,” *IEEE Photonics J.*, vol. 13, no. 2, pp. 1–15, 2021, doi: 10.1109/JPHOT.2021.3063172.
- [149] F. Attivissimo, C. Guarnieri Calò Carducci, A. M. L. Lanzolla, and M. Spadavecchia, “An Extensive Unified Thermo-Electric Module Characterization Method,” *Sensors*, vol. 16, no. 12, Art. no. 12, Dec. 2016, doi: 10.3390/s16122114.
- [150] M. A. Ragolia, F. Attivissimo, A. D. Nisio, A. M. L. Lanzolla, and M. Scarpetta, “A virtual platform for real-time performance analysis of electromagnetic tracking systems for surgical navigation,” *Acta IMEKO*, vol. 10, no. 4, Art. no. 4, Dec. 2021, doi: 10.21014/acta_imeko.v10i4.1191.
- [151] L. De Palma, V. I. D’Alessandro, F. Attivissimo, A. D. Nisio, and A. M. L. Lanzolla, “ECG wave segmentation algorithm for complete P-QRS-T detection,” in *2023 IEEE International Symposium on Medical Measurements and Applications (MeMeA)*, Jun. 2023, pp. 1–6. doi: 10.1109/MeMeA57477.2023.10171894.

REFERENCES

- [152] E. Olvera Lopez, B. D. Ballard, and A. Jan, "Cardiovascular Disease," in *StatPearls*, Treasure Island (FL): StatPearls Publishing, 2024. Accessed: Jul. 24, 2024. [Online]. Available: <http://www.ncbi.nlm.nih.gov/books/NBK535419/>
- [153] S. C. Mukhopadhyay, "Wearable Sensors for Human Activity Monitoring: A Review," *IEEE Sens. J.*, vol. 15, no. 3, pp. 1321–1330, 2015, doi: 10.1109/JSEN.2014.2370945.
- [154] L. D'Alvia *et al.*, "Accuracy evaluation of an ECG device for heart failure patients self-monitoring: a preliminary study," in *2022 IEEE International Symposium on Medical Measurements and Applications (MeMeA)*, 2022, pp. 1–6. doi: 10.1109/MeMeA54994.2022.9856535.
- [155] F. Goodarzy, E. S. Skafidas, and S. Gambini, "Feasibility of Energy-Autonomous Wireless Microsensors for Biomedical Applications: Powering and Communication," *IEEE Rev. Biomed. Eng.*, vol. 8, pp. 17–29, 2015, doi: 10.1109/RBME.2014.2346487.
- [156] V. I. D'Alessandro, F. Paciolla, L. de Palma, F. Adamo, A. Di Nisio, and N. Giaquinto, "Robotized sorter for blood classification using RFID tags," in *2022 IEEE International Symposium on Medical Measurements and Applications (MeMeA)*, 2022, pp. 1–6. doi: 10.1109/MeMeA54994.2022.9856477.
- [157] N. Giaquinto, M. Scarpetta, M. A. Ragolia, and P. Pappalardi, "Real-time drip infusion monitoring through a computer vision system," in *2020 IEEE International Symposium on Medical Measurements and Applications (MeMeA)*, 2020, pp. 1–5. doi: 10.1109/MeMeA49120.2020.9137359.
- [158] K. Hung, Y. T. Zhang, and B. Tai, "Wearable medical devices for tele-home healthcare," in *The 26th Annual International Conference of the IEEE Engineering in Medicine and Biology Society*, 2004, pp. 5384–5387. doi: 10.1109/IEMBS.2004.1404503.
- [159] G. Andria, F. Attivissimo, N. Giaquinto, A. M. L. Lanzolla, L. Quagliarella, and N. Sasanelli, "Functional Evaluation of Handgrip Signals for Parkinsonian Patients," *IEEE Trans. Instrum. Meas.*, vol. 55, no. 5, pp. 1467–1473, 2006, doi: 10.1109/TIM.2006.881029.
- [160] M. Scarpetta, M. Spadavecchia, G. Andria, M. A. Ragolia, and N. Giaquinto, "Simultaneous measurement of heartbeat intervals and respiratory signal using a smartphone," in *2021 IEEE International Symposium on Medical Measurements and Applications, MeMeA 2021 - Conference Proceedings*, 2021. doi: 10.1109/MeMeA52024.2021.9478711.
- [161] L. Grajales and I. V. Nicolaescu, "Wearable multisensor heart rate monitor," in *International Workshop on Wearable and Implantable Body Sensor Networks (BSN'06)*, 2006, p. 4 pp. – 157. doi: 10.1109/BSN.2006.58.
- [162] P. E. McSharry, G. D. Clifford, L. Tarassenko, and L. A. Smith, "A dynamical model for generating synthetic electrocardiogram signals," *IEEE Trans. Biomed. Eng.*, vol. 50, no. 3, pp. 289–294, Mar. 2003, doi: 10.1109/TBME.2003.808805.
- [163] J. Aspuru *et al.*, "Segmentation of the ECG Signal by Means of a Linear Regression Algorithm," *Sensors*, vol. 19, no. 4, p. 775, Feb. 2019, doi: 10.3390/s19040775.
- [164] J. Pan and W. J. Tompkins, "A Real-Time QRS Detection Algorithm," *IEEE Trans. Biomed. Eng.*, vol. BME-32, no. 3, pp. 230–236, 1985, doi: 10.1109/TBME.1985.325532.
- [165] "Development of QRS Detection using Short-time Fourier Transform based Technique." Accessed: Jul. 24, 2024. [Online]. Available:

REFERENCES

- <https://www.ijcaonline.org/specialissues/casct/number1/998-32/>
- [166] N. Prashar, M. Sood, and S. Jain, "Semiautomatic detection of cardiac diseases employing dual tree complex wavelet transform," *Period. Eng. Nat. Sci.*, vol. 6, no. 2, Art. no. 2, Nov. 2018, doi: 10.21533/pen.v6i2.188.
- [167] J. P. V. Madeiro, P. C. Cortez, F. I. Oliveira, and R. S. Siqueira, "A new approach to QRS segmentation based on wavelet bases and adaptive threshold technique," *Med. Eng. Phys.*, vol. 29, no. 1, pp. 26–37, Jan. 2007, doi: 10.1016/j.medengphy.2006.01.008.
- [168] H. N. Abderahman, H. R. Dajani, and V. Z. Groza, "Adaptive R-Peak Detector in Extreme Noise Using EMD Selective Analyzer," in *2022 IEEE International Symposium on Medical Measurements and Applications (MeMeA)*, 2022, pp. 1–6. doi: 10.1109/MeMeA54994.2022.9856531.
- [169] "A Review on the Applications of Time-Frequency Methods in ECG Analysis - Pradhan - 2023 - Journal of Healthcare Engineering - Wiley Online Library." Accessed: Jul. 24, 2024. [Online]. Available: <https://onlinelibrary.wiley.com/doi/10.1155/2023/3145483>
- [170] S. K. Mukhopadhyay, M. Mitra, and S. Mitra, "ECG feature extraction using differentiation, Hilbert transform, variable threshold and slope reversal approach," *J. Med. Eng. Technol.*, vol. 36, no. 7, pp. 372–386, Oct. 2012, doi: 10.3109/03091902.2012.713438.
- [171] M. Rakshit and S. Das, "An efficient wavelet-based automated R-peaks detection method using Hilbert transform," *Biocybern. Biomed. Eng.*, vol. 37, no. 3, pp. 566–577, Jan. 2017, doi: 10.1016/j.bbe.2017.02.002.
- [172] F. Adamo, F. Attivissimo, A. Di Nisio, M. Savino, and M. Spadavecchia, "A spectral estimation method for nonstationary signals analysis with application to power systems," *Measurement*, vol. 73, pp. 247–261, Sep. 2015, doi: 10.1016/j.measurement.2015.04.023.
- [173] I. Beraza and I. Romero, "Comparative study of algorithms for ECG segmentation," *Biomed. Signal Process. Control*, vol. 34, pp. 166–173, Apr. 2017, doi: 10.1016/j.bspc.2017.01.013.
- [174] S. S. Mehta and N. S. Lingayat, "SVM-based algorithm for recognition of QRS complexes in electrocardiogram," *IRBM*, vol. 29, no. 5, pp. 310–317, Nov. 2008, doi: 10.1016/j.rbmret.2008.03.006.
- [175] G. Goovaerts, S. Padhy, B. Vandenberg, C. Varon, R. Willems, and S. Van Huffel, "A Machine-Learning Approach for Detection and Quantification of QRS Fragmentation," *IEEE J. Biomed. Health Inform.*, vol. 23, no. 5, pp. 1980–1989, Sep. 2019, doi: 10.1109/JBHI.2018.2878492.
- [176] P. Silva *et al.*, "Towards better heartbeat segmentation with deep learning classification," *Sci. Rep.*, vol. 10, p. 20701, Nov. 2020, doi: 10.1038/s41598-020-77745-0.
- [177] S. Vijayarangan, V. R., B. Murugesan, P. S.P., J. Joseph, and M. Sivaprakasam, "RPnet: A Deep Learning approach for robust R Peak detection in noisy ECG," in *2020 42nd Annual International Conference of the IEEE Engineering in Medicine & Biology Society (EMBC)*, 2020, pp. 345–348. doi: 10.1109/EMBC44109.2020.9176084.
- [178] X. Liu, H. Wang, Z. Li, and L. Qin, "Deep learning in ECG diagnosis: A review," *Knowl.-Based Syst.*, vol. 227, p. 107187, Sep. 2021, doi: 10.1016/j.knosys.2021.107187.

REFERENCES

- [179] P. Choudhary, R. Jaswal, and P. G. Scholar, "ECG SIGNAL DENOISING USING UWT AND FEATURES EXTRACTION USING LABVIEW," vol. 03, no. 07.
- [180] M. L. Ramirez *et al.*, "A Novel Methodology for Calculating Heart Rate using Images Processing," *IEEE Lat. Am. Trans.*, vol. 14, no. 8, pp. 3522–3527, Aug. 2016, doi: 10.1109/TLA.2016.7786329.
- [181] N. Otsu, "A Threshold Selection Method from Gray-Level Histograms," *IEEE Trans. Syst. Man Cybern.*, vol. 9, no. 1, pp. 62–66, Jan. 1979, doi: 10.1109/TSMC.1979.4310076.